

สำนักหอสมุดกลาง พระจอมเกล้าลาดกระบัง

DEVELOPMENT OF ALUMINIUM FOAM PANEL FOR SOUND
ABSORPTION IN ROAD VEHICLES



E077809



PHADUNGKIAT PHEWOON

เลขหมู่.....077809
เลขทะเบียน.....
วัน,เดือน,ปี..... 13 ส.ย. 2559

b. 127 11 10
i.

A THESIS SUBMITTED IN PARTIAL FULFILLMENT
OF THE REQUIREMENT FOR THE DEGREE OF
MASTER OF ENGINEERING IN AUTOMOTIVE ENGINEERING
(INTERNATIONAL PROGRAM)
INTERNATIONAL COLLEGE
KING MONGKUT'S INSTITUTE OF TECHNOLOGY LADKRABANG

2015

KMITL-2015-IC-M-004-02

This material is reserved for educational use only, not allowed for commercial use.

Forbidden to modify the content, and cite the document when use.



COPY RIGHT 2015

INTERNATIONAL COLLEGE

KING MONGKUT'S INSTITUTE OF TECHNOLOGY LADKRABANG

NATIONAL SCIENCE AND TECHNOLOGY DEVELOPMENT AGENCY

This material is reserved for educational use only, not allowed for commercial use.

Forbidden to modify the content, and cite the document when use.

ABSTRACT

Thesis Title	Development of aluminium foam panel for sound absorption in road vehicles
Thesis Credits	12
Candidate	Mr. Phadungkiat Phewoon
Thesis Advisors	Asst. Prof. Dr. Panya Kansuwan Dr. Sompong Srimanosaowapak Prof. Dr. Naoto Ohtake
Program	Master of Engineering
Field of Study	Automotive Engineering
Department	Mechanical Engineering
Faculty	Engineering
B.E.	2558

Abstract

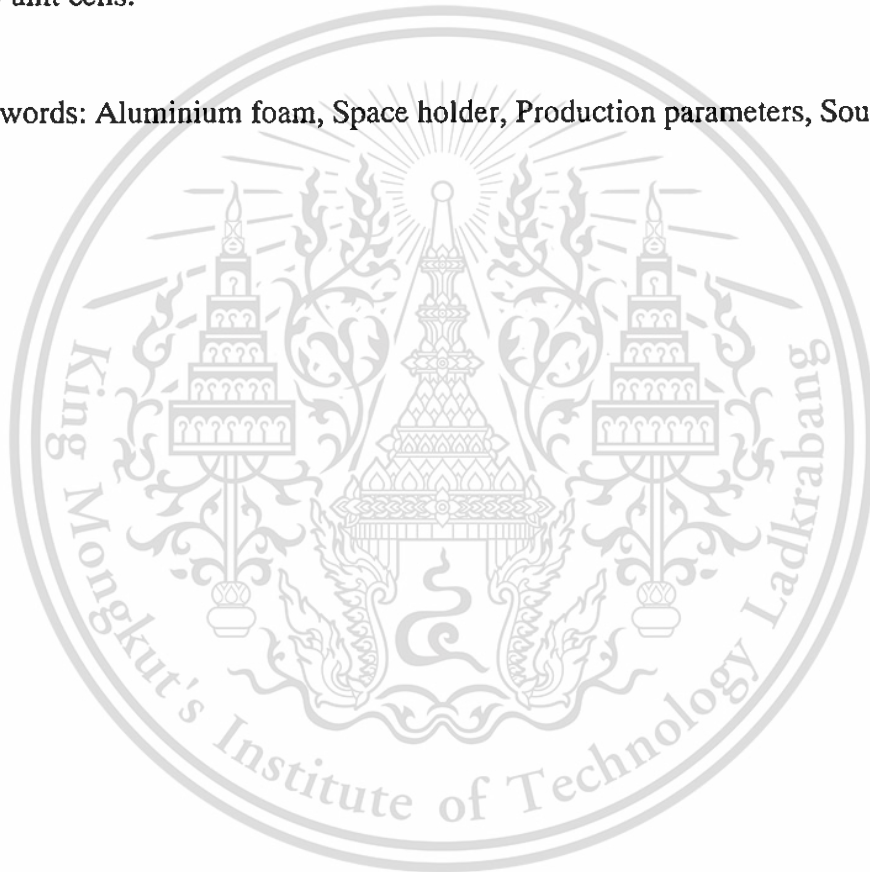
Open cell aluminium foams made from AC2A aluminium alloy were produced using vacuum pressure to assist molten metal to fill into space of preforms of sizes 4.1, 5.0 and 6.3 mm to obtain aluminum foams with combines properties, such as lightweight, good energy absorption, sound absorption and heat transfer. In this research, influence of production parameters affecting foam structure, mechanical properties and sound absorption, and foam installation affecting efficiency of sound absorption was investigated. The properties of aluminium foam prototype are aimed to overcome those of current sound absorptive materials which are still in limit of use.

The results indicate that gas permeability coefficient of mold affected density of aluminium foams and characteristic of molten metal filling at infiltration zones of mold. It was found that the use of pouring temperature of molten metal at 720°C and molds with gas permeability coefficient of $31.26 \times 10^{-12} \text{ m}^2$, while vacuum pressure was kept constant, gave aluminium foams with a high percentage of molten metal filling resulting in high density and uniform structure. The use of molds with higher gas permeability coefficients resulted in aluminium foams with lower percentages of molten metal filling and density, thinner cell walls and less uniform structure. Level of vacuum pressure was found to directly proportional to both percentage of molten metal filling and density.

For sound absorption performance of aluminium foam samples with three sizes of spherical perform, it was found that sound absorption as a function of sound absorption coefficients against frequencies increased with increasing thickness and density of

samples, especially at low frequencies in the ranges of 125 – 1,000 Hz. Decreasing preform sizes, while density and sample thickness were kept constant, resulted in aluminium foams with lower energy absorption capacity but higher sound absorption performance. Moreover, installation by having air gap behind an aluminium foam sample enhanced sound absorption coefficient at frequencies depending on the size of the air gap. Predictions of sound absorption coefficients based on structural parameters of aluminium foam gave relatively good agreement with those of measurements. Less disagreement in predictions was obtained when aluminium foams with more thickness and cell number were used. The lowest level of disagreement in predictions in this work (10% – 33% at the range of frequencies of 125 – 250 Hz) was obtained with aluminium foams having 46 – 63 unit cells.

Keywords: Aluminium foam, Space holder, Production parameters, Sound absorption



หัวข้อวิทยานิพนธ์	การพัฒนาแผ่นโพลีเอทิลีนสำหรับดูดซับเสียงในยานยนต์
หน่วยกิต	12
ผู้เขียน	นายผดุงเกียรติ ผิวอ่อน
อาจารย์ที่ปรึกษา	ผศ. ดร. ปัญญา ชันธุ์สุวรรณ ดร. สมพงษ์ ศรีมโนเสาวภาคย์ Prof. Dr. Naoto Ohtake
หลักสูตร	วิศวกรรมศาสตรมหาบัณฑิต
สาขาวิชา	วิศวกรรมยานยนต์
ภาควิชา	วิศวกรรมเครื่องกล
คณะ	คณะวิศวกรรมศาสตร์
พ.ศ.	2558
	บทคัดย่อ

โพลีเอทิลีนแบบรูเปิด ผลิตจากโพลีเอทิลีนอัลลอย AC2A โดยการหล่อโลหะด้วยวิธีใช้แม่แบบร่างขนาดเส้นผ่านศูนย์กลางเฉลี่ย 4.1, 5.0 และ 6.3 มิลลิเมตร โดยใช้แรงดันสุญญากาศช่วยเติมน้ำโลหะเข้าสู่ช่องว่างของแม่แบบร่าง ทำให้ได้โพลีเอทิลีนที่มีน้ำหนักเบา มีความสามารถในการรับแรงกระแทกได้ดี ดูดซับเสียงและถ่ายเทความร้อนได้ดี งานวิจัยนี้ได้ทำการศึกษาอิทธิพลของตัวแปรในการผลิตชิ้นงาน โพลีเอทิลีนซึ่งส่งผลกระทบต่อโครงสร้าง คุณสมบัติทางกลและการดูดซับเสียง รวมทั้งวิธีการติดตั้งชิ้นงานเพื่อเพิ่มประสิทธิภาพของการดูดซับเสียง โดยมีเป้าหมายเพื่อให้ต้นแบบโพลีเอทิลีนมีคุณสมบัติเหนือกว่าของวัสดุดูดซับเสียงที่มีในปัจจุบันที่ยังคงมีข้อจำกัดในการใช้งาน

ผลการทดลองพบว่าค่าสัมประสิทธิ์การซึมผ่านของอากาศผ่านรูทางออกของแม่พิมพ์ มีผลต่อความหนาแน่นของโพลีเอทิลีนและลักษณะของการเติมน้ำโลหะในแต่ละส่วนในแม่พิมพ์ ซึ่งพบว่าอุณหภูมิเหนือน้ำโลหะที่ 720 องศาเซลเซียส ภายใต้แรงดันสุญญากาศคงที่ ค่าสัมประสิทธิ์การซึมผ่านของอากาศผ่านรูทางออกของแม่พิมพ์ 31.26×10^{-12} ตารางเมตร ได้ชิ้นงานที่มีเปอร์เซ็นต์การเติมน้ำโลหะสูงส่งผลให้มีความหนาแน่นสูงและมีความสม่ำเสมอของโครงสร้าง ส่วนการเพิ่มค่าสัมประสิทธิ์การซึมผ่านของอากาศผ่านรูทางออกของแม่พิมพ์ทำให้ได้ชิ้นงานที่มีเปอร์เซ็นต์การเติมน้ำโลหะและความหนาแน่นต่ำ มีผนังเซลล์บางและความสม่ำเสมอของโครงสร้างน้อยกว่า สำหรับผลของค่าแรงดันสุญญากาศที่ใช้ในการผลิต พบว่ามีความสัมพันธ์โดยตรงกับเปอร์เซ็นต์การเติมน้ำโลหะและความหนาแน่น

ประสิทธิภาพของการดูดซับเสียงของชิ้นงาน โพลีเอทิลีนที่มีขนาดเส้นผ่านศูนย์กลางของแม่แบบร่างทั้งสามขนาด พบว่าการวัดค่าประสิทธิภาพการดูดซับเสียงซึ่งแสดงผลในรูปของค่าสัม

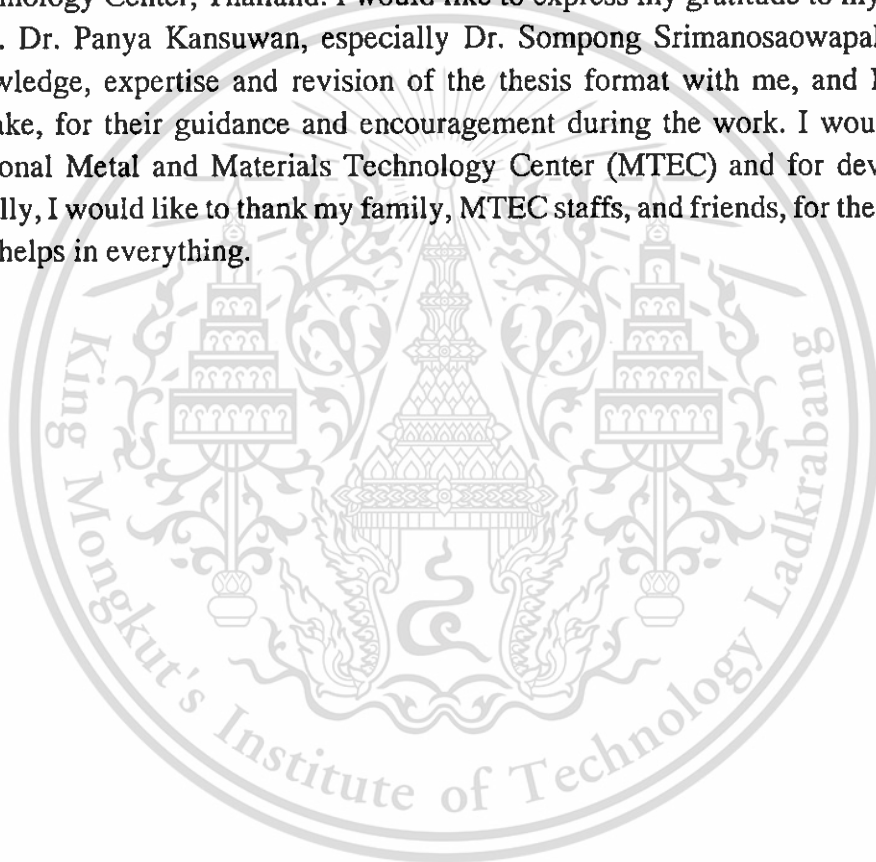
ประสิทธิภาพการดูดซับเสียงต่อความถี่มีค่าเพิ่มขึ้นตามความหนาและความหนาแน่นของชิ้นงาน โดยเฉพาะช่วงความถี่ต่ำที่ 125 – 1,000 เฮิรตซ์ ส่วนการลดลงของขนาดแม่แบบร่างโดยที่ความหนาแน่นและขนาดชิ้นงานเท่าเดิมทำให้ค่าความแข็งแรงของการรับแรงลดลงแต่สัมประสิทธิ์ในการดูดซับเสียงมีค่าสูงขึ้น นอกจากนี้การติดตั้งชิ้นงานโดยให้มีช่องว่างอากาศที่ด้านหลังของชิ้นงาน ทำให้สัมประสิทธิ์การดูดซับเสียงมีค่าเพิ่มขึ้นในช่วงถี่ต่างๆ ซึ่งขึ้นกับขนาดของช่องว่างอากาศการทำนายค่าสัมประสิทธิ์ในการดูดซับเสียงโดยใช้ค่าพารามิเตอร์ของโครงสร้างโฟมอะลูมิเนียมให้ผลทำนายใกล้เคียงกับผลการวัด โดยค่าความคาดเคลื่อนจะลดลงเมื่อจำนวนเซลล์หรือความหนาของชิ้นงานที่ใช้ทำนายเพิ่มขึ้น ซึ่งจำนวนเซลล์ที่ให้ผลทำนายค่าสัมประสิทธิ์การดูดซับเสียงมีความคาดเคลื่อนต่ำที่สุด (10% - 33% ที่ช่วงความถี่ 125 -250 เฮิรตซ์) สำหรับชิ้นงานโฟมอะลูมิเนียมที่ผลิตในงานวิจัยนี้ คือ 46 – 63 ยูนิทเซลล์

คำสำคัญ: โฟมอะลูมิเนียม แม่แบบร่าง พารามิเตอร์ในการผลิต การดูดซับเสียง



ACKNOWLEDGEMENTS

I gratefully acknowledge a scholarship from Thailand Advanced Institute of Science and Technology, and Tokyo Institute of Technology (TAIST-Tokyo Tech) which is a collaborative program among National Science and Technology Development Agency (NSTDA, Thailand), Tokyo Institute of Technology (Tokyo Tech, Japan) and King Mongkut's Institute of Technology Ladkrabang (KMIL, Thailand). This work was supported by National Metal and Materials Technology Center [grant number MT-B-55-MET-07-252-I]. This study has been carried during the year 2011-2015 as a part of a research project in the Near Net Shape Laboratory, National Metal and Materials Technology Center, Thailand. I would like to express my gratitude to my advisors; Asst. Prof. Dr. Panya Kansuwan, especially Dr. Sompong Srimanosaowapak for giving all knowledge, expertise and revision of the thesis format with me, and Prof. Dr. Naoto Othake, for their guidance and encouragement during the work. I would like to thank National Metal and Materials Technology Center (MTEC) and for devices supported. Finally, I would like to thank my family, MTEC staffs, and friends, for their great supports and helps in everything.

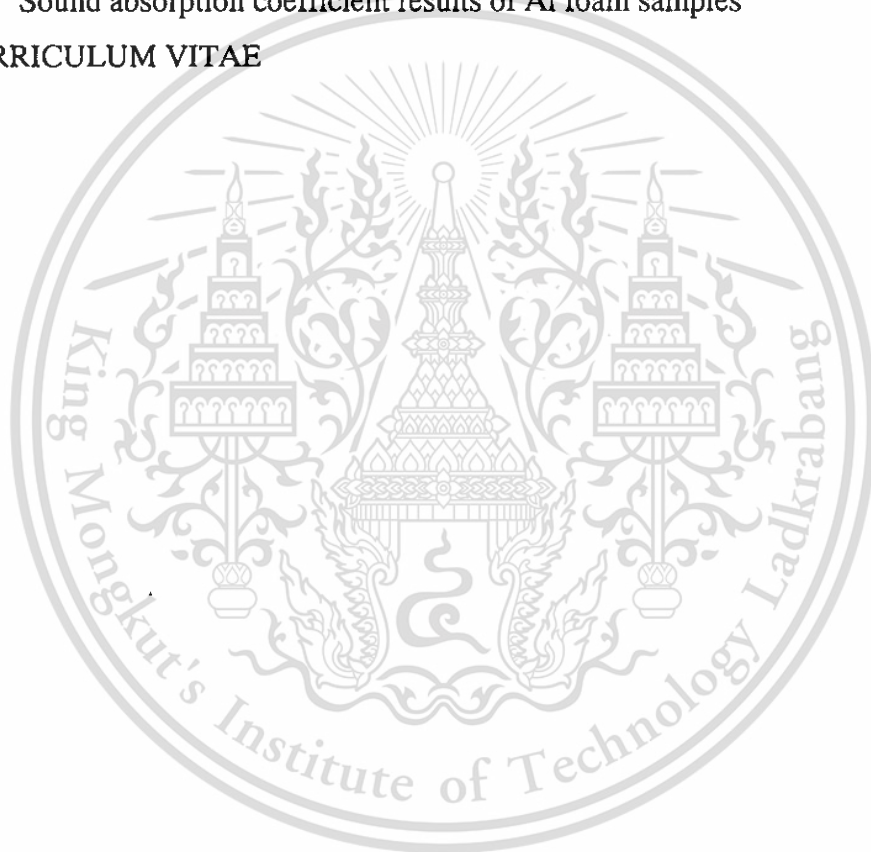


CONTENTS

	PAGE
ABSTRACT	i
ACKNOWLEDGEMENTS	v
CONTENTS	vi
LIST OF TABLES	ix
LIST OF FIGURES	x
LIST OF SYMBOLS	xviii
LIST OF TECHNICAL VOCABULARY AND ABBREVIATION	xxi
CHAPTER 1 INTRODUCTION	1
1.1 Background	1
1.2 Objectives	1
1.3 Scope of Research	2
1.4 Thesis Outline	2
CHAPTER 2 LITERATURE REVIEW	3
2.1 Noises in Vehicles	3
2.1.1 Type of Noises in Vehicles.....	3
2.1.2 Noises and Their Sources in Vehicles.....	3
2.1.3 Interior Sound Design for Vehicles.....	5
2.2 Noise Control in Vehicles	6
2.2.1 Noise Control Mechanisms.....	6
2.2.2 Noise Control Methods.....	7
2.2.3 Materials for Noise Control.....	9
2.3 Fundamental of Open Cell Aluminium Foam	11
2.3.1 Parameters of Open Cell Aluminium Foam Structure.....	11
2.3.2 Applications of Open Cell Aluminium Foam.....	12
2.4 Production Methods of Open Cell Aluminium Foam	13
2.4.1 Space Holder Method.....	13
2.4.2 Investment Casting Method (Duocel® aluminium foam).....	15
2.4.3 Honeycomb Casting Process (Alvéotec).....	16
2.4.4 Styropor Granules Sintering Method (Globomet®).....	17
2.4.5 Replica method.....	18
2.5 Production Parameters Influencing on Foam Structure	19

2.5.1 Degree of Drainage.....	19
2.5.2 Infiltration Pressure	20
2.5.3 Infiltration Temperature	23
2.6 Mechanical Properties of Open Cell Aluminium Foam	24
2.7 Acoustical Property of Open Cell Aluminium Foam	26
2.7.1 Sound Absorption performance.....	26
2.7.2 Acoustical measurement.....	31
CHAPTER 3 EXPERIMENTAL PROCEDURE.....	34
3.1 Aluminium Foam Production	34
3.1.1 Space Holder with Vacuum Infiltration Method	34
3.2 Investigation of Infiltration Parameters on Aluminium Foam Structure	35
3.2.1 Gas permeability through mold drainage	36
3.2.2 Initial Infiltration Pressure.....	37
3.2.3 Melt Temperature	38
3.3 Characterisation	38
3.3.1 X-Ray and CT-Scan Imaging	38
3.3.2 Density and Porosity.....	38
3.3.3 Pore Size and Aperture Size	40
3.3.4 Compressive test.....	41
3.3.5 Acoustic Measurement	42
CHAPTER 4 RESULTS AND DISCUSSION.....	45
4.1 Influence of Production Parameters	45
4.1.1 Effect of Gas Permeability through mold drainages	45
4.1.2 Effect of Initial Vacuum Pressure	55
4.1.3 Effect of Melt Temperature	61
4.2 Structure of Aluminium Foams	66
4.2.1 Uniformity of Structure	66
4.2.2 Aperture Size	72
4.3 Compressive test	74
4.4 Sound Absorption Test	80
4.4.1 Effect of Structural Foam on Sound Absorption Performance.....	81
4.4.2 The Use of Models for Prediction of Sound Absorption Performance of Al foams	87
This material.....	87

4.4.3 Sound Absorption Material for Automotive applications	100
CHAPTER 5 CONCLUSIONS AND SUGGESTIONS	105
5.1 Conclusions	105
5.2 Suggestions	106
REFERENCES	107
APPENDIX	115
I. Image analysis method for porosity measurement of Al foams	115
II. Sound absorption coefficient test using VA-LAB 4 IMP software	115
III. Sound absorption coefficient results of Al foam samples	117
CURRICULUM VITAE	118



LIST OF TABLES

TABLE	PAGE
Table 2.1 Recommendations for permissible sound level inside motor vehicles [6].	5
Table 2.2 Sound pressure level and corresponding sound pressure [10].	7
Table 2.3 Models relating to production and structure parameters of foams produced using infiltration method.	22
Table 2.4 Aluminium foams produced using space holder method.	23
Table 2.5 Prediction models for sound absorption coefficient of porous materials.	29
Table 2.6 Comparative properties of sound absorbant materials [76].	31
Table 3.1 Chemical compositions of AC2A (A319) aluminium alloy used for producing aluminum foams in this work.	34
Table 3.2 Parameters used in different experimental schemes of aluminium foam production.	37
Table 3.3 Parameters used for producing aluminium foams using different pouring temperatures.	38
Table 3.4 Dimensions and some physical properties of open cell aluminium foam specimens used for compressive test.	42
Table 3.5 Impedance tube specifications.	43
Table 4.1 Production parameters and characteristics of aluminium foams.	45
Table 4.2 Results of different drainage molds for producing aluminium foams with AC2A aluminium alloys using pouring temperatures 715 – 720 °C and initial vacuum pressure -100 kPa.	46
Table 4.3 Conditions for production of three different pore size AC2A aluminium foams with spongy and dense structures.	53
Table 4.4 Density of aluminium foams produced from AC2A aluminium alloy using conditions shown in Table 4.3 .	53
Table 4.5 Physical and mechanical properties of produced aluminium foams.	77
Table 4.6 Properties of aluminium foams produced by infiltration method.	80
Table 4.7 Structural parameters used to predict sound absorption coefficients of aluminium foams by previous researchers.	88

LIST OF FIGURES

FIGURES	PAGE
Figure 2.1 Transfer paths of airborne noise in a car [1].....	3
Figure 2.2 Transfer paths of structure-borne noise in a car [1].....	3
Figure 2.3 Noises transmitting through a car compartment and their sources [2].	4
Figure 2.4 Noises in an automotive vehicle classified by type, source and frequency [3].....	4
Figure 2.5 Interior sound pressure level at the front right ear (Dark and light traces represent for vehicles with standard and acoustic windshield, respectively) [4].....	5
Figure 2.6 Schematic diagram of sound absorption mechanism by aluminium foam panel [8].	6
Figure 2.7 Methods of noise reduction in automotive components: reduce, absorb and block [11].	8
Figure 2.8 Installation of sound absorption materials in automotive components [12].	9
Figure 2.9 Three main types of porous absorption materials [13].	10
Figure 2.10 Sound absorptive materials in automotive vehicle components.....	11
Figure 2.11 Enlargement of cell wall showing the presence of apertures [16].....	12
Figure 2.12 Main automotive applications of metallic foams [17].....	12
Figure 2.13 Applications of open cell aluminium foams [18].	13
Figure 2.14 Production of cellular metallic materials using space-holder fillers [17].	14
Figure 2.15 Effect of space holder size on porosity of Al foams [28].....	15
Figure 2.16 Schematic diagram of investment casting method for open cell aluminium foam production such as Duocel® aluminium foam) [19].	16
Figure 2.17 Photographs of cell structures: modified and cubic cells [29].....	16
Figure 2.18 Schematic diagram of direct casting method for open cell aluminium foam production (Alvéotec process) [29].	17
Figure 2.19 Photographs of aluminium foams produced from hollow spheres [30].	17
Figure 2.20 Schematic diagram of (globomet® process) [30].....	18
Figure 2.21 Schematic diagram of replica method for open cell aluminium foam production [31].....	19
Figure 2.22 Photographs of stainless steel foams with ligament of cell structures having hollow inside [32].	19
Figure 2.23 Pressure balance at the advancing melt front in the pressure infiltration process [39].....	21
Figure 2.24 Dependence of critical pressure required for infiltration into space of different size of SiC space holder [39].	21
Figure 2.25 Schematic of molten metal temperature during advancing into a filler (space holder) in infiltration process [44].....	24
Figure 2.26 Typical compressive stress-strain response of cellular metal [56].	25

This material is reserved for educational use only, not allowed for commercial use.

Forbidden to modify the content, and cite the document when use.

Figure 2.27 Compressive stress-strain curves of commercial open cell aluminium foams [60].	26
Figure 2.28 Sound absorption results of open cell aluminium foams.	28
Figure 3.1 Photographs of different size spherical preforms for producing aluminium foams: (a) 4.0 - 4.2 mm, (b) 4.9 – 5.1 mm and (c) 6.2 – 6.4 mm.	34
Figure 3.2 Schematic diagram of aluminium foam production using vacuum infiltration method: a) preparation of space holder and mold, b) infiltration with molten Al alloys and c) space holder removal.	35
Figure 3.3 Plaster mold with spherical preforms used for producing aluminiums foams.	36
Figure 3.4 Schematic diagram of equipment used for gas permeability measurement.	37
Figure 3.5 Weight measurement of aluminium foams: (a) cross-section and (b) bulk.	39
Figure 3.6 Aluminium foam: (a) as-cast, (b) mounted in a cylindrical tube using resin dyed with black colour paint and (c) sectioned specimen.	39
Figure 3.7 of aluminium foams measured using image analysis method: (a) scanned image, (b) B&W image and (c) pore area thresholded by imageJ software.	40
Figure 3.8 Pores of an aluminium foam measured using image analysis method: (a) image taken using a DSLR camera with macro lens, (b) B&W image adjustment and (c) pores thresholded by ImageJ software.	41
Figure 3.9 Apertures of an aluminium foam measured using image analysis method: (a) image taken using a DSLR camera with macro lens, (b) B&W image adjustment and (c) apertures thresholded by ImageJ software.	41
Figure 3.10 An Instron 8801 universal testing machine used for compressive tests.	41
Figure 3.11 Dimension of impedance tube based on ASTM E1050-98.	42
Figure 3.12 Schematic diagram of sound absorption test based on ASTM E1050-98 impedance tube method using two microphones.	43
Figure 3.13 Felt having thickness of 20 mm and weight of 2,000 g/m ² was used to determine the accuracy of the set-up of impedance tube.	44
Figure 3.14 Comparison of sound absorption coefficients of felt specimen between those obtained from manufacturer and impedance tube measurement [83].	44
Figure 4.1 Photographs of aluminium foams produced from infiltration of molten metal into the space holder of spherical preform sizes 4.1, 5.0, and 6.3 mm: (a) spongy, (b) dense and (c) sectioned aluminium foams.	45
Figure 4.2 Results of different pressure versus flow rate of air through mold with varying of drainage contained 6.3 mm diameter preform and 150 g inside are produced aluminium foams.	48
Figure 4.3 Gas permeability coefficient of molds having different drainage bases.	48
Figure 4.4 Infiltration types of open-cell aluminium foam structure: (a) no infiltration, (b) full infiltration with residue metal and (c) full infiltration without residue metal.	49
Figure 4.5 Defined zones of molten metal infiltration in space holder: A = residue metal, B = retained metal and C = infiltrate metal.	49

Figure 4.6 Photographs of 6.3 mm pore size aluminium foams produced using molds with drainage bases having different permeability (initial vacuum pressure, pouring temperatures and molten metal weight were kept constant as -100 kPa, 715 - 720 °C and 348 g, respectively).	51
Figure 4.7 Infiltration characteristic of 6.3 mm pore size aluminium foams produced using molds with drainage bases having different permeability (initial vacuum pressure, pouring temperatures and molten metal weight were kept constant as -100 kPa, 715 - 720 °C and 348 g, respectively).	52
Figure 4.8 Saturation and density of 6.3 mm pore size aluminium foams produced using molds with drainage bases having different permeability (initial vacuum pressure, pouring temperatures and molten metal weight were kept constant as -100 kPa, 715 - 720 °C and 348 g, respectively).	52
Figure 4.9 Aluminium foams produced using mold drainage type M3 (in Table 4.2) 31.26 K·10 ⁻¹² , 630 °C, -95 kPa: (a) before and (b) after space holder removal.....	54
Figure 4.10 Photographs of 4.1, 5.0 and 6.3 mm pore size aluminium foams produced using molds with drainage bases having permeability coefficients: (a) – (c) 31.26 x 10 ⁻¹² and (d) – (f) 44.35 x 10 ⁻¹² m ² (initial vacuum pressure, pouring temperature and molten metal weight were kept constant as -20 kPa, 620 °C and 353 g, respectively).	54
Figure 4.11 Infiltration characteristics of spongy aluminium foams produced using different spherical preform sizes (initial vacuum pressure, pouring temperatures, molten metal weight and mold permeability coefficient were kept constant as -20 kPa, 620 °C, 236 g and 44.35 x 10 ⁻¹² m ² respectively).	54
Figure 4.12 Infiltration characteristics of dense aluminium foams produced using different spherical preform sizes (initial vacuum pressure, pouring temperatures, molten metal weight and mold permeability coefficient were kept constant as -20 kPa, 620 °C, 233 g and 31.26 x 10 ⁻¹² m ² respectively).	55
Figure 4.13 Saturation of 4.1, 5.0 and 6.3 mm pore size aluminium foams produced using molds with drainage bases having permeability coefficients 31.26 x 10 ⁻¹² and 44.35 x 10 ⁻¹² m ² (initial vacuum pressure, pouring temperature and molten metal weight were kept constant as -20 kPa, 620 °C and 353 g, respectively).....	55
Figure 4.14 Photographs of 6.3 mm pore size aluminium foams produced using different initial vacuum pressures (mold permeability coefficient, pouring temperature and molten metal weight were kept constant as 44.35 x 10 ⁻¹² m ² , 725 °C and 353 g, respectively).	56
Figure 4.15 Infiltration characteristic of 6.3 mm pore size aluminium foams produced using different initial vacuum pressures (mold permeability coefficient, pouring temperature and molten metal weight were kept constant as 44.35 x 10 ⁻¹² m ² , 725 °C and 353 g, respectively).	57
Figure 4.16 Predicted threshold pressures of aluminium foams produced using different spherical preform diameters.....	57
Figure 4.17 Photographs of 6.3 mm pore size aluminium foams produced using different initial vacuum pressures (mold permeability coefficient, pouring temperatures	

and molten metal weight were kept constant as $31.26 \times 10^{-12} \text{ m}^2$, 620 - 630 °C and 221 g, respectively).....	58
Figure 4.18 Infiltration characteristic of 6.3 mm pore size aluminium foams produced using different initial vacuum pressures (mold permeability coefficient, pouring temperature and molten metal weight were kept constant as $31.26 \times 10^{-12} \text{ m}^2$, 620 – 630 °C and 221 g, respectively).....	59
Figure 4.19 Predicted and measured saturation of 6.3 mm pore size aluminium foams produced using different initial vacuum pressures (mold permeability coefficient, pouring temperatures and molten metal weight were kept constant as $31.26 \times 10^{-12} \text{ m}^2$, 620 - 630 °C and 221 g, respectively).....	59
Figure 4.20 Photographs of 6.3 mm pore size aluminium foams produced using different initial vacuum pressures (mold permeability coefficient, pouring temperature and molten metal weight were kept constant as $44.35 \times 10^{-12} \text{ m}^2$, 620 °C and 276 g, respectively).....	60
Figure 4.21 Infiltration characteristic of 6.3 mm pore size aluminium foams produced using different initial vacuum pressures (mold permeability coefficient, pouring temperature and molten metal weight were kept constant as $44.35 \times 10^{-12} \text{ m}^2$, 620 °C and 276 g, respectively).....	61
Figure 4.22 Predicted and measured saturation of 6.3 mm pore size aluminium foams produced using different initial vacuum pressures (mold permeability coefficient, pouring temperature and molten metal weight were kept constant as $44.35 \times 10^{-12} \text{ m}^2$, 620 °C and 276 g, respectively).....	61
Figure 4.23 Photographs of 6.3 mm pore size aluminium foams produced using different pouring temperatures (mold permeability coefficient, initial vacuum pressure and molten metal weight were kept constant as $44.35 \times 10^{-12} \text{ m}^2$, -100 kPa and 334 g, respectively).....	62
Figure 4.24 Infiltration characteristic of 6.3 mm pore size aluminium foams produced using different pouring temperatures (mold permeability coefficient, initial vacuum pressure and molten metal weight were kept constant as $44.35 \times 10^{-12} \text{ m}^2$, -100 kPa and 334 g, respectively).....	62
Figure 4.25 Density and saturation of 6.3 mm pore size aluminium foams produced using different pouring temperatures (mold permeability coefficient, initial vacuum pressure and molten metal weight were kept constant as $44.35 \times 10^{-12} \text{ m}^2$, -100 kPa and 334 g, respectively).....	63
Figure 4.26 Photographs of 6.3 mm pore size aluminium foams produced using different pouring temperatures (mold permeability coefficient, initial vacuum pressure and molten metal weight were kept constant as $31.26 \times 10^{-12} \text{ m}^2$, -95 kPa and 267 g, respectively).....	64
Figure 4.27 Infiltration characteristic of 6.3 mm pore size aluminium foams produced using different pouring temperatures (mold permeability coefficient, initial vacuum pressure and molten metal weight were kept constant as $31.26 \times 10^{-12} \text{ m}^2$, -95 kPa and 267 g, respectively).....	64

Figure 4.28 Saturation and density of 6.3 mm pore size aluminium foams produced using different pouring temperatures (mold permeability coefficient, initial vacuum pressure and molten metal weight were kept constant as $31.26 \times 10^{-12} \text{ m}^2$, -95 kPa and 267 g, respectively).....	65
Figure 4.29 Saturation and density of 6.3 mm pore size aluminium foams produced using different conditions.	65
Figure 4.30 Photographs of infiltrated aluminium foams having different infiltration type (type I: mold drainage type H2, pouring temperature 725 °C and initial vacuum pressure 0 kPa, type II: mold drainage type M3, pouring temperature 675 °C and initial vacuum pressure -95 kPa, and type III: mold drainage type H2, pouring temperature 650 °C and initial vacuum pressure -100 kPa).	66
Figure 4.31 Photographs of cross section along the infiltration length of an aluminium foam produced using mold drainage of M3 type, spherical preform size of 4.1 mm, pouring temperature of 620 °C and initial vacuum pressure of -20 kPa.....	68
Figure 4.32 Photographs of cross section along the infiltration length of an aluminium foam produced using mold drainage of H2 type, spherical preform size of 4.1 mm, pouring temperature of 620 °C and initial vacuum pressure of -20 kPa.....	69
Figure 4.33 Density distribution of aluminium foams measured from bottom to top in vertical axis: (a) – (c) spongy and (e) – (f) dense structure of the foams produced using spherical preform sizes 4.1, 5.0 and 6.3 mm.	70
Figure 4.34 Porosity distribution of aluminium foams measured from bottom to top in vertical axis: (a) spongy and (b) dense structure of the foams produced using spherical preform sizes 4.1, 5.0 and 6.3 mm.....	71
Figure 4.35 Spongy aluminium foam: (a) photograph, (b) x-ray and (c) CT-scan images.	71
Figure 4.36 μ CT images of 6.3 mm spherical preforms after packing in plaster mold: vibrated time 60 s, weight 150 g: (a) top view and (b) front view.	71
Figure 4.37 Saturation and density of 6.3 mm pore size aluminium foams produced using different conditions.	72
Figure 4.38 Size distribution of apertures of dense aluminium foams produced using infiltration method with conditions given in Table 4.3 for preform sizes: (a) 4.1, (b) 5 and (d) 6.3 mm.....	73
Figure 4.39 Predicted and measured apertures of dense aluminium foams produced using infiltration method with conditions given in Table 4.3 for preform sizes: (a) 4.1, (b) 5 and (d) 6.3 mm.	73
Figure 4.40 Compressive stress-strain curves of dense aluminium foams produced by preforms having mean spherical diameters 4.1, 5.0 and 6.3 mm and molds having permeability coefficient of $31.26 \times 10^{-12} \text{ m}^2$	74
Figure 4.41 Compressive stress-strain curves of aluminium foams produced by preforms having mean spherical diameters 4.1, 5.0 and 6.3 mm and molds having permeability coefficient of $44.35 \times 10^{-12} \text{ m}^2$	75
Figure 4.42 Compressive stress-strain curve of a dense aluminium foam produced by preforms having a mean spherical diameter of 4.1 mm and a mold having permeability	

coefficient of $31.26 \times 10^{-12} \text{ m}^2$ (Inset photographs showed the foam specimen at different strains during compression). 76

Figure 4.43 Compressive stress-strain curve of a spongy aluminium foam produced by preforms having a mean spherical diameter of 4.1 mm and a mold having permeability coefficient of $44.35 \times 10^{-12} \text{ m}^2$ (Inset photographs showed the foam specimen at different strains during compression). 76

Figure 4.44 Plots of relative Young's modulus (and Young's modulus) against relative density of the produced aluminium foams shown in **Table 4.5**. 78

Figure 4.45 Plots of relative plateau stress (and plateau stress) against relative density of the produced aluminium foams shown in **Table 4.5**. 78

Figure 4.46 Plots of Young's modulus against density of currently-available metal foams [86] (Black symbols) and this work aluminium foams (Red symbols) shown in **Table 4.5** (Numbers in parentheses are densities in Mg/m^3). 79

Figure 4.47 Plots of $\sigma_c/23/\rho$ against $E/12/\rho$ of currently-available metal foams [86] (Black symbols) and this work aluminium foams (Red symbols) shown in **Table 4.5** (Numbers in parentheses are densities in Mg/m^3). $E/12/\rho \sigma_c/23/\rho$ 79

Figure 4.48 Plots of energy absorption at densification against plateau stress of currently-available metal foams [86] (Black symbols) and this work aluminium foams (Red symbols) shown in **Table 4.5** (Numbers in parentheses are densities in Mg/m^3). 80

Figure 4.49 Effect of pore size on sound absorption of aluminium foams with sample thickness of 8 mm. 82

Figure 4.50 Effect of pore size on sound absorption of aluminium foams with sample thickness of 25 mm. 82

Figure 4.51 Effect of pore size on sound absorption of aluminium foams with sample thickness of 50 mm. 83

Figure 4.52 Effect of sample thickness on sound absorption coefficient of aluminium foams pore size 4.1 mm (no an air gap cavity). 83

Figure 4.53 Effect of sample thickness on sound absorption coefficient of aluminium foams pore size 5 mm (no an air gap cavity). 84

Figure 4.54 Effect of sample thickness on sound absorption coefficient of aluminium foams pore size 6.3 mm (no an air gap cavity). 84

Figure 4.55 Effect of sample porosity (%) on sound absorption coefficient of aluminium foams pore size 4.1 mm with thickness of 8 mm (no an air gap cavity). .. 85

Figure 4.56 Effect of sample porosity (%) on sound absorption coefficient of aluminium foams pore size 4.1 mm with thickness of 50 mm (no an air gap cavity). 85

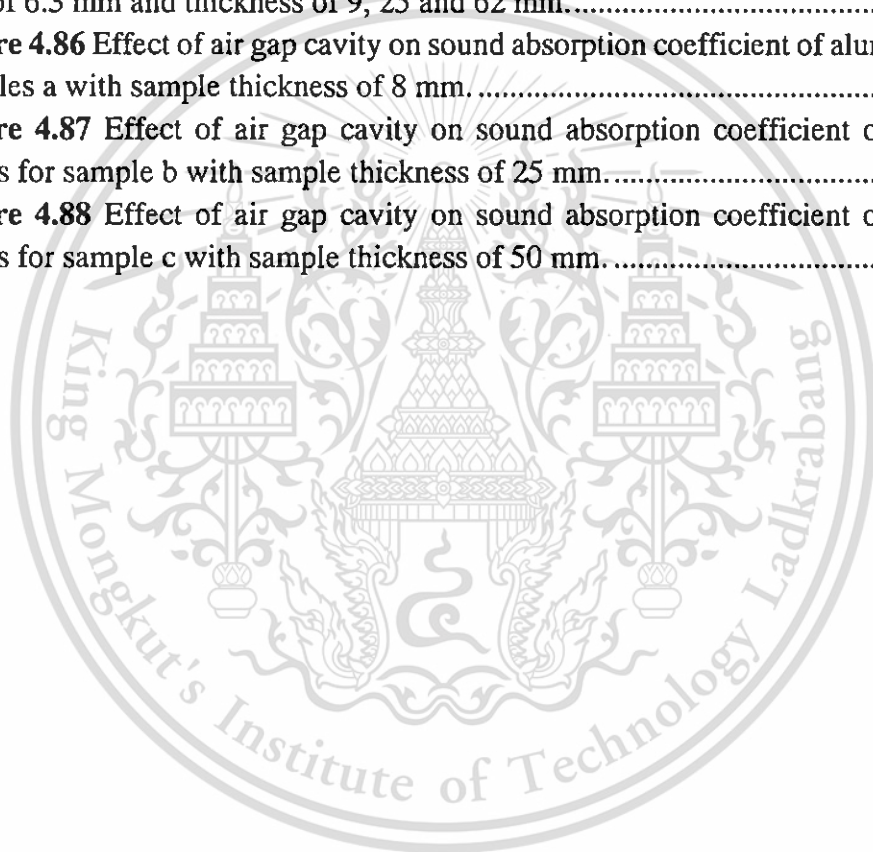
Figure 4.57 Effect of sample porosity (%) on sound absorption coefficient of aluminium foams pore size 5 mm with thickness of 8 mm (no an air gap cavity). 86

Figure 4.58 Effect of sample porosity (%) on sound absorption coefficient of aluminium foams pore size 5 mm with thickness of 50 mm (no an air gap cavity). ... 86

Figure 4.59 Effect of sample porosity (%) on sound absorption coefficient of aluminium foams pore size 6.3 mm with thickness of 8 mm (no an air gap cavity). .. 87

Figure 4.60 Effect of sample porosity (%) on sound absorption coefficient of aluminium foams pore size 6.3 mm with thickness of 50 mm (no an air gap cavity).	87
Figure 4.61 Measured and predicted sound absorption coefficients of aluminium foam a (denoted in Table 4.6) with thickness of 8.4 mm.	90
Figure 4.62 Measured and predicted sound absorption coefficients of aluminium foam b (denoted in Table 4.6) with thickness of 24.85 mm.	90
Figure 4.63 Measured and predicted sound absorption coefficients of aluminium foam c (denoted in Table 4.6) with thickness of 55.85 mm.	91
Figure 4.64 Measured and predicted sound absorption coefficients of aluminium foam d (denoted in Table 4.6) with thickness of 115.22 mm.	91
Figure 4.65 Measured and predicted sound absorption coefficients of aluminium foam e (denoted in Table 4.6) with thickness of 172.98 mm.	92
Figure 4.66 Measured and predicted sound absorption coefficients of aluminium foam f (denoted in Table 4.6) with thickness of 229.25 mm.	92
Figure 4.67 Measured and predicted sound absorption coefficients of aluminium foam g (denoted in Table 4.6) with thickness of 281.19 mm.	93
Figure 4.68 Measured and predicted sound absorption coefficients of aluminium foam h (denoted in Table 4.6) with thickness of 8.49 mm.	93
Figure 4.69 Measured and predicted sound absorption coefficients of aluminium foam i (denoted in Table 4.6) with thickness of 24.97 mm.	94
Figure 4.70 Measured and predicted sound absorption coefficients of aluminium foam j (denoted in Table 4.6) with thickness of 60.52 mm.	94
Figure 4.71 Measured and predicted sound absorption coefficients of aluminium foam k (denoted in Table 4.6) with thickness of 125.94 mm.	95
Figure 4.72 Measured and predicted sound absorption coefficients of aluminium foam l (denoted in Table 4.6) with thickness of 186.46 mm.	95
Figure 4.73 Measured and predicted sound absorption coefficients of aluminium foam m (denoted in Table 4.6) with thickness of 251.62 mm.	96
Figure 4.74 Measured and predicted sound absorption coefficients of aluminium foam n (denoted in Table 4.6) with thickness of 8.51 mm.	96
Figure 4.75 Measured and predicted sound absorption coefficients of aluminium foam o (denoted in Table 4.6) with thickness of 24.83 mm.	97
Figure 4.76 Measured and predicted sound absorption coefficients of aluminium foam p (denoted in Table 4.6) with thickness of 61.98 mm.	97
Figure 4.77 Measured and predicted sound absorption coefficients of aluminium foam q (denoted in Table 4.6) with thickness of 127.58 mm.	98
Figure 4.78 Measured and predicted sound absorption coefficients of aluminium foam r (denoted in Table 4.6) with thickness of 194.19 mm.	98
Figure 4.79 Measured and predicted sound absorption coefficients of aluminium foam s (denoted in Table 4.6) with thickness of 260.06 mm.	99
Figure 4.80 Difference between measurement and prediction of sound absorption coefficients of aluminium foams having thicknesses 252 – 281 mm with different pore/aperture ratios.	99

Figure 4.81 Difference between measurement and prediction of sound absorption coefficients of aluminium foams having thicknesses 173 to 194 mm (unit cell 28 - 39) with different pore sizes.....	100
Figure 4.82 Difference between measurement and prediction of sound absorption coefficients of aluminium foams having thicknesses 252 to 281 mm (unit cell 46 - 63) with different pore sizes.....	100
Figure 4.83 Measured sound absorption coefficient of aluminium foams having pore size of 4 mm and thickness of 8, 25 and 56 mm.....	101
Figure 4.84 Measured sound absorption coefficient of aluminium foams having pore size of 5 mm and thickness of 8, 25 and 61 mm.....	102
Figure 4.85 Measured sound absorption coefficient of aluminium foams having pore size of 6.3 mm and thickness of 9, 25 and 62 mm.....	102
Figure 4.86 Effect of air gap cavity on sound absorption coefficient of aluminium foam samples a with sample thickness of 8 mm.	103
Figure 4.87 Effect of air gap cavity on sound absorption coefficient of aluminium foams for sample b with sample thickness of 25 mm.....	103
Figure 4.88 Effect of air gap cavity on sound absorption coefficient of aluminium foams for sample c with sample thickness of 50 mm.	104



LIST OF SYMBOLS

SYMBOLS		UNIT
A	Cross-sectional area of specimen	(cm ²)
A _p	Diameter of aperture size	(mm)
c ₀	Speed of sound	(m/s)
d	Diameter of the tube	(m)
D	Diameter of pore size	(mm)
f	Frequency	(Hz)
f _l	Lower working frequency of the tube	(Hz)
f _u	Upper working frequency of the tube	(Hz)
H ₁₂	Transfer function	
H _i	Transfer function of incident wave alone	
H _r	Transfer function of reflected wave alone	
k ₀	Wave number	(m ⁻¹)
K	Constant of tube diameter which is 0.586	
K	Permeability	(m ²)
l _{st}	Strut length	(m)
L	Length of specimen	(m)
L _p	Sound pressure level	(dB)
m	Weight of aluminium foam	(g)
M ₀	Reactance of pore opening between pores	
n	Number of pores	
p	Root mean square sound pressure	(Pa)
p _{ref}	Reference sound pressure	(Pa)
p ₁ and p ₂	Complex sound pressure of the incident and reflected waves at location x ₁ and x ₂	
P	Applied pressure	(Pa)
P _b	Bubbling pressure	(Pa)
P _f	Pressure drop	(Pa)
P _{th}	Threshold pressure	(Pa)
P _γ	Capillary pressure	(Pa)
Q	Volumetric flow rate	(cm ³ /sec)
r	Radius of spherical pore diameter	(μm)
r	Normal incidence reflection factor	

r_e	Radius of pore diameter	(m)
R_0	Specific acoustic resistance	
S	Distance between microphones	(m)
S	Saturation	(%)
t	Cell wall thickness	(mm)
t_0	Initial temperature of space holder	(°C)
t_{st}	Strut thickness	(m)
T_0	Initial temperature of molten metal	(°C)
T_E	Solidification at temperature	(°C)
v	Volume of aluminium foam	(cm ³)
V	Fluid velocity	(l/min)
V_m	Volume fraction of metal	
V_r	Volume fraction of preforms	
W	Energy absorption	(MJ·m ⁻³)
$Wt\%$	Percentage by weight	(%)
x_1 and x_2	Microphone location	(m)
Z_D	Specific acoustic impedance of air inside a cell	
Z_n	Acoustic impedance of acoustic system	

GREEK

ΔP	Pressure drop	(Pa)
ΔL	Infiltration distance	(m)
Ω	Porosity	(%)
α	Sound absorption coefficient	
β	Inertial parameter	
ε	Measured porosity	(%)
ε_d	Densification strain	(g/cm ³)
θ	Contact angle between liquid and solid interface	(Degree)
λ	Pore size distribution index	
μ	Viscosity of the fluid	(kg/m·s)
ρ	Density of the fluid	(kg/m ³)
ρ_0	Theoretical density	(g/cm ³)
ρ^*	Density of foam	(g/cm ³)
ρ_s	Measured density	(g/cm ³)

This material is restricted to personal use only, not allowed for commercial use.

Forbidden to modify the content, and cite the document when use.

$\bar{\rho}$	Relative density	
σ_{LV}	Liquid-vapour surface tension	(N/m)
σ_{pl}	Plateau stress	(MPa)
σ_y	Yield stress	(MPa)
ω	Angular velocity	rad/s
ϕ_{in}	Inside diameter	(m)



LIST OF TECHNICAL VOCABULARY AND ABBREVIATION

ACRONYMS

B&W	Black and white
CT	Computed tomograph
D	Degree of drainage
dpi	Dots per inch
DSLR	Digital single lens reflex
E	Young's modulus
FF	Free field
NAC	Noise absorption coefficient
NI	National Instruments
NRC	Noise reduction coefficient
P	Pressure field
P	Infiltration pressure
RF	Random field
SPL	Sound pressure level

ABBREVIATIONS

Al	Aluminium
Cu	Copper
Fe	Iron
Mg	Magnesium
Mn	Manganese
NaCl	Sodium chloride
PU	Polyurethane
Si	Silicon
SiC	Silicon carbide
SiCp	Silicon carbide particle
Ti	Titanium
Zn	Zinc

CHAPTER 1 INTRODUCTION

1.1 Background

Noise pollution is one of the primary concern in automotive design. The hearing of too loud noise for a long time can deteriorate the hearing ability and the mental health of humans. Consequently, one should avoid hearing too loud noise, otherwise, some preventive method should be taken into account. Daily communication requires an enormous number of journeys which undoubtedly make noise pollution to some extent depending on the type of vehicles.

In addition to surrounding sounds from outside, loud noise could occur from several components of a vehicle, such as power train, exhaust system, tyres and wind, which generate noise to a vehicle compartment. The vehicle compartment is similar to a living room where calmness is highly desirable for a driver and passengers. Automotive manufacturers have attempted to make a car as quiet as possible in order to satisfy their customers. The calmness within the compartment is one of the selling points of a car. Sound absorption is a prime solution for acquiring the low sound requirement. Competent materials eligible for sound absorption purpose are those of which contain porous structure such as polyester, glass fiber, urethane and aluminium foam. The last porous material has excellent properties especially suitable for sound absorption applications due to its good capability and stability of sound absorption, environmentally friendly property, and human harmlessness during both production and usage. These properties of aluminium foam are better than those of fiberglass and poly-urethane foams which are most used sound absorption materials. The use of aluminium foam, however, has limited due to its high sale prices. A combination of product cost and sound absorption property of a sound absorption material is a selective criterion for crucial decision made by a car maker.

The purpose of this study is to develop a low cost aluminium foam panel for sound absorption applications in road vehicles. Cheaper raw materials, which can be used for producing aluminium foams with controllable pore sizes, optimised manufacturing conditions and proper installation will be the key elements of this research. The results from this work will benefit for both car makers and customers.

1.2 Objectives

- To optimise manufacturing conditions to receive a determinative control of aluminium foam structure for good sound absorption at a specified range of frequency.
- To determine the effect of different installation on sound absorption properties of aluminium foam panels.
- To evaluate the use of aluminium foam panel for sound absorption in road

This material is provided for educational use only, not allowed for commercial use.

Forbidden to modify the content, and cite the document when use.

1.3 Scope of Research

- To produce aluminium foams with different pore size, porosity and thickness using a vacuum infiltration method.
- To measure sound absorption coefficients of aluminium foams having different structure and installation, and compare them with theoretical models.

1.4 Thesis Outline

The thesis is arranged in 5 chapters, the contents of which are summarised as follows.

Chapter 1: Introduction

This chapter introduces the general background of noises in road vehicle including noise sources and absorbent materials. The crucial idea of car manufacturer designs and a quality of car for customer satisfaction are presented. In addition, objectives of this study, and scope carrying out into research are presented in this chapter.

Chapter 2: Literature Review

This chapter explains the fundamental theory of noises, noise control methods in vehicle, and sound absorption characteristic of porous materials. The production parameters, influencing on sound absorption, of open cell aluminium foams are summarised from previous studies. Furthermore, prediction models of production parameters and sound absorption performance are presented for comparing results of experiments and predictions.

Chapter 3: Experimental Procedure

This chapter explains in details the space holder method for open cell aluminum foam production. The aluminium foam production parameters including gas permeability through mold drainage, initial infiltration pressure and melt temperature are varied in order to investigate the correlation between production parameters and foam structures. Sample characterisation methods including related equations to calculate, specifications of equipment and operating methods are also explained in this chapter.

Chapter 4: Results and Discussion

This chapter shows the results of open cell aluminium foam structures produced in various investigation parameters including their mechanical and acoustical properties. Some aluminium foam specimens are chosen to measure acoustical properties and optimise sound absorption performance with varying installation methods. Their results are compared with prediction models and physical equations.

Chapter 5: Conclusions and Suggestions

The obtained results from this research are concluded. Suggestions of experiments that are benefit in the future research are recommended in this chapter.

CHAPTER 2 LITERATURE REVIEW

2.1 Noises in Vehicles

2.1.1 Type of Noises in Vehicles

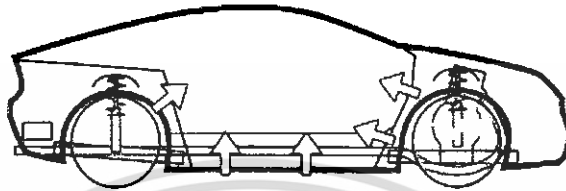


Figure 2.1 Transfer paths of airborne noise in a car [1].

Noise in vehicles can be divided into two types: airborne and structure-borne noises. Airborne noise is a sound pressure level which can be transferred only via the air as shown for example of airborne noise in a car in Figure 2.1 [1]. It can be reduced by installation of absorptive materials.

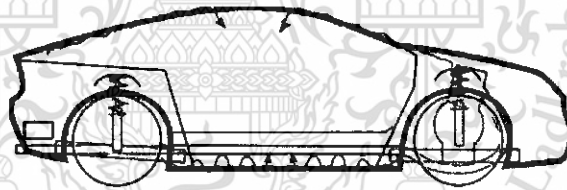


Figure 2.2 Transfer paths of structure-borne noise in a car [1].

Structure-borne noise in a car occurs by vibration sources of structure or automotive components transmitting into a passenger compartment. Figure 2.2 shows an example of the structure-borne noise occurred during driving by suspension components excitation [1].

2.1.2 Noises and Their Sources in Vehicles

Figure 2.3 shows various sound sources producing noises transmitting through the passenger compartment of a car [2]. They can be classified according to type, source and frequency of noises as shown in Figure 2.4 [3]. Lu [4] measured noise in sound pressure level which transmitted through a passenger compartment at the front passenger right ears versus frequency. A range of high sound pressure levels of 50 – 90 dB occurs at frequencies 0 – 2,000 Hz and gradually decreases at higher frequencies,

as shown in Figure 2.5 [4]. Similar results of high sound pressure level occurring at frequencies less than 2,000 Hz were reported [5-8]. Putner *et al.* showed that the highest sound pressure level occurred at the engine and the rear axle of a car [5].

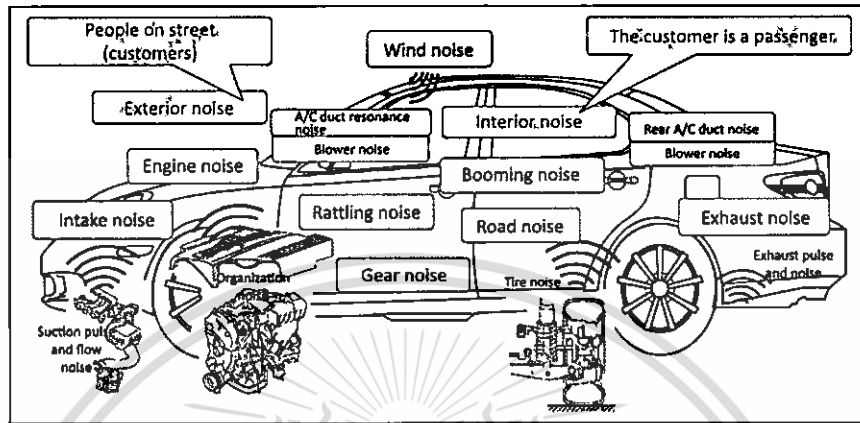


Figure 2.3 Noises transmitting through a car compartment and their sources [2].

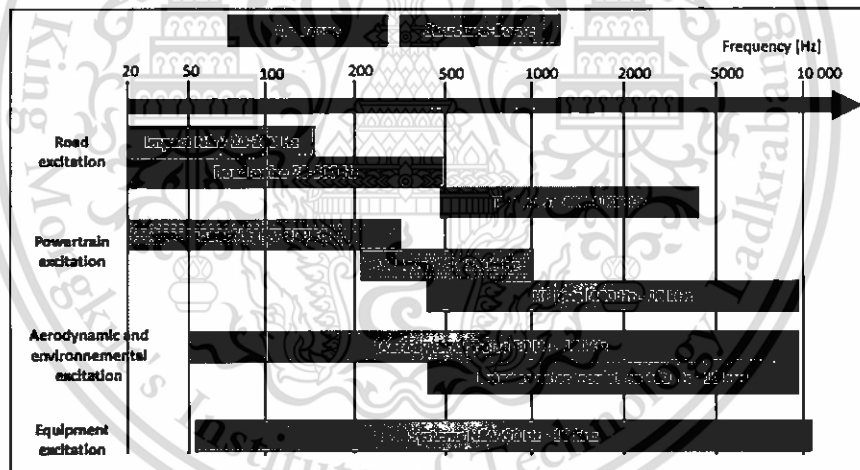


Figure 2.4 Noises in an automotive vehicle classified by type, source and frequency [3].

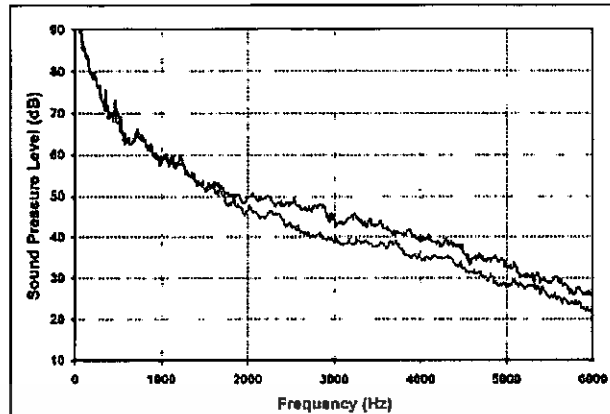


Figure 2.5 Interior sound pressure level at the front right ear (Dark and light traces represent for vehicles with standard and acoustic windshield, respectively) [4].

2.1.3 Interior Sound Design for Vehicles

Sound level is one of car design aspects concerning for health of driver/passenger. Basically, level of sound inside a vehicle should not exceed permissible levels of noise as can be seen in **Table 2.1** [6]. Moreover interior noise at low level can guarantee reliability, safety and comfort of the vehicle. Recent automotive manufactures have designed their component parts or systems in the way to reduce noises in a passenger compartment. For example, the recent Volkswagen Golf VI car [7], a new soft sound injection pump and a new sound insulation and damping package were developed for noise reduction in a common rail engine. In addition, in order to reduce rolling noise, an engine mounting system was moved to locate near a torque roll axis [5]. The geometry and material of windshield mirror was also redesigned to attenuate an aerodynamic noise [4].

Table 2.1 Recommendations for permissible sound level inside motor vehicles [6].

<i>Motor vehicle</i>	<i>Permissible levels of noise, dB (A) †</i>
Motor vehicles for transportation of passengers	
Categories M₁ and M₂	
(a) at the driver's seat	78
(b) in the passenger compartment of class B, II and III buses	80
(c) in the passenger compartment of class A and I buses	82
Categories M₂ and M₃ with the engine located in front of adjacent to the driver's seat, including special purpose buses manufactured on the chassis of trucks	80
Motor vehicles for transportation of goods	
Category N ₁ with a laden mass up to 2000 kg	80
Category N ₁ with a laden mass from 2000 kg up to 3500 kg	82
Categories N ₂ and N ₃	82
Categories N ₂ and N ₃ (trucks with a sleeping berth)	80
Semitrailers for transportation of passengers	80
Trolley-buses	
(a) at the driver's seat	78
(b) in the passenger compartment	82
Vehicles with the pneumatic braking system, when the compressed air is discharged from the pneumatic valves after the actuation of brakes	70

2.2 Noise Control in Vehicles

2.2.1 Noise Control Mechanisms

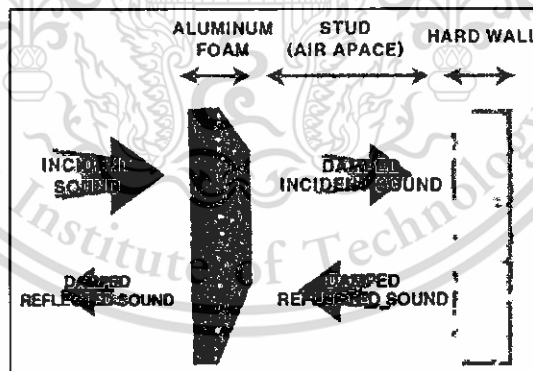


Figure 2.6 Schematic diagram of sound absorption mechanism by aluminium foam panel [8].

Sound is a mechanical wave which is an oscillation of pressure transmitted through a solid, liquid or gas. It composes of frequencies within the range of hearing and of level sufficiently strong to be heard, or the sensation stimulated in organs of hearing by such vibrations [9].

Sound pressure in a given medium is the difference between average local pressure and the pressure in the sound wave. As the human ear can detect sounds with a wide range

of amplitudes, sound pressure is often measured as a level on a logarithmic decibel scale. The sound pressure level (SPL), L_p , is defined as

$$L_p = 10 \log_{10} \left(\frac{p^2}{p_{ref}^2} \right) = 20 \log_{10} \left(\frac{p}{p_{ref}} \right) \quad (2.1)$$

where p is the root mean square sound pressure and p_{ref} is a reference sound pressure [9]. Examples of L_p and corresponding p are shown in **Table 2.2** [10]. The sound level depends on the distance between the sound source and the place of measurement. When a sound passes through an absorptive material, its energy is converted to heat by the viscous friction of air in the absorptive material. **Figure 2.6** shows, for example, the absorption of sound by an aluminium foam panel having a wall at the back with an air space in between [8]. When an incident sound passes through the aluminium foam panel, a part of sound energy is absorbed by the aluminium foam panel. The remained sound subsequently reflects the wall and passes through the aluminium foam panel again. Therefore sound energy is absorbed by the aluminium foam panel two times.

Table 2.2 Sound pressure level and corresponding sound pressure [10].

Sound pressure level L_p	Sound pressure p
140 dB SPL	200 Pa
137.5 dB SPL	150 Pa
134 dB SPL	100 Pa
130 dB SPL	63 Pa
120 dB SPL	20 Pa

2.2.2 Noise Control Methods

There are three main methods for noise control in passenger compartment of an automotive vehicle: re-design or adjust component parts to reduce noise from noise sources, use sound absorptive materials and add sound source to noise cancellation. **Figure 2.7** shows noise reduction methods; reduction, absorption and block, in components at positions of a vehicle in relation to type of noises [11]. Examples of automotive components having sound absorptive materials installed are shown in **Figure 2.8** [12].

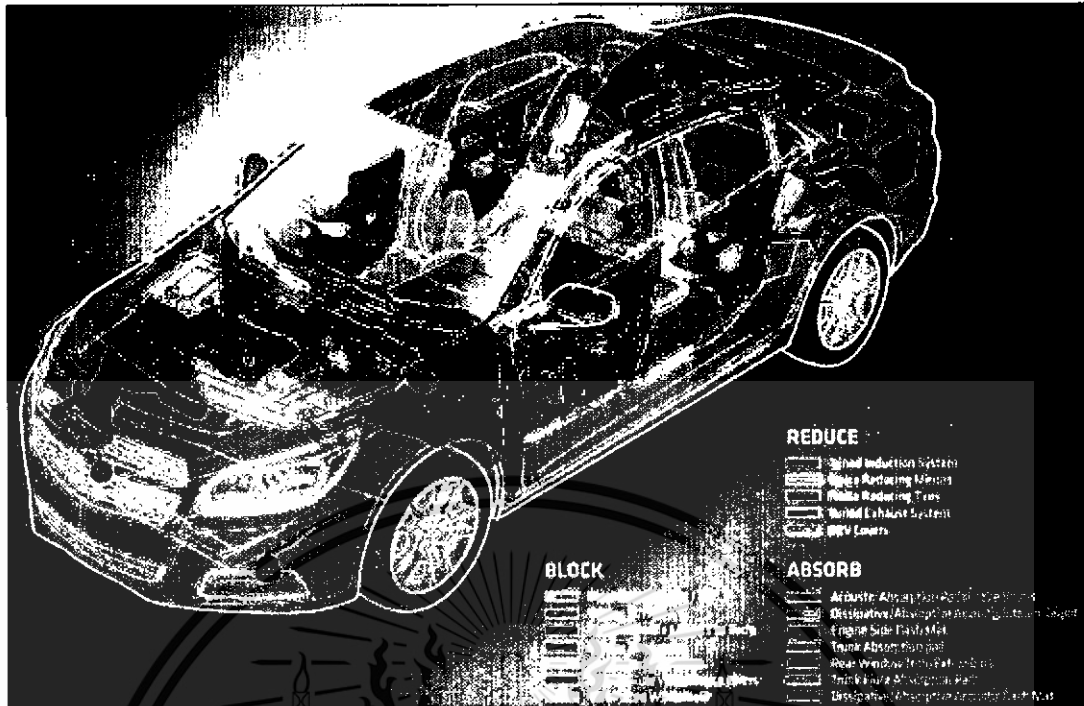


Figure 2.7 Methods of noise reduction in automotive components: reduce, absorb and block [11].


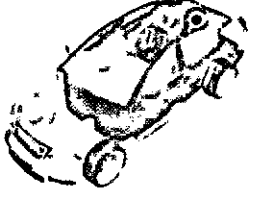




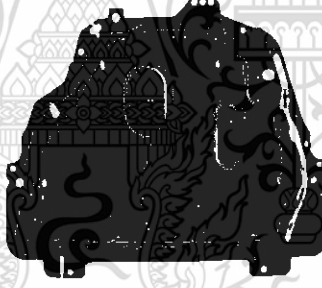



Automotive components	Materials	Feature of sound absorption materials	Installation location
Parcel tray	Lightweight microfiber		
Spare tyre cover	Felt		
A-Pillar	Lightweight microfiber		
Engine under cover	Felt		
Fender liner	Felt		

Figure 2.8 Installation of sound absorption materials in automotive components [12].

2.2.3 Materials for Noise Control

There are three main types of porous absorptive materials, which are classified by structure, named as cellular, fibrous and granular, as shown in

Figure 2.9 [13]. Performance of sound absorption of current materials used in some automotive components is shown in **Figure 2.10** [14], [15]. It can be observed that

This material is reserved for educational use only, not allowed for commercial use.

Forbidden to modify the content, and cite the document when use.

sound absorption coefficients at frequency ranges 125 - 1,000 Hz of the materials currently available in the market in **Figure 2.10** is low compared with those at higher frequencies. Consequently, noises that generating in the range of low frequencies are still little absorbed by the current absorptive materials, particularly for fibrous materials.

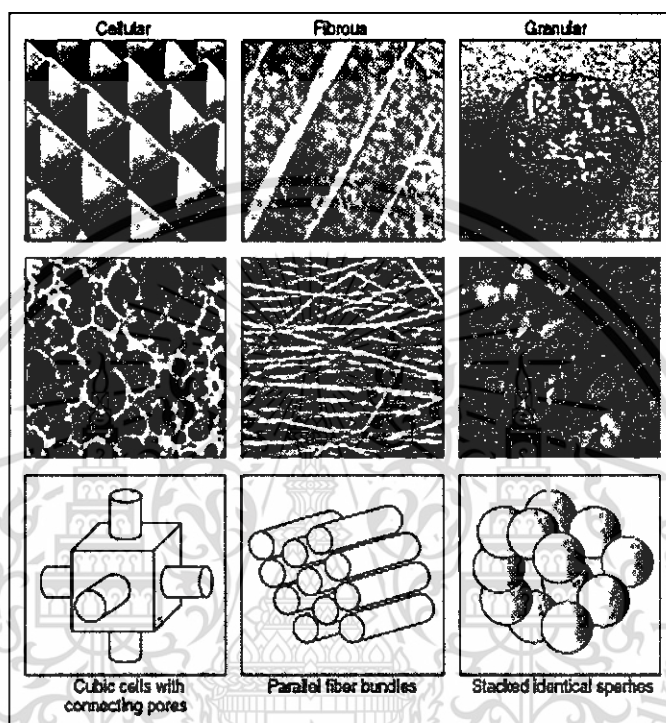
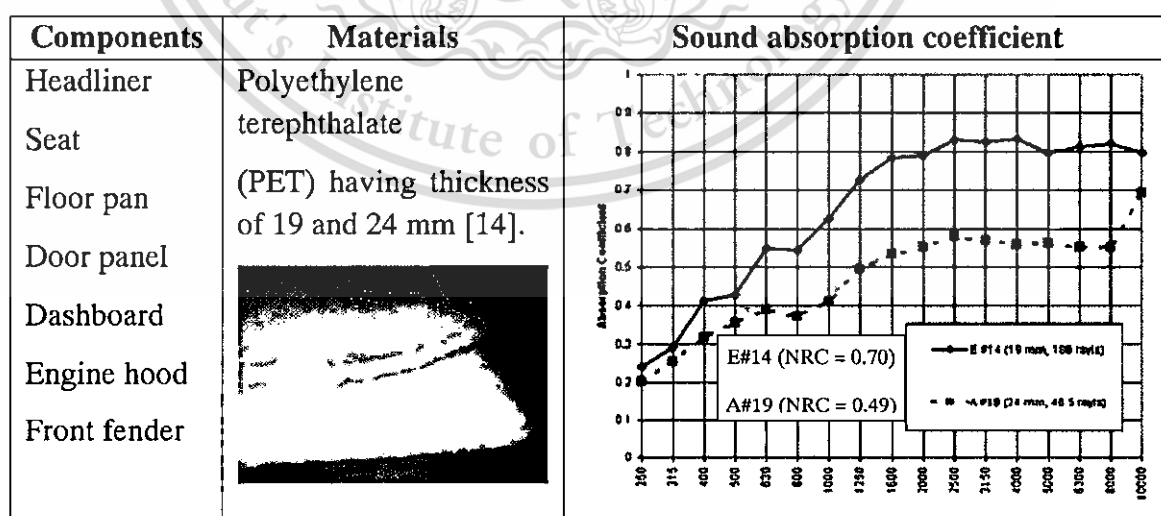


Figure 2.9 Three main types of porous absorption materials [13].



This material is reserved for educational use only, not allowed for commercial use.

Forbidden to modify the content, and cite the document when use.

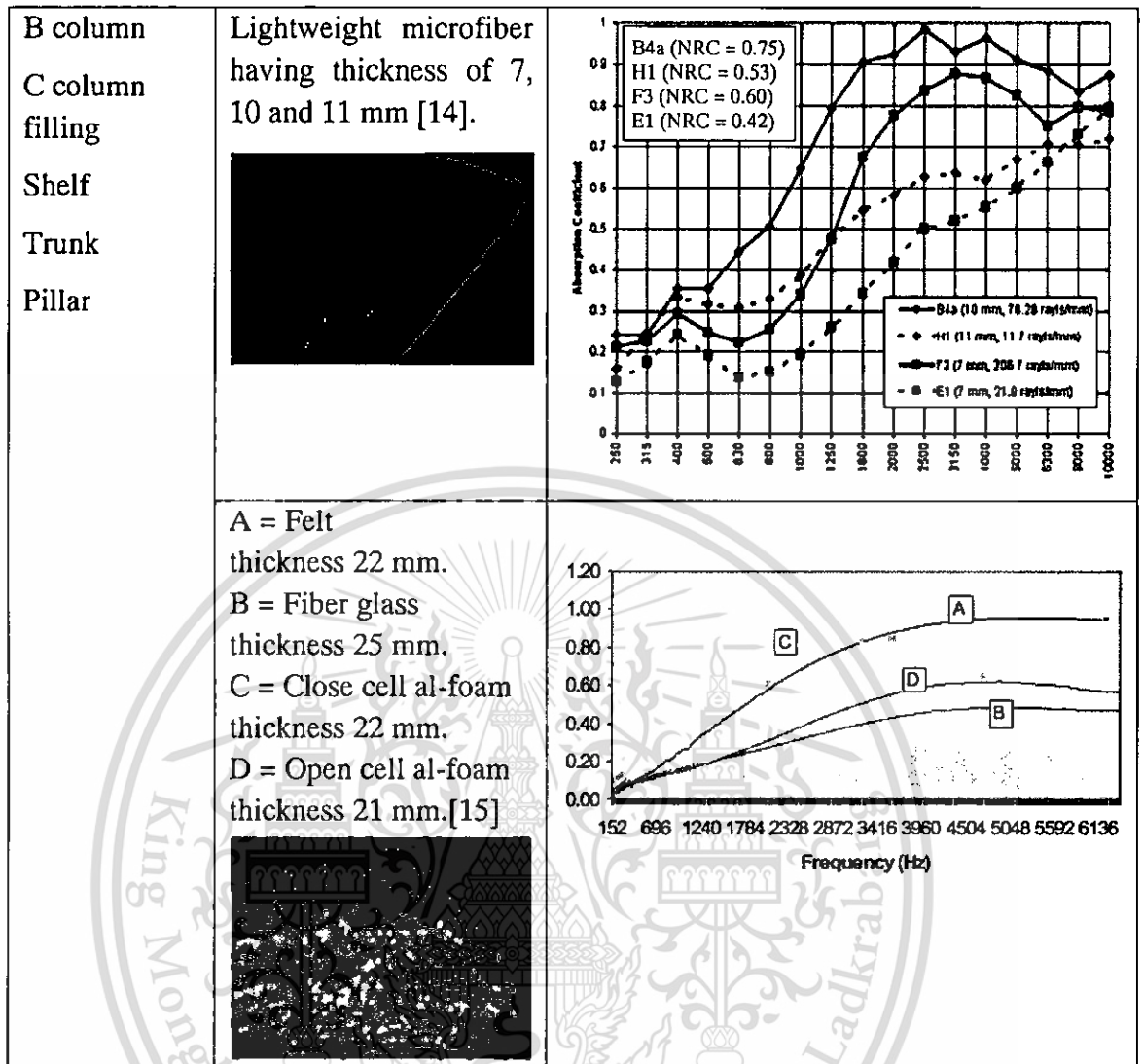


Figure 2.10 Sound absorptive materials in automotive vehicle components.

2.3 Fundamental of Open Cell Aluminium Foam

2.3.1 Parameters of Open Cell Aluminium Foam Structure

Structure of open cell aluminium foams consists of unit cells with interconnectivity. Each of the unit cells is randomly arranged in different geometries and sizes which depend on production method. Structural parameters of open cell aluminium foams can be described as follows: density, porosity, pore size, aperture size (shown in Figure 2.11 [16]), strut shape and strut morphology. Production methods and related parameters of open cell aluminium foams will be described in Sections 2.4 - 2.5.

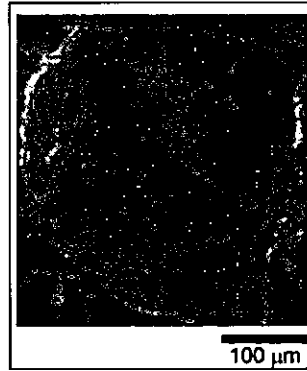


Figure 2.11 Enlargement of cell wall showing the presence of apertures [16].

2.3.2 Applications of Open Cell Aluminium Foam

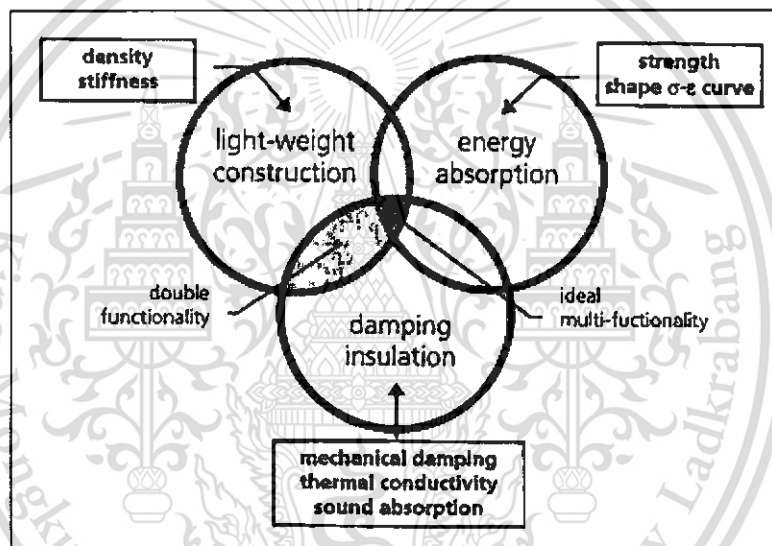


Figure 2.12 Main automotive applications of metallic foams [17].

Open cell aluminium foams have multifunctional properties namely noises attenuation, light-weight construction and energy absorption which can be used in automotive applications as shown in Figure 2.12 [17]. Open cell aluminium foams have been used in four main applications [18], [19] and [20] as shown in Figure 2.13. Apart from automotive applications, open cell aluminium foams can be used in other applications, for example, aerospace industry, decoration and arts [21]. Four main applications of open cell aluminium foams are described below.

- **Light-weight construction:** the structure of open cell aluminium foams having low density and high stiffness have been used for weight reduction.
- **Energy absorption:** open cell aluminium foams having like sponge behavior with mechanical stiffness and energy absorbing have been used as bumpers of vehicles.

This material is reserved for educational use only, not allowed for commercial use.

Forbidden to modify the content, and cite the document when use.

- Thermal control: open cell aluminium foams having high surface area and unit cell have been used as heat exchangers.
- Acoustic absorption: porous structure of open cell aluminium foam have been used for sound absorption particularly in high temperature and outdoor applications.

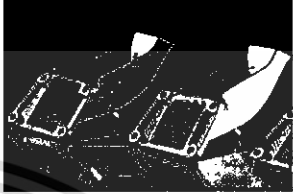
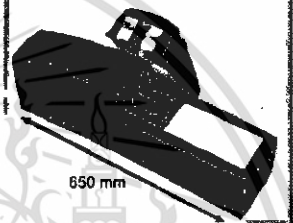
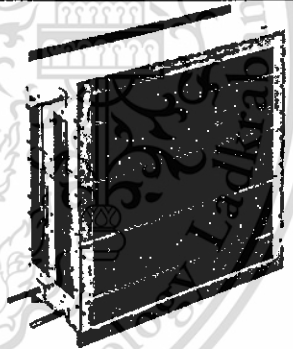

Applications	Samples
Light-weight construction: BMW engine mounting bracket.	 <p data-bbox="859 732 1006 754">Courtesy of LKR</p>
Energy absorption: crash energy absorber for a tram built for the COMBINO vehicle system.	 <p data-bbox="859 990 1104 1041">Courtesy of hubner, Schunk, Siemens</p>
Thermal control: heat-exchange medium for the space shuttle atmospheric control system.	 <p data-bbox="931 1402 1078 1424">Courtesy of ERG</p>
Acoustic absorption: sound absorbing underside of highway bridge	

Figure 2.13 Applications of open cell aluminium foams [18].

2.4 Production Methods of Open Cell Aluminium Foam

2.4.1 Space Holder Method

There are several methods to produce open cell foams, which are summarised in reference [17]. The space holder method is one of liquid state processing methods

whose equipment set-up is simple. Moreover, this method can precisely control pore size and porosity of foam structure by controlling infiltration of liquid metal into space locating among specific size of space holder. Garcia and Cordovilla [22] summarised the important factors of infiltration process on structural parameters which occur from infiltration phenomenon at different production conditions as described below.

- Space holder (size, shape and surface roughness)
- Liquid metal (surface tension and viscosity)
- Liquid/solid interface (contact angle and reactivity)
- Production parameters (applied pressure, pouring temperature and gas permeability)

These factors influencing on structure and physical properties of open cell aluminium foams. For example, increasing infiltration pressure provides increased density, while, higher compact of space holder density decreases density of foams [23], [24]. Although factors of space holder have all been investigated, some production parameters such as gas permeability have not yet studied.

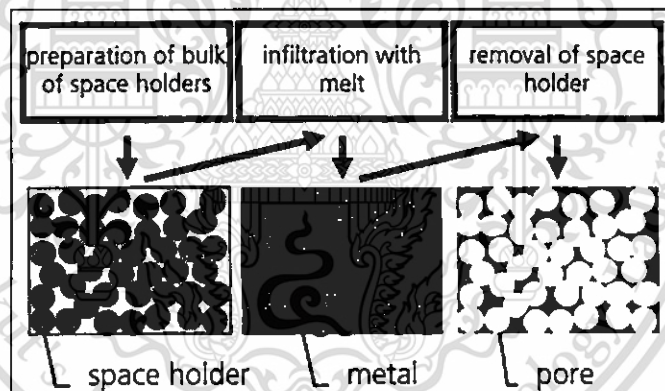


Figure 2.14 Production of cellular metallic materials using space-holder fillers [17].

Figure 2.14 shows the schematic diagram of space holder method for producing open cell aluminum foams [17]. This method can be achieved in three steps:

1. Preparation of space holders: space holders can be made from organic or inorganic substances which can withstand the high melting temperature of metals; moreover, space holders should be leachable in water or solvents. Space holders are mostly produced in a spherical shape made from different processes and raw materials [25], [26]. The porosity of a produced foam is an inverse structure of space holders. Therefore, porosity of the foam is controllable by controlling the level of packing of the space holders [27]. Both size and number of aperture in foam structure can be increased by increasing compact density of

space holder. Chou *et al.* [28] reported that the porosity of their foams increased with decreasing space holder diameter as shown in **Figure 2.15**.

2. Infiltration with molten metal: several metals, such as aluminium, copper, titanium, steel and stainless etc, can be used. In order to fill a molten metal in the interconnectivity of space holders completely, pressure has been often used.
3. Removal of space holders: space holder can be removed after the solidification of molten metal using ultrasonic vibration, hot water, water jet, or solvent depending on the type of space holders. Jinnapat [23] reported that high density of space holder made from salt dissolved rapidly at low pressure, but higher infiltration pressure decreased dissolution rate significantly.

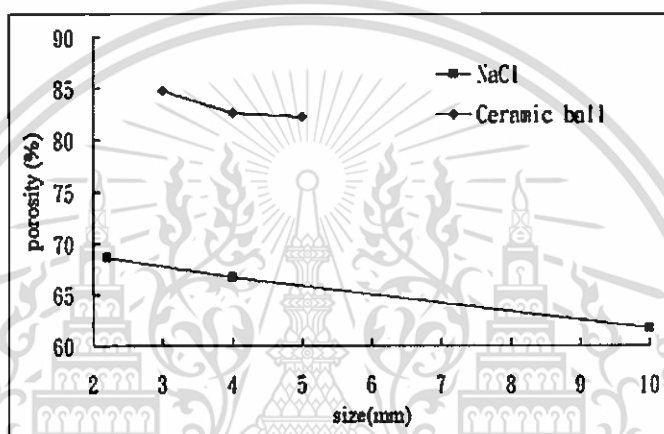


Figure 2.15 Effect of space holder size on porosity of Al foams [28].

2.4.2 Investment Casting Method (Duocel® aluminium foam)

The key of this method is to fill molten metal instead of mold pattern in a mold. Mold pattern produced from polymer material in arbitrary shape and size is coated with casting slurry, such as sand, and placed in a casting mold. Heat was used to decompose the polymer, dry the casting slurry and enhance casting slurry strength. Pressure is then applied for assisting molten metal to fill into the mold as shown in **Figure 2.16** [19]. This technique is expensive in preparing mold pattern and slurry casting mold.

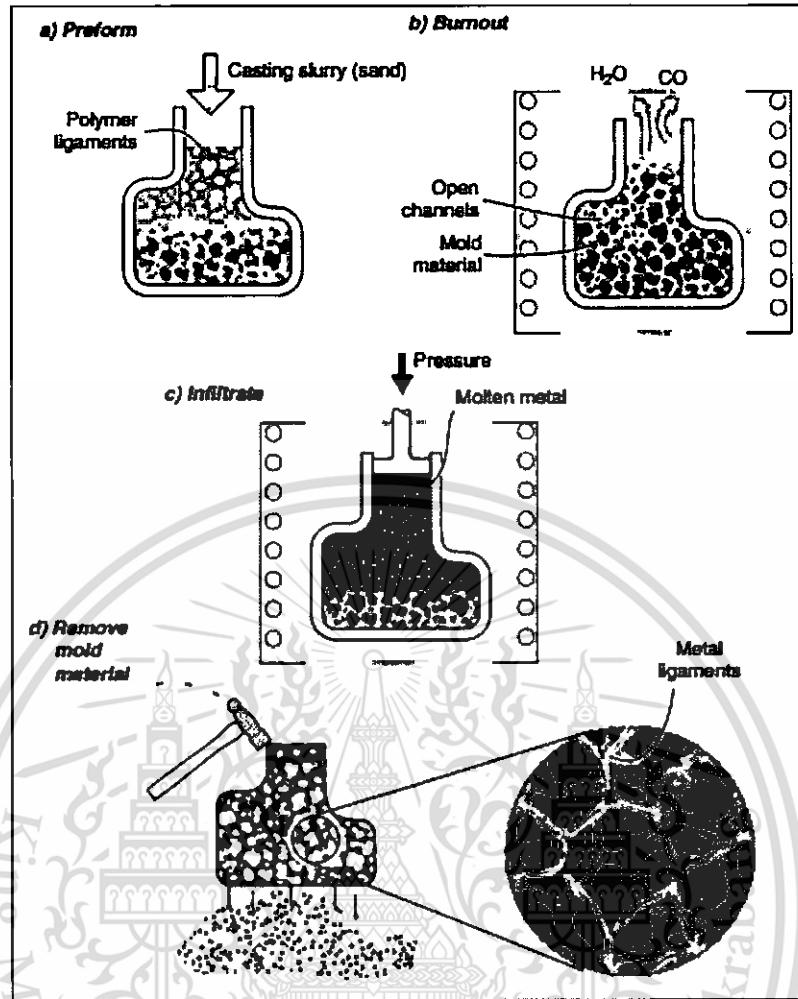


Figure 2.16 Schematic diagram of investment casting method for open cell aluminium foam production such as Duocel® aluminium foam) [19].

2.4.3 Honeycomb Casting Process (Alvéotec)

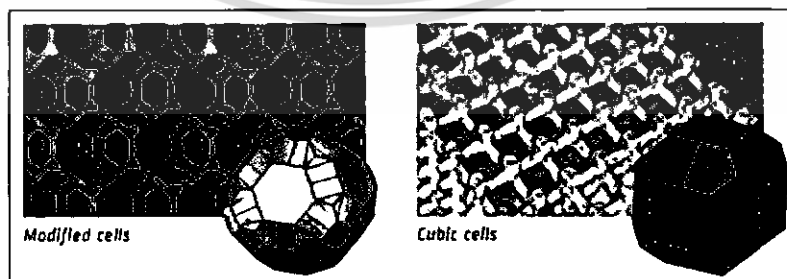


Figure 2.17 Photographs of cell structures: modified and cubic cells [29].

Figure 2.17 shows a unique aluminium foam with cell diameter of 10 mm made from pure Al of 99.7% by Alvéotec company. This foam structure was claimed to have an

excellent thermal behaviour which can be used as a heat sink to improve heat dissipation up to 40%. Production method of this aluminium foam is shown in Figure 2.18 [29].

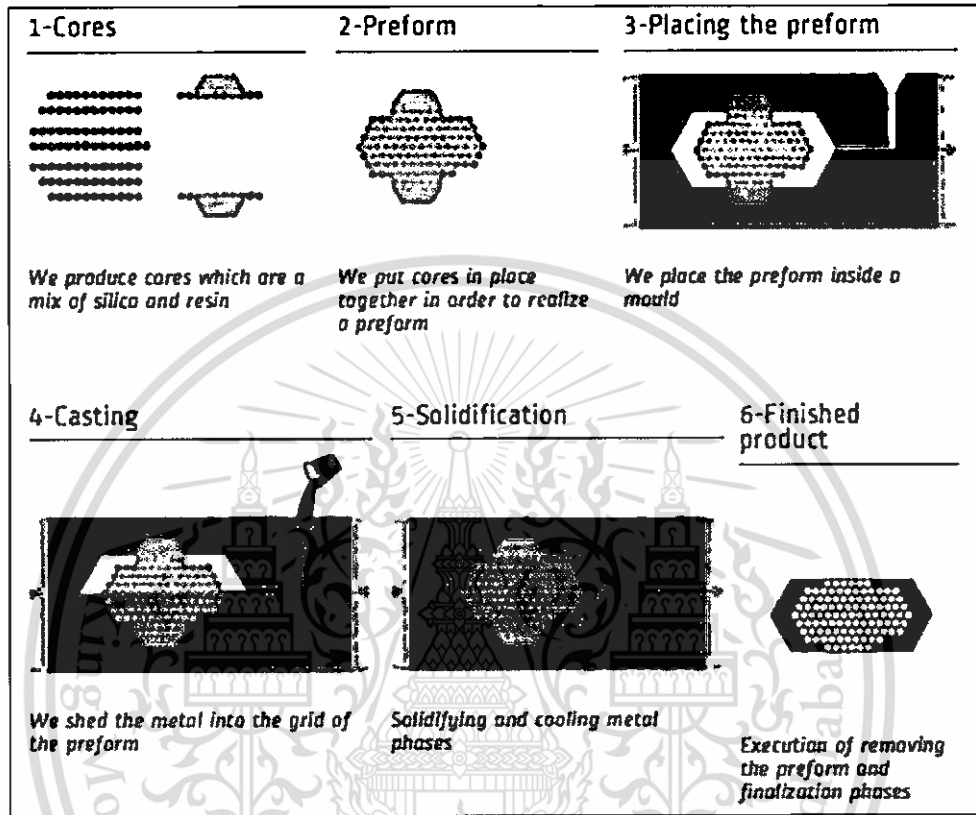


Figure 2.18 Schematic diagram of direct casting method for open cell aluminium foam production (Alvéotec process) [29].

2.4.4 Styropor Granules Sintering Method (Globomet®)

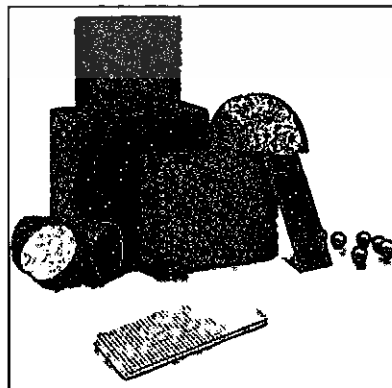


Figure 2.19 Photographs of aluminium foams produced from hollow spheres [30]. This material is reserved for educational use only, not allowed for commercial use.

Figure 2.19 shows novel aluminium foams produced from hollow spheres which are made from polymer balls coated with metal and ceramic powder as shown in **Figure 2.20** [30]. The foams produced by this method is very thin and uniform cell wall thickness. These aluminium foams are suitable for energy absorption application.

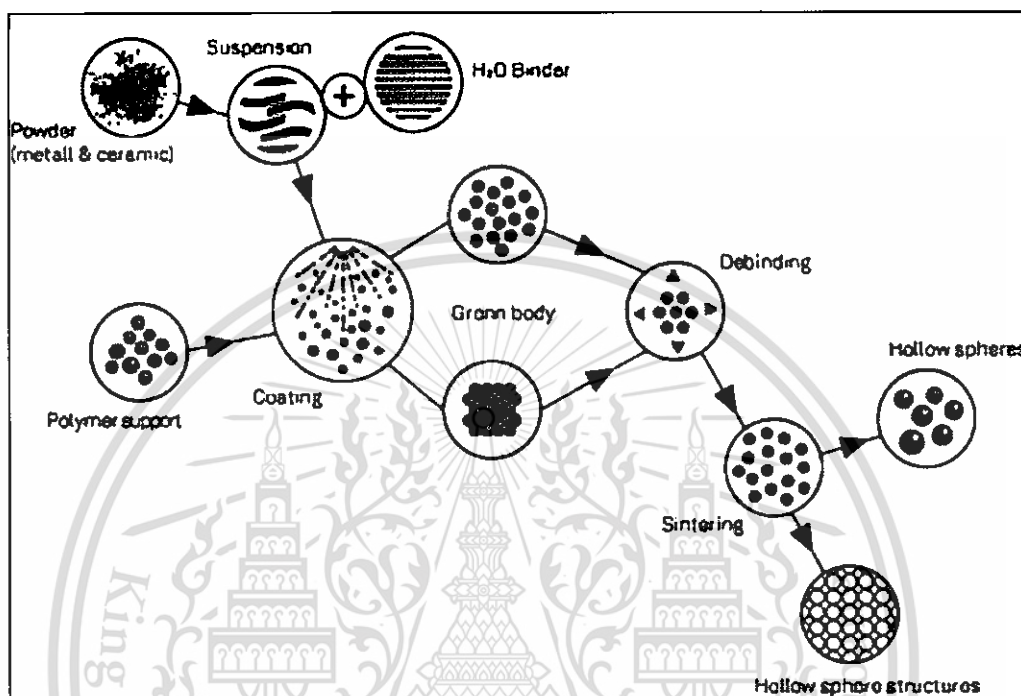


Figure 2.20 Schematic diagram of (globomet® process) [30].

2.4.5 Replica method

In this method, an open cell foam is produced using sponge or PU foam, as a mold pattern. The mold pattern having specific cell sizes and shapes is coated with metal powder slurry and dried. Mold pattern together with metal powder slurry is heated to decompose polymer material. The structure of the obtained foam is a duplication of mold pattern structure as shown in **Figure 2.21** [31]. Optimal properties of metal powder slurry for coating or impregnation are still practical limitation. The foam produced by this method contains strut cells having hollow in their center as shown in **Figure 2.22** [32].

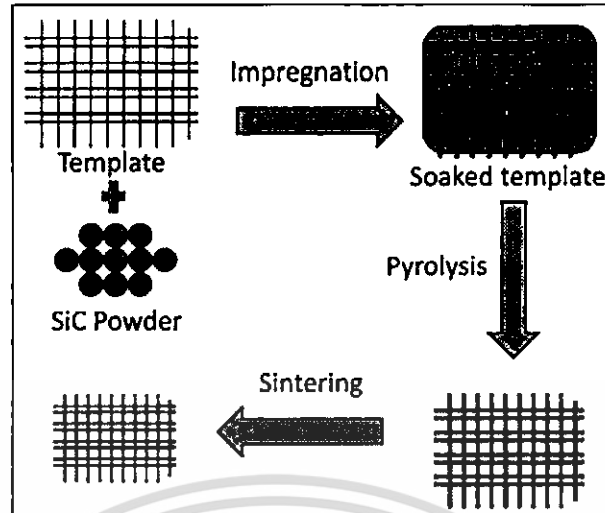


Figure 2.21 Schematic diagram of replica method for open cell aluminium foam production [31].

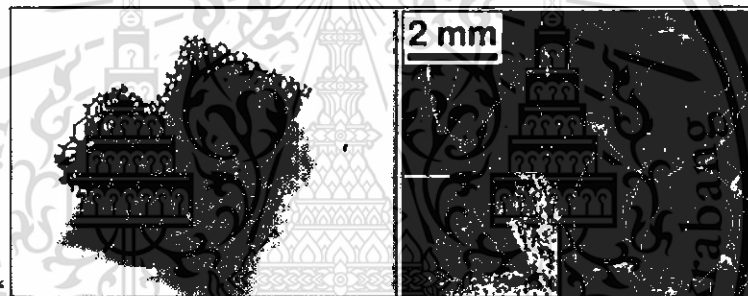


Figure 2.22 Photographs of stainless steel foams with ligament of cell structures having hollow inside [32].

2.5 Production Parameters Influencing on Foam Structure

2.5.1 Degree of Drainage

The degree of drainage is the level of the fluid that can permeate through a mold during applying forces to the fluid by either applied pressure or vacuum. Permeability of fluid flow has been studied for filter and pneumatic silencer applications [33] and for describing thermo physical properties of aluminium foams [34]. However, permeability of mold drainage has never been determined in producing aluminium foams using the space holder method. Level of fluid permeability depends on medium characteristics as can be described by Darcy's law. Degree of drainage of mold is one of important parameters influencing on aluminium foam production by vacuum infiltration method because the structure of a produced foam is directly related to its level.

Permeability of a fluid flowing through a mold is characterised based on the type of fluid flow which is described by the Reynolds's number [35], [36]. When the fluid flow

This material is reserved for educational use only, not allowed for commercial use.

Forbidden to modify the content, and cite the document when use.

is laminar in which the Reynolds's number is in the ranges 1 – 10, permeability of the flowing fluid can be determined by Darcy's law as given in equation (2.2) [37]. For higher Reynolds's numbers, the fluid flow is turbulent, and hence the permeability cannot be determined by the linear Darcy's equation. The turbulent flow can be, instead, determined by Forcheimer's equation as given in equation (2.3) [37].

The permeability coefficient of porous materials can be determined by Darcy's equation [37].

$$K = \frac{\mu QL}{A(\Delta P)} \quad (2.2)$$

where K is the permeability, μ is the viscosity of the fluid in centipoises, Q is the volumetric flow rate measured in cm^3/sec , L is the length of specimen in cm in the flow direction, A is the cross-sectional area of the specimen perpendicular to the direction of gas flow in cm^2 , ΔP is the pressure drop over the specimen length ($P_2 - P_1$): P_2 and P_1 are the pressure at outside and inside of the specimen in atmospheres, respectively.

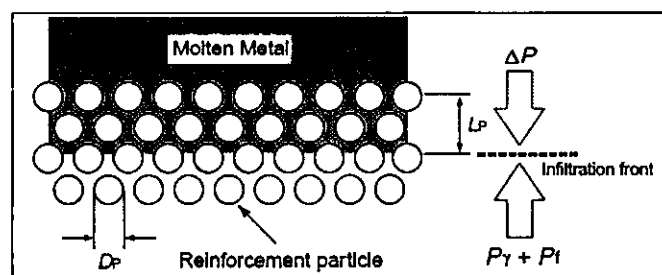
The permeability coefficient of porous materials with non-linear fluid flow can be determined by Forcheimer's equation [37].

$$-\frac{\Delta P}{L} = \frac{\mu}{K}V + \beta\rho V^2 \quad (2.3)$$

where V is the fluid velocity averaged over the total cross-section of the porous specimen (Q/A), β is the inertial parameter, ρ is the density of the fluid. Density of air and viscosity can be taken from physical properties tables of gases at atmospheric pressure [38].

2.5.2 Infiltration Pressure

In production of an aluminium foam using space holders, a different pressure, ΔP , is applied across the space holders to assist molten metal to infiltrate through spaces within the space holders. During infiltration, capillary pressure (P_c) and pressure drop (P_f) give an opposite direction to the infiltration as illustrated in Figure 2.23 [39]. A space holder with different particle size contains different capillary pressure and pressure drop, and hence requires different infiltration pressure as shown, for example, in Figure 2.24.



This material is reserved for educational use only, not allowed for commercial use.

Forbidden to modify the content, and cite the document when use.

Figure 2.23 Pressure balance at the advancing melt front in the pressure infiltration process [39].

Relations between an applied pressure and parameters which are determinative to structure and hence mechanical properties of foams have been extensively proposed as summarised in **Table 2.3**. Several parameters can be experimental measured to describe infiltration behavior. One of the measurable parameters called saturation is the extent of filling of a molten metal into a space holder, S , which is the fraction of open pore space filled by the molten metal [24]. Another measurable parameter is an infiltration height which is the distance of infiltration. It can be estimated using the Young - Laplace equation [40] given in Equation (2.5). Saturation of molten metal in spaces of a space holder can be determined using a soil science model based on liquid infiltration into a porous media [41] and [42]. Infiltration height can be directly derived from Darcy and capillary laws [22]. **Table 2.4** shows various aluminium foams produced using the space holder method.

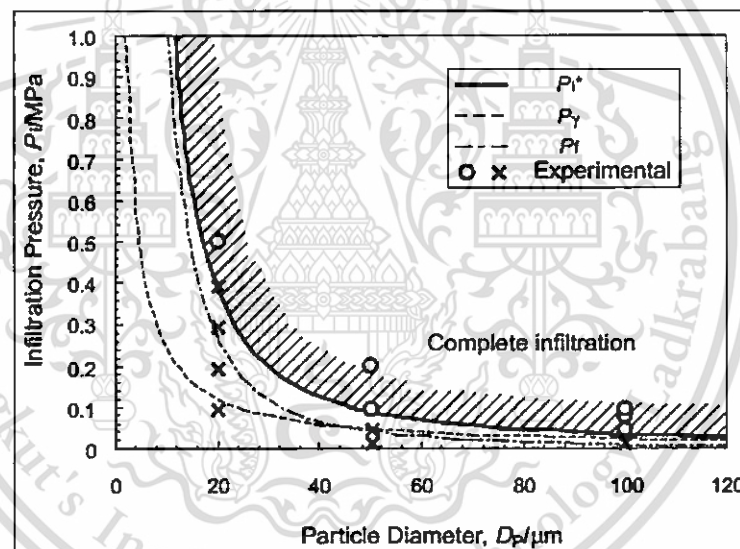


Figure 2.24 Dependence of critical pressure required for infiltration into space of different size of SiC space holder [39].

Influence of infiltration pressure on foam structure can be classified as infiltration cases similar to those in squeeze casting [43] as given below.

- No infiltration
- Partial infiltration (some space holders are incompletely infiltrated)
- Full infiltration with residue
- Full infiltration with infiltrate

Different infiltration cases take place depending on the extent of applied infiltration pressure and other production parameters. Inappropriate applied pressure can result in

defects in foam structure such as metal finger occurred due to too high applied pressure [24].

Table 2.3 Models relating to production and structure parameters of foams produced using infiltration method.

Model	Description	Eqs.
Young - Laplace	$P_{th} = (2\sigma_{LV} \cos \theta)/r_h$	(2.4)
equation [23], [40].	$L^2 = (\rho r_e^2 / 4\eta)[(2\sigma_{LV} \cos \theta)/(\rho r_e) - gL + P_{app}/\rho]t$	(2.5)
The infiltration	$V = Avdt \times K \times S_m$	(2.6)
model of molten	$Q_1 = V\rho_{Al}H_{Al} = \rho_{Al}H_{Al}KS_mAvdt$	(2.7)
metal and the	$= (1 - K)\rho_{salt}C_{salt}(T_E - t_0)Avdt$	(2.8)
distribution of	$Q_2 = \lambda_{Al}A(T_0 - T_E)dt/\Delta L$	(2.8)
temperature [44].	$\Delta L = \lambda(T_0 - T_E)/[(1 - K)\rho_{salt}C_{salt}(T_E - t_0)v]$	(2.9)
	$t = \frac{\rho_{Al}V_{Al}C_{Al}(T_b - T_a)}{\lambda_{salt}A(T_b - T_L)}L$	(2.10)
	$Re_c = \frac{ud}{v}$	(2.11)
	$v = \frac{\beta K^2}{\lambda(1 - K)}d^2 \frac{\gamma_{Al}}{\eta_{Al}}J$	(2.12)
	$F = \frac{(1 - k)dAds}{\beta d^3} \lambda \eta dv$	(2.13)
Saturation (extent of filling) [23]	$S = \frac{V_m}{1 - V_r} = 1 - \left(\frac{P_b}{P}\right)^\lambda$	(2.14)
	$V_m = \frac{V_{m'}}{V_f}$	(2.15)
	$V_{m'} = \frac{m_f}{\rho_{AC2A}}$	(2.16)
	$V_r = \frac{m_p}{V_p}/\rho_{preform}$	(2.17)
	$P_b = \frac{2\sigma_{LV} \cos \theta}{r_e}$	(2.18)
	$S = \frac{m_f}{\rho_{AC2A} V_f} / 1 - \left(\frac{m_p}{V_p}/\rho_{preform}\right)$	(2.19)
	$\varphi = \frac{\sigma_{LV}^{Al} \cos(\theta_{Al-pre})}{\sigma_{LV}^{Hg} \cos(\theta_{Hg-pre})}$	(2.20)
	$S = 1 - \left(\frac{P_b}{P}\right)^\lambda$	(2.21)
	$\ln(1 - S) = \ln\left(\frac{P_b}{P}\right)^\lambda$	(2.22)

This material is reserved for educational use only, not allowed for commercial use.

Forbidden to modify the content, and cite the document when use.

$$\ln(1 - S) = \lambda \ln\left(\frac{P_b}{P}\right) \quad (2.23)$$

$$\ln(1 - S) = \lambda[\ln P_b - \ln P] \quad (2.24)$$

$$\text{Minimum pore radius [33]} \quad r_{min} = \frac{-3\sigma + \sqrt{9\sigma^2 - 8\sigma RP \cos \theta}}{2P} \quad (2.25)$$

Table 2.4 Aluminium foams produced using space holder method.

Materials	Process	Space holder	Density (g/cm ³)	Pore size (mm)	Applied pressure (MPa)	Pouring temperature (°C)	Preheat temperature (°C)
Alloys (A356)	Counter-gravity infiltration	Sulfate	n/a	n/a	0.02	800	400 [45]
Alloys (ZL104)	Infiltration pressure	Granule	n/a	8 - 14 (mesh)	0.02 - 0.08	670 - 760	30 - 240 [46]
Alloys (ZL102)	Infiltration pressure	Salt	n/a	0.4 - 0.6	0.04	740 - 760	450 - 500 [44]
Alloys (ZL102)	Infiltration pressure	NaCl	n/a	0.6 - 3.2	0.04 - 0.07	700 - 760	450 - 500 [47]
Pure Al	Infiltration pressure	Salt	0.26 - 0.80	1.4 - 2.0	0.1 - 0.2	760	600 [23]
Pure Al	Infiltration pressure	NaCl	0.15 - 0.89	0.5 - 3.1	0.1 - 0.25	760	600 [48]
Pure Al	Infiltration pressure	NaCl	n/a	1.3 - 1.9	0.1 - 0.3	n/a	n/a [49]
Pure Al	Infiltration pressure	NaCl	15 - 25%	0.4	0.2 - 15.5	n/a	n/a [24]
Alloys (Al)	Infiltration pressure	NaCl	0.85 - 1.08	0.3 - 1.6	0.2	720	700 [50]
Pure Al	Infiltration pressure	NaCl	n/a	0.4	0.4	710	775 [25]
Alloys (A356)	Replication	Salt	1.05	3	2.0 - 3.0	700	500 [51]
Alloys (AlSiMg)	Infiltration pressure	NaCl	34 - 36%	0.5 - 2.0	n/a	700	n/a [52]
Alloys (Al)	Infiltration pressure	Ceramic balls	82 - 88%*	3.0 - 5.0	n/a	740	n/a [28]

(% is relative density and *% is porosity)

2.5.3 Infiltration Temperature

Infiltration temperature which includes the temperature of molten metal, mold and space holder is one of parameters determining foam structure. Fischer *et al.* [53] investigated the influence of casting (molten metal) and mold temperature on compressive behavior of open pore 10 and 15 ppi foams produced using A356 alloy. They found that increasing the mold temperature from 700°C to 750°C and reducing

the casting temperature decreased mechanical properties. Increasing pouring temperature and infiltration time were found to enhance infiltration rate of molten metal which increased struts diameter after solidification [53], [54].

Chung *et al.* [55] indicated that infiltration temperature of 640 °C was an optimum condition for producing SiCp/Al composites. Wu *et al.* [44] studied influence of infiltration factors: preheat temperature (A), pouring temperature (B), infiltration pressure (C), and content of ceramic balls (D), on infiltration height in producing aluminium foam composite using an orthogonal test. They found that the influential degree is $A > C > B > D$. The optimum producing parameters in this study are preheat temperature of 480°C, pouring temperature of 740 °C, infiltration pressure of -0.04 MPa and content of ceramic ball of 20 - 40%. Schematic describing infiltration of Wu *et al.*'s work [44] is shown in Figure 2.25 which includes temperature distribution of metal. Due to heat exchange between molten metal having initial temperature (T_0) and space holder having initial temperature (t_0), the molten metal loses heat during infiltration along the distance (ΔL) leading to complete solidification at temperature (T_E). The infiltration length can be derived from the balance of energy loss of molten metal and energy gain of space holder as given in Equations (2.6) - (2.10) in Table 2.3.

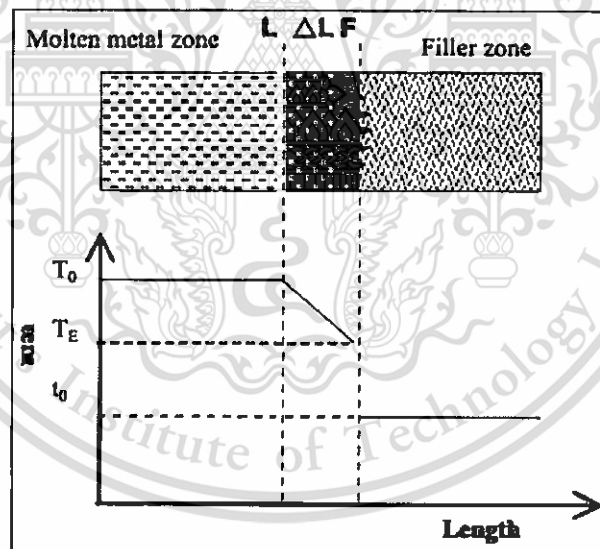


Figure 2.25 Schematic of molten metal temperature during advancing into a filler (space holder) in infiltration process [44].

2.6 Mechanical Properties of Open Cell Aluminium Foam

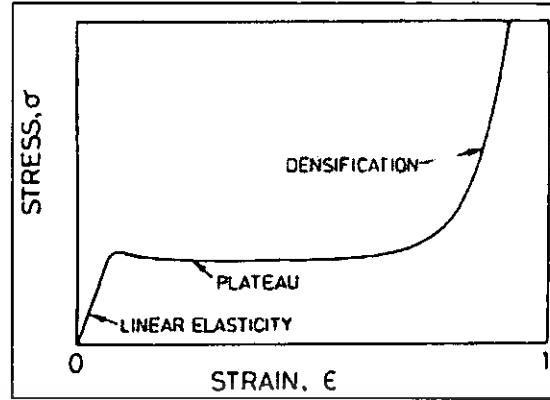


Figure 2.26 Typical compressive stress-strain response of cellular metal [56].

Energy absorption is one of dominant mechanical properties of open cell aluminium foams having an interconnectivity between pore and stiffness. Such structure well absorbs energy by deformation. The deformation behavior of an open cell aluminium foam can be divided into three stages: linear elasticity, plateau and densification, as shown in **Figure 2.26** [56]. In stage I, aluminium foam can return to its original shape after being deformed, while in stage II, the elastic limit is beyond and shape of aluminium foam change permanently. During state II, cell wall of aluminium foam buckles resulting in constant stress called plateau stress (σ_{pl}). Stage III occurs when the cell wall collapses leading to densification and increase in stress. Young's modulus (E) of aluminium foam can be determined by fitting the slope of stress-strain curve of elastic regime with a straight line. The plateau stress (σ_{pl}) starts at the end of elastic regime in which struts are initial collapse until complete collapse at densification strain (ϵ_d). Densification strain can be determined by intersection of straight lines between two curves at the end of plateau regime [57]. Energy absorption capacity can be determined by summing the area under stress-strain curve as shown below.

$$w = \int_{\epsilon}^{\epsilon_d} \sigma(\epsilon) d\epsilon \quad (2.26)$$

Energy absorption performance of open cell aluminium foams are not only dependent on pore size but also strut thickness (t_{st}), strut length (l_{st}), ρ^*/ρ_s , strut morphology [58], relative density (ρ^*/ρ_s) and cell alignment [59]. Homogenous or heterogeneous foam structure can be determined by the stress-strain curve of compressive test. **Figure 2.27** shows results of compressive test of commercial open cell aluminium foams [60].

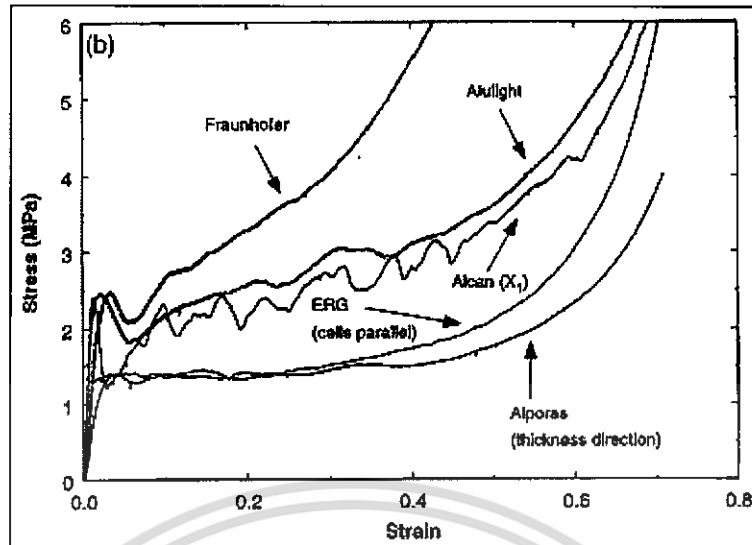


Figure 2.27 Compressive stress-strain curves of commercial open cell aluminium foams [60].

2.7 Acoustical Property of Open Cell Aluminium Foam

2.7.1 Sound Absorption performance

Sound absorption performance of absorbent materials can be measured in terms of noise absorption coefficient (NAC) or noise reduction coefficient (NRC) which represents the amount of sound energy absorbed upon striking a particular surface. NAC is generally measured at one-third octave band center frequencies ranging from 100 to 5000 Hz of normal incidence sound using an impedance tube following ASTM standards. NRC is the average, rounded to the nearest multiple of 0.05, of the absorption coefficients, commonly determined in reverberation rooms of qualified acoustical laboratory test facilities, at the one octave band center frequencies of 250, 500, 1000 and 2000 Hz [14]. NAC or NRC of 0 indicates perfect reflection, while 1 indicates perfect absorption. Physical phenomenon such as viscous losses, thermoelastic damping, Helmholtz-type resonators, vortex shedding from sharp edges, and direct mechanical damping [61] are important factors in determining the absorption behaviour of absorbent materials. In open cell aluminium foams, the main contributions to sound absorption performance are viscous losses and thermoelastic damping.

Previous studies in sound absorption performance of open cell aluminium foams have concentrated on two main areas: structural parameters, such as porosity, pore size, aperture size, sample thickness and static flow resistivity, and installation techniques.

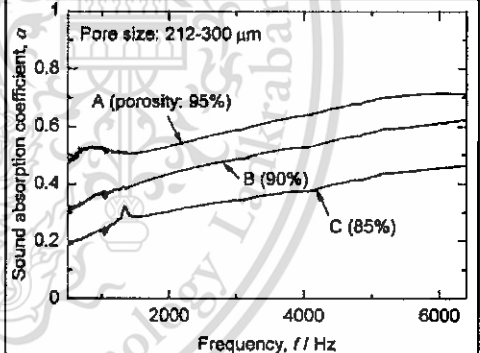
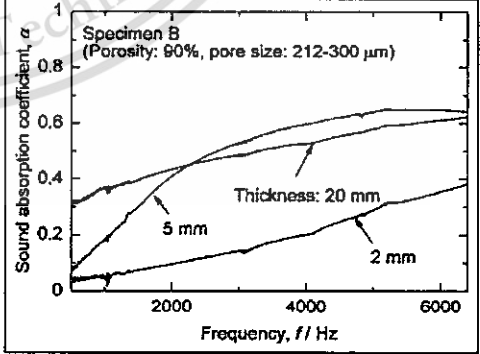
- Structural parameters influencing sound absorption performance

Hakamada *et al.* [16] investigated effects of structural parameters of open cell aluminium foams, produced by spacer method, with porosities (85% - 95%), pore sizes (0.2 – 0.6 mm), aperture sizes (0.26 – 0.67 mm) and sample thickness (2, 5 and 20 mm).

This material is reserved for educational use only, not allowed for commercial use.

Forbidden to modify the content, and cite the document when use.

They found that sound absorption coefficient increased with increasing porosity, aperture size and sample thickness, while pore sizes gave no significant effect to sound absorption coefficient. In addition, measured sound absorption results were in good agreement with predictions based model given by Lu *et al.* [59]. Li *et al.* [49] studied effect of aperture number and size of aluminium foams having a constant porosity of 65% on sound absorption coefficient. They reported that increasing a number of apertures per unit area or reducing aperture size in the range of 0.4 to 0.3 mm enhances sound absorption coefficient. Moreover, aluminium foams with varying pore in the range of 1.3 – 1.9 mm and without varying porosity and aperture size were found to exhibit similar sound absorption behavior, especially at low frequencies. Guan *et al.* [62] investigated sound absorption performance of aluminium foams with bulk density of 0.85 – 1.08 g/cm³, porosity of 60% - 68%, pore size of 0.4 – 0.1 mm and static flow resistivity of 28 – 147 kPa·s/m². They reported that there are poor and no significant relation of structural parameters to sound absorption at frequencies in the range of 0 – 500 Hz. At frequencies higher than 1,000 Hz, static flow resistivity and bulk density increased in proportion to sound absorption coefficient. Details of sound absorption results of the described literatures are given in **Figure 2.28**.

Literature	Structural parameters	Sound absorption performance
Hakamada <i>et al.</i> [16]	Variable porosity: 85%, 90% and 95% Constant pore size: 0.2 – 0.3 mm. Constant thickness: 20 mm.	
	Variable thickness: 2, 5 and 20 mm. Constant porosity: 90% Constant pore size: 0.2 – 0.3 mm.	

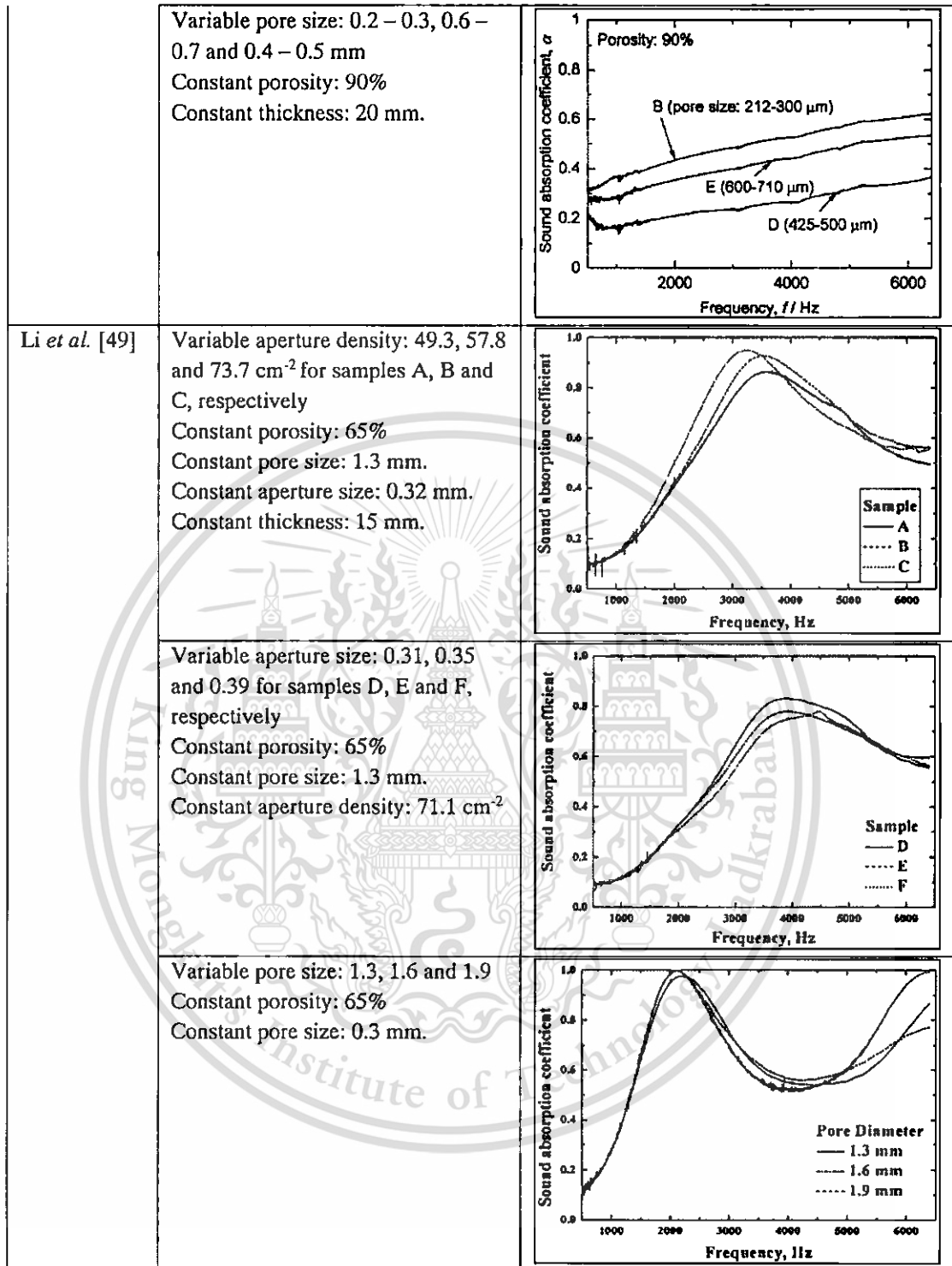


Figure 2.28 Sound absorption results of open cell aluminium foams.

- Installation techniques influencing sound absorption performance

Many studies have investigated effects of installation of absorbent materials on sound absorption performance. Various installation techniques have been found to improve the performance of absorbent materials. Installation with an air cavity between

This material is reserved for educational use only, not allowed for commercial use.

Forbidden to modify the content, and cite the document when use.

absorbent material and rigid wall, for example, can shift resonance frequencies peak backward to lower frequencies which can be described by Helmholtz resonator's equation [16], [49]. Structural configuration of absorbent materials can be controlled using different installations to receive optimal sound absorption coefficients at specific frequency [63]. Band width of sound absorption coefficient can also be modified and expanded by installation of absorbent materials in different order [64], [65].

- Models for prediction of sound absorption coefficient

A wide range of methods, including power-law relation, equivalent electrical circuit, acoustic-transmission and equivalent fluid, are currently employed in modelling sound absorption behaviour of open cell aluminium foams as shown in Table 2.5. Prediction models of sound absorption coefficient indicated that essential parameters influencing on sound absorption performance of open cell aluminium foams are aperture size and air gap in tests using an incident sound wave direction [16], [49]. Previous experimental results of sound absorption coefficient of open cell aluminium foam showed good agreement of those with prediction in that aperture size is more predominant than pore size for good sound absorption performance [50]. Likewise, thickness was found to be more pronounced than porosity in sound absorption of open cell aluminium foam [66], [67]. However, good sound absorption performance can be optimised using prediction models to select optimal structural parameters such as pore size, aperture size and pore connectivity [59].

Table 2.5 Prediction models for sound absorption coefficient of porous materials.

Model	Author	Description	Eqs.
Power-law relation	Delany and Bazley [68]	$Z = Z_0 \coth \gamma l$	(2.27)
		$\alpha_n = 1 - \left \frac{Z - \rho_0 c_0}{Z + \rho_0 c_0} \right ^2$	(2.28)
Equivalent electrical circuit approach (EECA)	Congyun and Qibai [69]	$Z_D = -i\rho_0 c_0 \cot(0.909D\omega/c_0)$	(2.29)
		$R_0 = \frac{32\eta t}{d^2} (\sqrt{1 + \beta^2/32} + \sqrt{\beta d/4t})$	(2.30)
		$M_0 = \omega\rho_0 t(1 + 1/\sqrt{9 + \beta^2/2} + 0.85 d/t)$	(2.31)
		$Z_1 = z_0 + Z_D = R_1 + iM_1$	(2.32)
		$Z_n = z_0 + \frac{1}{(1/Z_D) + (1/Z_{n-1})} = R_n + iM_n$	(2.33)
		$\alpha = \frac{4R_n/\rho_0 c_0}{(1 + R_n/\rho_0 c_0)^2 + (M_n/\rho_0 c_0)^2}$	(2.34)
Acoustic-Transmission Approach (ATA)	Lee and Chen [70]	$\Gamma_{j1} = Z_{j1} \frac{Z_r \cosh(\gamma_{j1} t_{j1}) + Z_{j1} \sinh(\gamma_{j1} t_{j1})}{Z_r \sinh(\gamma_{j1} t_{j1}) + Z_{j1} \cosh(\gamma_{j1} t_{j1})}$	(2.35)
		where ($j = a$ or m)	(2.36)
		$a = \text{air and } m = \text{porous material}$	(2.37)
		$\alpha = \frac{4R_r/\rho_a c_a}{(R_r/\rho_a c_a + 1)^2 + (X_r/\rho_a c_a)^2}$	(2.38)
		where R_r and X_r are real and imaginary	(2.39)

This material is reserved for educational and non-commercial use.

Forbidden to modify the content, and cite the document when use.

		of resultant acoustic impedance Γ_r	(2.40)
Equivalent fluid	Johnson-Allard [71]	$Z = \sqrt{\rho K}$, $k = \omega \sqrt{\rho/K}$	(2.41)
		$\rho(\omega) = \rho_0 \left[1 + 1 / \sqrt{3^2 + \frac{4\omega\rho_0}{\sigma\phi} - i \frac{\sigma\phi}{\omega\rho_0} \sqrt{1 + \frac{\omega\rho_0}{4\sigma\phi}} \right]$	(2.42)
		$K(\omega) = \gamma P_0 / \left[\gamma - (\gamma - 1) \left(1 - \frac{Nu}{i8\omega\rho_0 P_r / \sigma\phi + Nu} \right) \right]$	(2.43)
		$\begin{bmatrix} P_f \\ V_f \end{bmatrix} = [T] \begin{bmatrix} P_b \\ V_b \end{bmatrix} = \begin{bmatrix} T_{11} & T_{12} \\ T_{21} & T_{22} \end{bmatrix} \begin{bmatrix} P_b \\ V_b \end{bmatrix}$	(2.44)
		$\begin{bmatrix} T_{11} & T_{12} \\ T_{21} & T_{22} \end{bmatrix} = \begin{bmatrix} \cos kd & iZ \sin kd \\ i \sin kd / Z & \cos kd \end{bmatrix}$	(2.45)
		$[T']_{total} = [T_1][T_2][T_3] \dots [T_n] = \begin{bmatrix} T'_{11} & T'_{12} \\ T'_{21} & T'_{22} \end{bmatrix}$	(2.46)
		$\alpha = 1 - \frac{ T'_{11} - T'_{21} Z_0 ^2}{ T'_{11} + T'_{21} Z_0 ^2}$	(2.47)
		$[T_n]_{foam} = \begin{bmatrix} \cos kd_n & iZ \sin kd_n \\ i \sin kd_n / Z & \cos kd_n \end{bmatrix}$	(2.48)
		$[T_n]_{air} = \begin{bmatrix} \cos k_0 D_n & iZ \sin k_0 D_n \\ i \sin k_0 D_n / Z & \cos k_0 D_n \end{bmatrix}$	(2.49)

In conclusion, parameters significantly influencing on enhancing sound absorption performance are material structure and installation techniques. For open cell aluminium foams produced by space holder method, structure with small pore size under 1 mm, porosity in the range of 60 - 95% and foam thicknesses 2 - 20 mm performed low sound absorption at low frequencies, 125 to 1,000 Hz, at which the maximum sound absorption coefficient is 0.5. Sound absorption coefficients at frequencies higher than 1,000 Hz rapidly increased until reaching a peak and then declined at higher frequencies as shown for example in Figure 2.28. Relation between pore size and sound absorption coefficient has been extensively studied. However, no significant correlation has been reported due to a narrow investigated pore size. Wang *et al.* [72] suggested that pore size of 0.1 mm in diameter exhibits a good sound absorption and Li *et al.* [49] reported that the open cell aluminium foam with aperture size of 0.034 mm performed better sound absorption than that with aperture size of 0.088 mm. For pore size with diameter below 0.1 mm, sound absorption performance became poor and hence most incident noises reflected back to the sound source. In practical operation, high noises at any frequencies should be reduced using a suitable absorbent material. Sound absorption performance of open cell aluminium foams produced using space holders with small pore sizes in the range 0.1 to 4 mm have been investigated so far due to limitation in production of space holder.

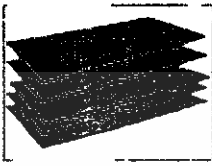


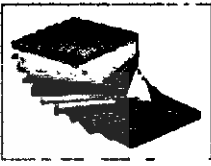
Table 2.6 shows properties of open cell aluminium foams comparing with other absorbent materials. Advantages of aluminium foams are heat resistance, energy absorption, water proof and anti-bacteria, but cost and weight are disadvantages of aluminium foams. Despite fibrous materials are low price, low density, good flexibility

This material is reserved for educational use only, not allowed for commercial use.

Forbidden to modify the content, and cite the document when use.

and acceptable strength [73], [74] and [75], they suffer dust intake and non-recyclable production waste giving a burden on health and environment.

Table 2.6 Comparative properties of sound absorbant materials [76].

Type	Aluminum Foam	Polyester	Glass Fiber	Urethane Form
Shape				
Material	Aluminum	Polyester	SiO ₂ , mineral	high molecular Material
Acoustic absorption(NRC Standard)	over 0.70	over 0.70	over 0.75	over 0.65
Acoustic absorption term	Permanent	Quality deterioration	sudden quality Deterioration	Quality deterioration
Eco-friendly	100% recyclable Environmental friendly	No recyclable easy Incineration low corpuscule	No recyclable, hard Incineration arsenic acid cause	No recyclable easy Incineration
Materials handling & Constructability	Easy conveyance, handling and works	Easy conveyance, handling and works	Easy transmission by contagion, Respiratory Disease and skin ailments	Easy conveyance, handling and works
Human maleficence	harmlessness	harmlessness	harmfulness	poisonous gas (CO, Cyan gas) on fire
Drainage & absorptiveness	Waterproofness, stable form, Permanent acoustic absorption	Waterproofness, stable form, Semi-permanent acoustic absorption	No waterproofness unstable form, lowering acoustic absorption	No waterproofness stable form, lowering acoustic absorption
Nonflammability	Inflammable (heat-resistant) -under 780°C-	Flammable	heat-resistant -under 350°C-	bad heat resistant (heat-resistant) -under 100°C-

2.7.2 Acoustical measurement

- Determination of sound absorption coefficient

There are two main methods for sound absorption coefficient measurement: reverberation room [77] and impedance tube method [78] both giving sound absorption coefficient as a function of frequency. The former is suitable for large materials, the latter, on the other hand, is suitable for small materials with limited workspace. The impedance tube method has been widely used in research work and small scale products. There are two types of measurement for the impedance tube method: standing wave ratio and transfer function method. Due to more usage, this work will describe only the transfer function method.

In transfer function method, complex frequency response between two microphones is measured as given by Equations (2.50) – (2.55).

$$H_{12} = \frac{p_2}{p_1} = \frac{e^{jk_0x_2} + re^{-ik_0x_2}}{e^{jk_0x_2} + re^{-ik_0x_1}} \quad (2.50)$$

where p_1 and p_2 are complex sound pressure measured by two microphones locating at positions x_1 and x_2 ($x = 0$ measured at the center of microphone which is close to the specimen to front of specimen). The wave number, k_0 is defined by equation:

$$k_0 = \frac{2\pi f}{c_0} \quad (2.51)$$

where c_0 is the speed of sound (m/s) and f is frequency (Hz). The transfer function of incident wave alone, H_i and the reflection wave alone, H_r are determined as the following equation:

$$H_i = e^{-ik_0(x_1-x_2)} \quad (2.52)$$

$$H_R = e^{ik_0(x_1-x_2)} \quad (2.53)$$

Combining equations (2.50), (2.52) and (2.53) the normal incidence reflection factor, r is determined by equation:

$$r = \frac{H_{12} - H_i}{H_R - H_{12}} e^{2jk_0x_1} \quad (2.54)$$

The sound absorption coefficient, α is determined by:

$$\alpha = 1 - |r|^2 = 1 - r_r^2 - r_i^2 \quad (2.55)$$

where r_r and r_i are the real and imaginary components of r , respectively.

- Designation of impedance tube with two-microphone method

An impedance tube is made from a straight cylindrical pipe with smooth surface. Thickness of the tube is recommended to be 5 – 10% of inside tube diameter. A test specimen is mounted in sample holder at one end of the tube. Plane wave is generated by a loud speaker with frequency band 1/3 octave in according to tube specifications. The design of impedance tube for sound absorption test depends on operational parameters suggested in ASTM Standard E1050-98 [78]. The working frequency range is determined by equation:

$$f_l < f < f_u \quad (2.56)$$

where f is the working frequency (Hz), f_l is the lower working frequency of the tube (Hz) and f_u is the upper working frequency of the tube (Hz).

The tube diameter range is determined by equation:

$$d < K * c / f_u \quad (2.57)$$

where d is the diameter of the tube (m), K is a constant which is 0.586 and c is the speed of sound in the tube (m/s) f_u .

The microphone spacing is given by equation:

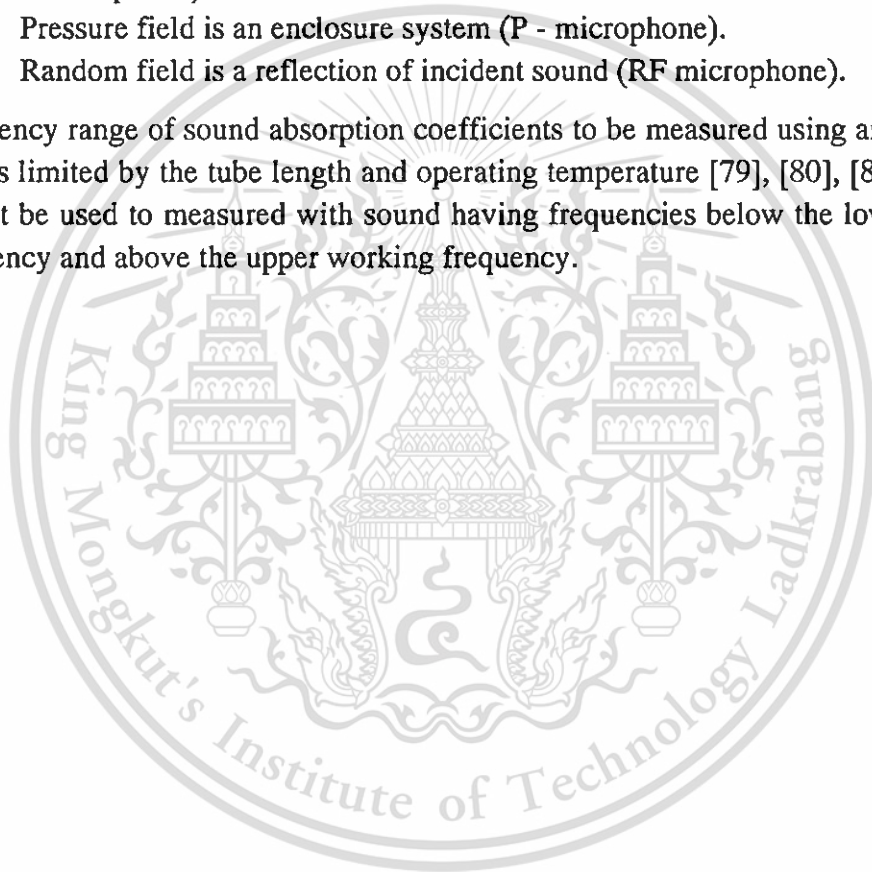
$$S \ll c/2f_u \quad (2.58)$$

where S is the distance between microphones (m).

There are three different microphone types classified by type of sound field available in the market.

1. Free field is an open area where there is no reflection of any incident sound (FF - microphone).
2. Pressure field is an enclosure system (P - microphone).
3. Random field is a reflection of incident sound (RF microphone).

Frequency range of sound absorption coefficients to be measured using an impedance tube is limited by the tube length and operating temperature [79], [80], [81]. The tube cannot be used to measured with sound having frequencies below the lower working frequency and above the upper working frequency.



CHAPTER 3 EXPERIMENTAL PROCEDURE

3.1 Aluminium Foam Production

3.1.1 Space Holder with Vacuum Infiltration Method

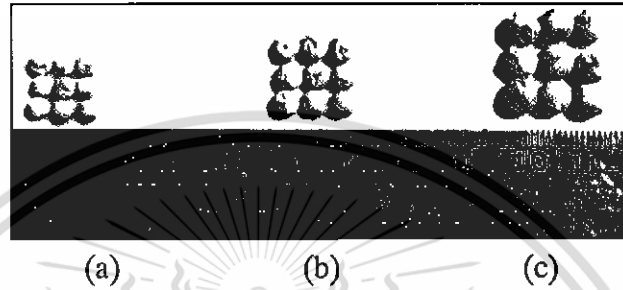


Figure 3.1 Photographs of different size spherical preforms for producing aluminium foams: (a) 4.0 - 4.2 mm, (b) 4.9 – 5.1 mm and (c) 6.2 – 6.4 mm.

Table 3.1 Chemical compositions of AC2A (A319) aluminium alloy used for producing aluminium foams in this work.

Element	Si	Cu	Mg	Fe	Mn	Zn	Ti
(Wt.%)	4.67	4.13	0.22	0.18	0.02	0.01	0.01

Aluminium foam production was carried out using space holder method. Three different sizes of spherical balls, as shown in **Figure 3.1**, and AC2A aluminium alloy, whose compositions are shown in **Table 3.1**, were used as space holders and a cast metal for producing aluminium foams in this work. The spherical preforms, which were produced using NaCl particles combined with inorganic substance, were sieved using diamond sorting sieves (Pierres) to obtain three different sizes: 4.0 – 4.2, 4.9 – 5.1 and 6.2 – 6.4 mm. These preforms were used for porous creation in aluminium foam structure having interconnection between each pore. For debinding binder, the preforms were heated in an electrical resistance furnace at temperature of 600°C for 3 hours. There are three steps of aluminium foam production as shown in **Figure 3.2**. Firstly, preforms of 150 g were poured into a plaster mold and then randomly packed using a vibration motor (Model MVE 41M) with 3,000 rpm for approximately 60 seconds to obtain theoretical packing density and hence void fraction of 0.641 and 0.359, respectively [82]. Vibration was employed to allow preforms to shift about their position to seek for more stable position. The plaster mold with compacted preforms was subsequently preheated in an electrical resistance furnace at 600°C with the heating rate of 250°C/Hrs. prior to move to a vacuum chamber. A ladle having a thermocouple attached for monitoring temperature was used

to pour molten aluminum alloy into the plaster mold. The temperature of molten aluminium alloy dropped about 10°C during transfer. In order to infiltrate molten aluminium alloy into space of the compacted performs completely, vacuum pressure was immediately applied to the vacuum chamber once the molten metal was poured. The metal was left for 5 minutes to solidify prior to suddenly submerge in water for breaking the plaster mold and leaching the preforms.

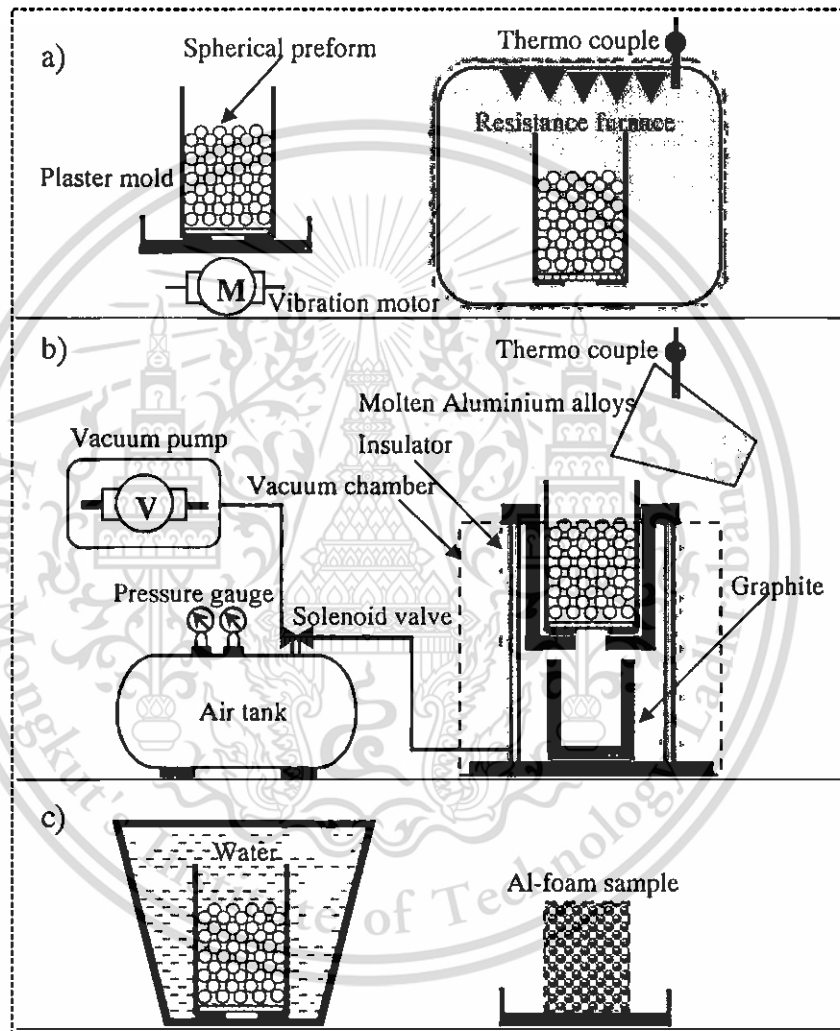


Figure 3.2 Schematic diagram of aluminium foam production using vacuum infiltration method: a) preparation of space holder and mold, b) infiltration with molten Al alloys and c) space holder removal.

3.2 Investigation of Infiltration Parameters on Aluminium Foam Structure

Parameters influencing aluminium foam structure: gas permeability through mold drainage, initial infiltration pressure and melt temperature, were investigated in this work.

Forbidden to modify the content, and cite the document when use.

Physical properties of aluminium foams related to these parameters will be given in chapter 4. Details of each parameter are given below.

3.2.1 Gas permeability through mold drainage

The degree of drainage, designated as D , of plaster molds having different bottom end was measured using the measurement of permeability which is the ability of a porous material to allow fluids to pass through it. The plaster molds used for aluminum foam production in this work contained spherical preforms of 76 mm height as shown in schematic in **Figure 3.3**. The permeability of each mold was measured using the equipment set-up as shown in **Figure 3.4**. In measurement of permeability of a porous medium, type of gas flow through the porous medium is a prime determination to permeability. For laminar flow (Reynolds number is in the range 1 to 10), permeability is a part of the proportionality constant in Darcy's law which relates fluid flow and properties to pressure gradient applied to the porous medium as given by the equation.

$$K = \frac{\mu QL}{A(\Delta P)} \quad (3.1)$$

where K is the gas permeability of porous medium, μ is the viscosity of fluid at measured temperature (kg/m-s), Q is the volumetric flow rate (l/min), L is the length of specimen in the flow direction (m), A is the cross-sectional area of the specimen perpendicular the direction of fluid flow (m²) and ΔP is the different pressure over the specimen length. In case of the Reynolds number higher than 10, the gas permeability of a porous medium can be determined using Forchheimer's equation as give below.

$$-\frac{\Delta P}{L} = \frac{\mu}{K}V + \beta\rho V^2 \quad (3.2)$$

where V is the fluid velocity averaged over the total cross-section of the porous specimen (m/s), β is the inertial parameter and ρ is the density of fluid at the measured temperature [38].

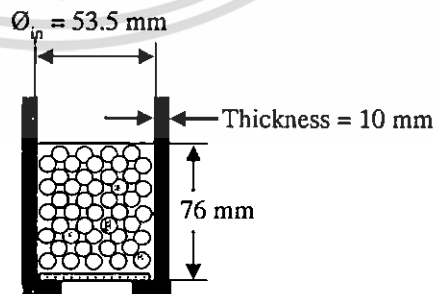


Figure 3.3 Plaster mold with spherical preforms used for producing aluminiums foams.

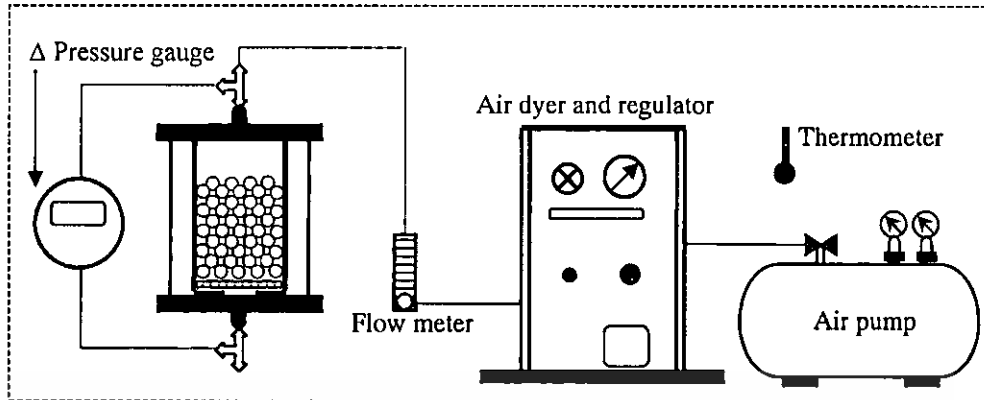


Figure 3.4 Schematic diagram of equipment used for gas permeability measurement.

3.2.2 Initial Infiltration Pressure

Table 3.2 Parameters used in different experimental schemes of aluminium foam production.

Experimental scheme	Initial pressure (-kPa)	Permeability of mold drainage (m^2)	Pouring temperature ($^{\circ}C$)	Average preform size (mm)
P - I	0 - 100	44.35	725	6.3
P - II	20 - 95	31.26	620	6.3
P - III	10 - 30	44.35	620	6.3

Infiltration pressures in the range 0 to -100 kPa were applied to the vacuum chamber to infiltrate molten aluminium into space of spherical preforms. The infiltration pressure was designated as P (0 – 100 kPa) which was applied by small and large pressure storage tank. Three experimental schemes using different parameters: initial pressure, mold drainage permeability, pouring temperature and preform size, as given in Table 3.2 were used in order to obtain different foam structures. Results of these investigations are shown in Section 4.1.2 - 4.1.3 (in chapter 4).

The threshold pressure which is an initial minimum pressure applied to infiltrate molten aluminium into space of preforms of different sizes can be predicted using Young-Laplace equation [40] as given below.

$$P_{th} = \frac{2\sigma_{LV}\cos\theta}{r} \quad (3.3)$$

where P_{th} is the threshold pressure (MPa), σ_{LV} is the liquid-vapour surface tension (N/m), θ is the contact angle between liquid and solid interface and r is the radius of spherical pore diameter (μm).

The extent of molten aluminium infiltrating into space of the preforms, S , can be calculated using the below equation [23].

$$S = \frac{V_m}{1 - V_r} = 1 - \left(\frac{P_b}{P}\right)^\lambda \quad (3.4)$$

where saturation (S) is the extent of infiltration by molten metal, V_m and V_r are the volume fraction of metal and preforms, P_b is the bubbling pressure (threshold pressure), P is the applied pressure and λ is pore size distribution index.

3.2.3 Melt Temperature

Melt temperatures in the range 625 – 735°C and 630 - 690°C were used in aluminium foam production under the control of initial pressure, mold drainage permeability and preform size as shown in Table 3.3. Results of these investigations are shown in Section 4.1.3 (Chapter 4). The temperature of molten aluminium alloy dropped about 10°C during transfer by ladle which took approximately 5 – 10 s.

Table 3.3 Parameters used for producing aluminium foams using different pouring temperatures.

Experiment scheme	Pouring temperature (°C)	Initial pressure (-kPa)	Permeability of mold drainage (m ²)	Average preform size (mm)
T - I	625 - 735	100	44.35	6.3
T - II	630 - 690	95	31.26	6.3

3.3 Characterisation

3.3.1 X-Ray and CT-Scan Imaging

Conventional method of cross-sectioning as well as novel CT-scan and X-ray imaging technologies were employed for establishing the architectural structures of the foam. The x-ray and DentiScan NSTDA Manufacturer CT-scan imaging technologies were employed for establishing the architectural structures of the aluminium foam samples. A X-ray machine was conducted at 210 kV and 0.3 mV for observation along vertical and horizontal axis. A CT-scan machine was conducted at 90 kV with slice thickness of 0.4 mm, resolution of 2.5 pixels per mm and pixel size of 0.4 x 0.4 x 0.4 mm. Slice data were reconstructed using ImageJ 1.47d software which is an open image analysis software.

3.3.2 Density and Porosity

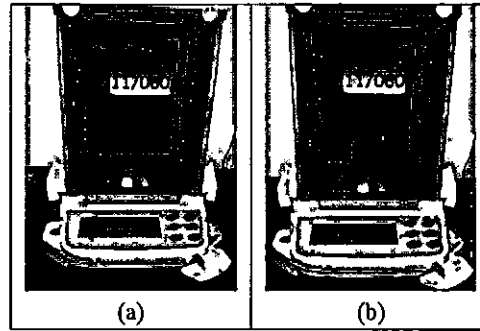


Figure 3.5 Weight measurement of aluminium foams: (a) cross-section and (b) bulk.

Density of aluminium foams was determined using weight-volume measurement given by equation

$$\rho_f = \frac{m}{V} \quad (3.5)$$

where ρ_f is the bulk density of aluminium foam, m is the dry weight of aluminium foam which was dried in an oven at 90°C for 6 hours after leaching preforms and v is the volume of aluminium foam. Density from bottom to top at interval of 10 mm was measured using a balance with 4 digits of decimal as shown in **Figure 3.5**.

After using micro-CT and X-Ray analysis structure of aluminium foams. Aluminium foams with densities below 0.26 g/cm³ were prepared for porosity measurement in 3 steps: dyeing resin with black colour paint, mounting in a cylindrical tube and sectioning with a band saw. Aluminium foam with higher densities, on the other hand, can be directly cut using a band saw. Example of a low density aluminium foam is shown in **Figure 3.6**. Each aluminium foam was sectioned from bottom to top at 10 mm interval. Each section was subsequently ground with sand papers. Sections with good smooth surface were scanned to obtain clear images for image analysis of porosity.

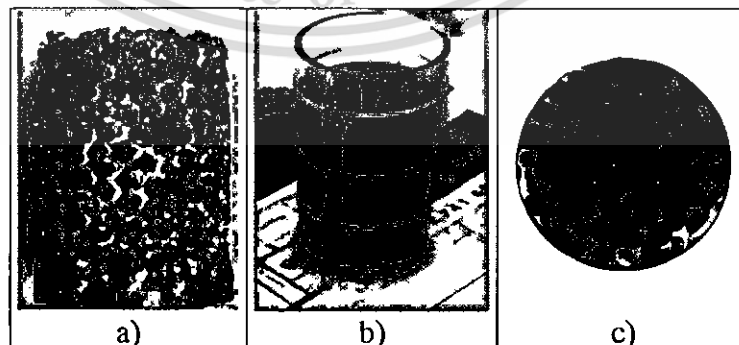


Figure 3.6 Aluminium foam: (a) as-cast, (b) mounted in a cylindrical tube using resin dyed with black colour paint and (c) sectioned specimen.

Porosity, which is the ratio of sectional area that belongs to the pore space and the total sectional area, was selected as a structural parameter for determination the validity of measurement with images taken from different sources or colour adjustment. All acquired images which are obtained by means of scanning using a multifunction color laser printer (Fuji Xerox DocuPrint CM305 df) with setting parameters: 600 x 600 dpi resolution were manipulated for each of image enhancement levels, using Photoshop software, as representatively shown in **Figure 3.7** in order to convert to black and white image. The black and white images were measured using ImageJ 1.47d software. Calculation of specimen porosity was carried out using the below equation.

$$\varepsilon (\%) = \left(\frac{Area_{air}}{Area_{total}} \right) \times 100 \quad (3.6)$$

where ε (% Porosity) is the ratio of sectional area that belongs to the pore space ($Area_{air}$), and the total sectional area ($Area_{total}$). Alternatively, porosity can be calculated using the below equation.

$$\varepsilon (\%) = \left(1 - \frac{\rho_f}{\rho_0} \right) \times 100 \quad (3.7)$$

where ε is the porosity of aluminium foam, ρ_0 is the theoretical density of aluminium alloy whose physical properties were obtained from ProCAST software database and ρ_f is the measured density of aluminium foam which was calculated using equation (3.5).

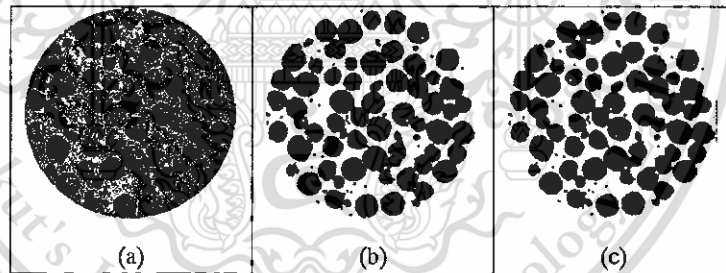


Figure 3.7 Images of aluminium foams measured using image analysis method: (a) scanned image, (b) B&W image and (c) pore area thresholded by imageJ software.

3.3.3 Pore Size and Aperture Size

Pore size and aperture (pore opening) size are important parameters of aluminium foam structure which can be obtained from the same technique of image analysis used for porosity measurement. Acquired images of pores and apertures were taken using a DSLR camera with macro lens focusing on interest areas to obtain good contrast images, which facilitates for black and white conversion as shown in **Figure 3.8** - **Figure 3.9**. Particle analysis function in ImageJ software was used to measure the specific area of pores and apertures. These results were used for sound absorption characterisation of aluminum foams shown in chapter 4.

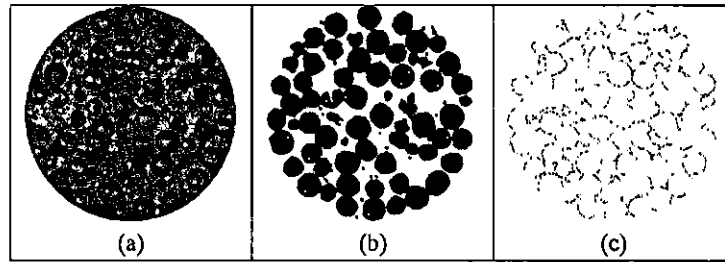


Figure 3.8 Pores of an aluminium foam measured using image analysis method: (a) image taken using a DSLR camera with macro lens, (b) B&W image adjustment and (c) pores thresholded by ImageJ software.

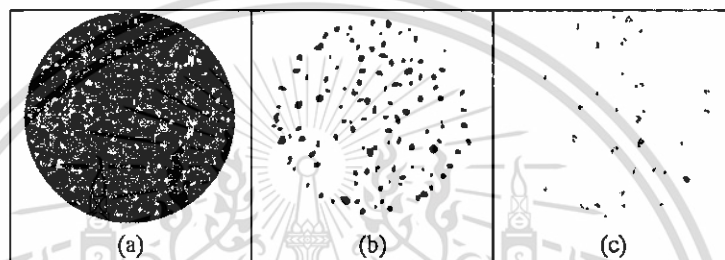


Figure 3.9 Apertures of an aluminium foam measured using image analysis method: (a) image taken using a DSLR camera with macro lens, (b) B&W image adjustment and (c) apertures thresholded by ImageJ software.

3.3.4 Compressive test



Figure 3.10 An Instron 8801 universal testing machine used for compressive tests.

This material is reserved for educational use only, not allowed for commercial use.

Forbidden to modify the content, and cite the document when use.

Specimens for compressive tests were taken from cylindrical open cell aluminium foams with porosities in the range 67 – 71% and 91 – 93%, and pore sizes 4.1, 5.0 and 6.3 mm. Both ends of the specimens were cut using a band saw and paralleled using a turning machine. Dimensions and some physical properties of the specimens are shown in **Table 3.4**. The compressive tests were carried out using an Instron 8801 universal testing machine having a maximum axial load capacity of 100 kN. These compressive tests were performed at a strain rate of 0.001 s^{-1} until 80% of compressive strain. During compressive tests, deformation of each specimen was recorded using a video camera. Young's modulus (E), plateau stress (σ_{pl}) and densification strain (ϵ_d) of each specimen were determined from stress-strain curves.

Table 3.4 Dimensions and some physical properties of open cell aluminium foam specimens used for compressive test.

Properties	Sample 1	Sample 2	Sample 3	Sample 4	Sample 5	Sample 6
Thickness (mm)	57.7	60.39	61.89	61.74	65.61	64.15
Diameter (mm)	53.37	53.50	53.56	53.40	53.14	53.23
Pore size (mm)	4.1	5.0	6.3	4.1	5.0	6.3
Relative density (%)	0.31	0.35	0.35	0.08	0.08	0.10
Porosity (%)	71	67	67	93	92	91

3.3.5 Acoustic Measurement

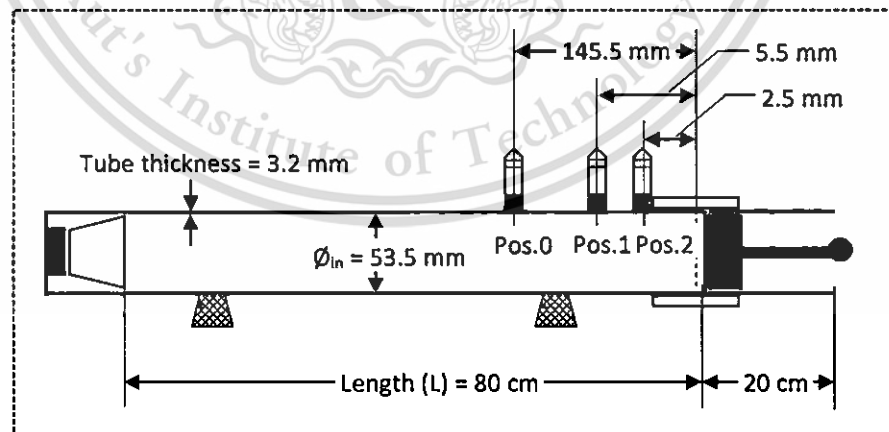


Figure 3.11 Dimension of impedance tube based on ASTM E1050-98.

Specimens for sound absorption tests were taken from cylindrical open cell aluminium foams with porosities in the range 67 – 71% and 91 – 93%, pore sizes 4.1, 5.0 and 6.3 mm, diameter of 53.5 mm, and thicknesses 10 – 20 mm. The sound absorption tests were carried out with frequencies in the range 125 to 3,150 Hz using two-microphone

impedance tube according to ASTM E1050-98 (ASTM, 1998) standard, as shown in **Figure 3.11**. A Meguro MAK-6581 audio analyser, NI USB-9234 data logger and BSWA software were used to generate sound, record data and analyse data, respectively. **Table 3.5** shows specifications of the impedance tube. The working frequency range, tube diameter and microphone spacing were calculated using equations 2.50 – 2.52 (in chapter 2.7.2).

Table 3.5 Impedance tube specifications.

Parameter	ASTM E1050-98
Test frequency	125 - 3,150 Hz
Material of impedance tube	Cylindrical acrylic tube having a thickness of 3.2 mm
Inner diameter of impedance tube	53.5 mm
Loud speaker	3" in diameter, 10 watts
Distance between Mic.2 and sample	2.5 mm
Distance between Mic.2 and Mic.1	3 mm
Distance between Mic.0 and Mic.2	14 mm
¼" Microphone	Super lux ECM 888B
Data acquisition	NI USB-9234
Power amplifier	6 W EPS-305
Frequency generator	Meguro MAK-6581 Audio Analyzer
Software	VA-LAB 4 IMP

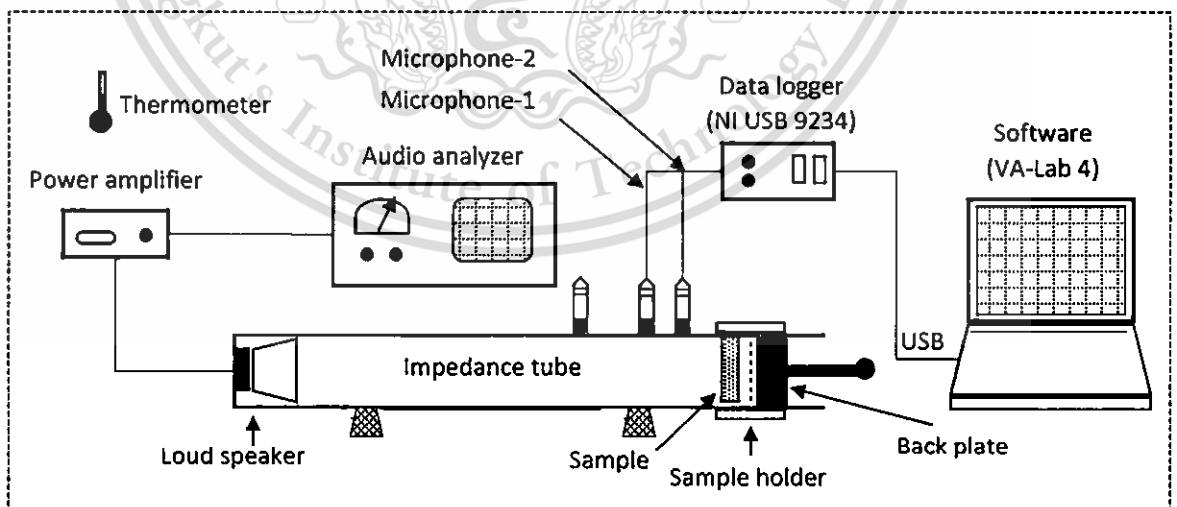


Figure 3.12 Schematic diagram of sound absorption test based on ASTM E1050-98 impedance tube method using two microphones.

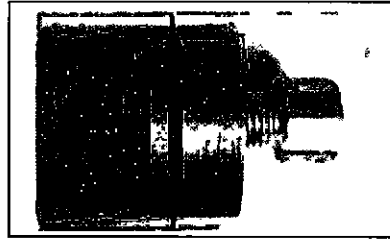


Figure 3.13 Felt having thickness of 20 mm and weight of $2,000 \text{ g/m}^2$ was used to determine the accuracy of the set-up of impedance tube.

Figure 3.12 shows schematic diagram of sound absorption test using two microphones method and VA-LAB 4 IMP software to measure sound absorption coefficients. Before measurements conducted, the specimen with known sound absorption properties, as shown in **Figure 3.13** was used for sound absorption test to roughly determine the accuracy of the set-up of the impedance tube in order to minimise errors in actual measurements. For each sound absorption test, two microphones having sensitivity of 7.1 mV/Pa were calibrated using sound with amplitude of 94 dB at $1,000 \text{ Hz}$ (see also in appendix II). Each specimen was inserted into a sample holder of the impedance tube. Sound absorption tests were carried out using $1/3$ octave of frequencies in the range 125 to $3,150 \text{ Hz}$ for sound absorption coefficient measurement. Equations for sound absorption calculation have been given in section 2.2.2 in literature review. Sound tests were performed for each sample two times in order to average values of sound absorption coefficient. **Figure 3.14** shows sound absorption coefficients r of felt specimen taken from a manufacturer compared with those measured using the impedance tube [83].

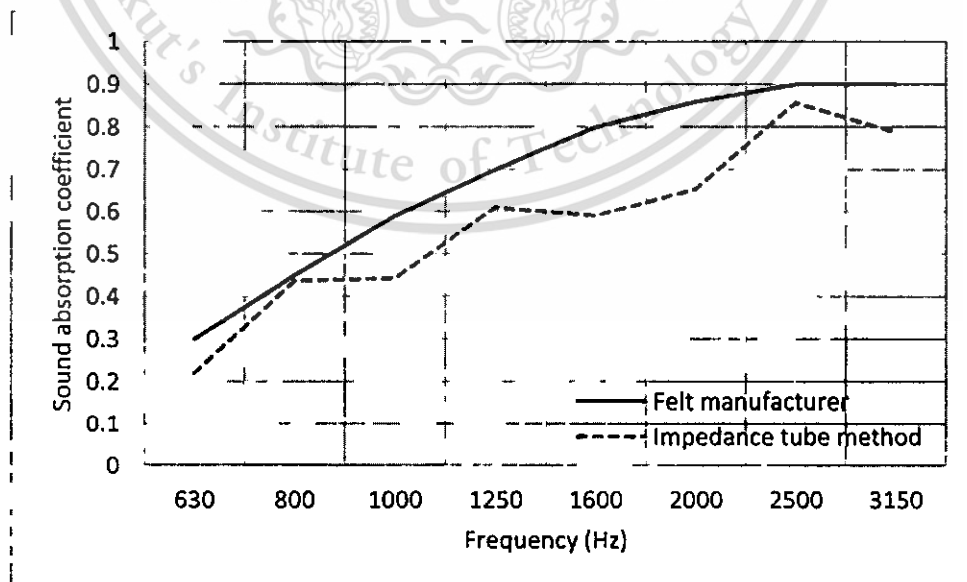


Figure 3.14 Comparison of sound absorption coefficients of felt specimen between those obtained from manufacturer and impedance tube measurement [83].

This material is reserved for educational use only, not allowed for commercial use.

Forbidden to modify the content, and cite the document when use.

CHAPTER 4 RESULTS AND DISCUSSION

Figure 4.1 illustrates photographs of open cell aluminium foams produced using infiltration of liquid metal into space locating among specific size of spherical preform. Both spongy (Figure 4.1 (a)) and dense foams (Figure 4.1 (b)) were produced by varying production parameters as given in Figure 4.1. Some produced aluminium foams were sectioned as shown in Figure 4.1 (c) for characterisations of foam structure and tests their sound absorption properties. Results and discussion of production parameters, characteristics and sound absorption properties of the produced aluminium foams are respectively given in this chapter. Recommendation for automotive components possibly made by these open cell aluminium foams is given in the last section of this chapter.

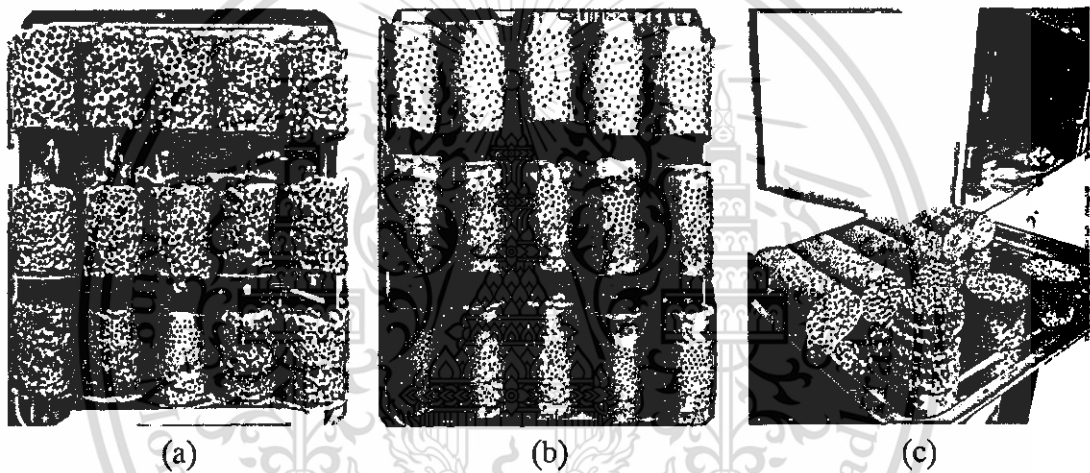


Figure 4.1 Photographs of aluminium foams produced from infiltration of molten metal into the space holder of spherical preform sizes 4.1, 5.0, and 6.3 mm: (a) spongy, (b) dense and (c) sectioned aluminium foams.

Table 4.1 Production parameters and characteristics of aluminium foams.

Production parameters	Aluminium foam characteristics
Mold permeability types: 1 - 8	Density (g/cm^3)
Initial vacuum pressure (kPa): -100 - 0	Porosity (%)
Melt temperature ($^{\circ}\text{C}$): 680 - 770	Infiltrated zone (wt%)
Spherical preform size ($\text{mm} \pm 0.1 \text{ mm}$): 4.1, 5.0 and 6.3	Saturation (extent of infiltration)

4.1 Influence of Production Parameters

4.1.1 Effect of Gas Permeability through mold drainages


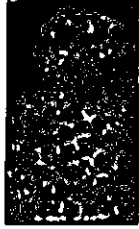
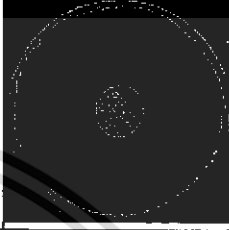
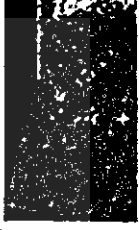
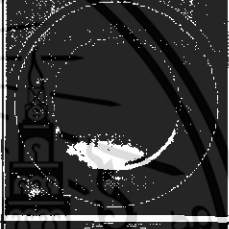
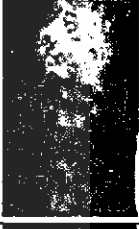

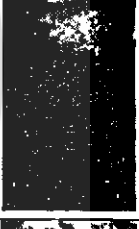
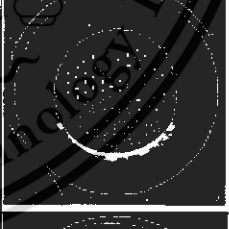
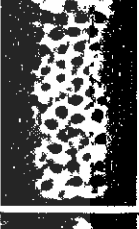
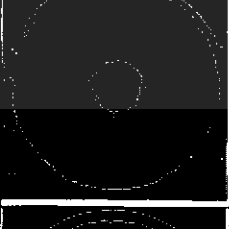

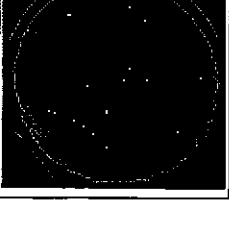

This material is reserved for educational use only, not allowed for commercial use.

Forbidden to modify the content, and cite the document when use.

Gas permeability of molds containing 150 g of 6.3 mm spherical performs packed by vibration for 60 s was measured. The molds contain different drainage base and open hole size as shown in **Table 4.2** which also includes photographs of aluminium foam produced by each mold with identical production parameters. It can be seen that different structure of aluminium foams can be obtained by varying molds' drainage base and open hole size. Each mold exhibited different permeability characteristics as illustrated in **Figure 4.2** which shows in terms of gas flow rate against different pressure. From this figure, higher gas flow rate at a different pressure represents higher gas permeability. Base on the gas permeability results shown in **Figure 4.2** and photographs of the produced aluminium foams shown in **Table 4.2**, one can classify the degree of permeability of each mold as high, medium and low represented by initial letters H, M and L, respectively. It can be seen that molds with high permeability gave sponge foams, medium permeability gave dense foams and low permeability gave incomplete foams. The plots shown in **Figure 4.2** can be used to calculate permeability coefficients (K) of the molds using Forcheimer equation given by Equation 2.3 and the results are plotted against mold drainage type ordered by the level of permeability as shown in **Figure 4.3**. It can be seen from this figure that there is a wide range of permeability coefficients ($8.50 \times 10^{-12} - 43.12 \times 10^{-12} \text{ m}^2$) to give foams with dense structure. To estimate permeability coefficient of mold drainages (K), flow rate of fluid against different pressure at specific mold drainage types (H1 – L2) as shown in **Table 4.2**, were plotted to calculate the permeability coefficients obtained from slope and parameters¹ using Forcheimer equation given by Equation 2.3. The different structure of open cell aluminium foams obtained in this work can be depicted by three types as shown in **Figure 4.4** whose typical zones of infiltration; residue, retained and infiltrate metal, are shown in **Figure 4.5**. Type I represents for incomplete aluminium foams whose molten metal completely un-infiltrates or partial infiltrates. In type II, since there is residue metal without infiltrate metal, full infiltration will give dense and complete foams. In type III, no residue metal is found but infiltrate metal is present, therefore full infiltration will give spongy foams.



Table 4.2 Results of different drainage molds for producing aluminium foams with AC2A aluminium alloys using pouring temperatures 715 – 720 °C and initial vacuum pressure -100 kPa.

¹ Substituting $L = 0.078 \text{ m}$, $A = 0.053 \text{ m}$, slope of $(\mu L/k_p) = 33629$ obtained from fitting curve of H2 mold drainage type as shown in **Figure 4.2** in Equation (2.3), $\mu = 1.86 \text{ kg/m}^3 \times 10^{-5}$ and $\rho = 1.17 \text{ kg/m}^3$ (calculated from physical properties table at $T = 27.6 \text{ }^\circ\text{C}$), gives $K = 43.12 \times 10^{-12} \text{ m}^2$.

No.	Mold vent (mm)	Mold drainage type	Permeability $K \cdot 10^{-12} (m^2)$	Photograph of mold drainage base	Photograph of sample
H1	42	Stainless steel perforate plate	44.28		
H2	15	Stainless steel perforate plate	44.35		
M1	42	Compressive NaCl plate	43.12		
M2	15	Stainless steel perforate plate + small hole NaCl plate	38.98		
M3	42	Stainless steel perforate plate + castable NaCl plate	31.26		
M4	15	Stainless steel perforate plate + castable NaCl plate	8.50		
L1	0	-	0		

This material is reserved for educational use only, not allowed for commercial use.

Forbidden to modify the content, and cite the document when use.

L2	0	Compressive NaCl plate	0		
----	---	------------------------	---	--	---

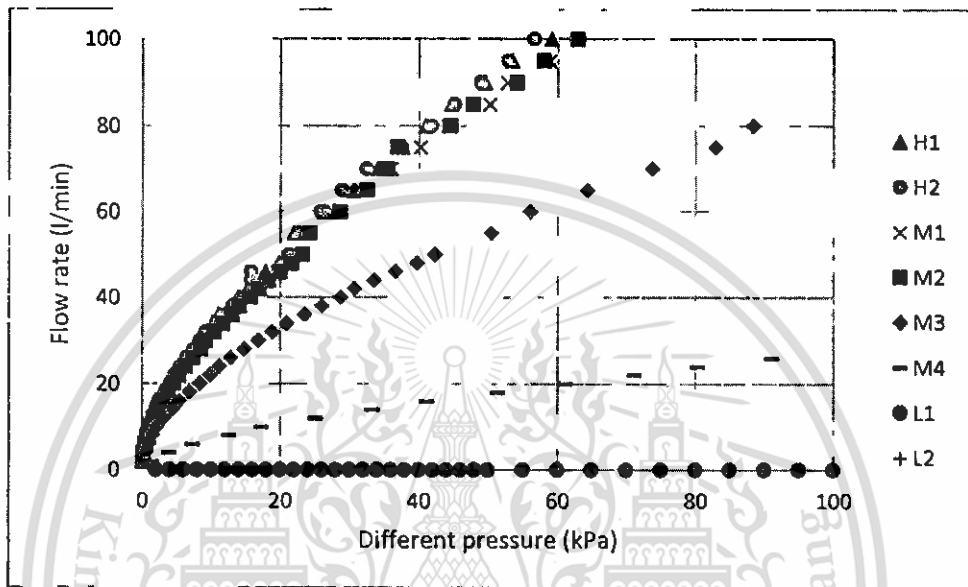


Figure 4.2 Results of different pressure versus flow rate of air through mold with varying of drainage contained 6.3 mm diameter preform and 150 g inside are produced aluminium foams.

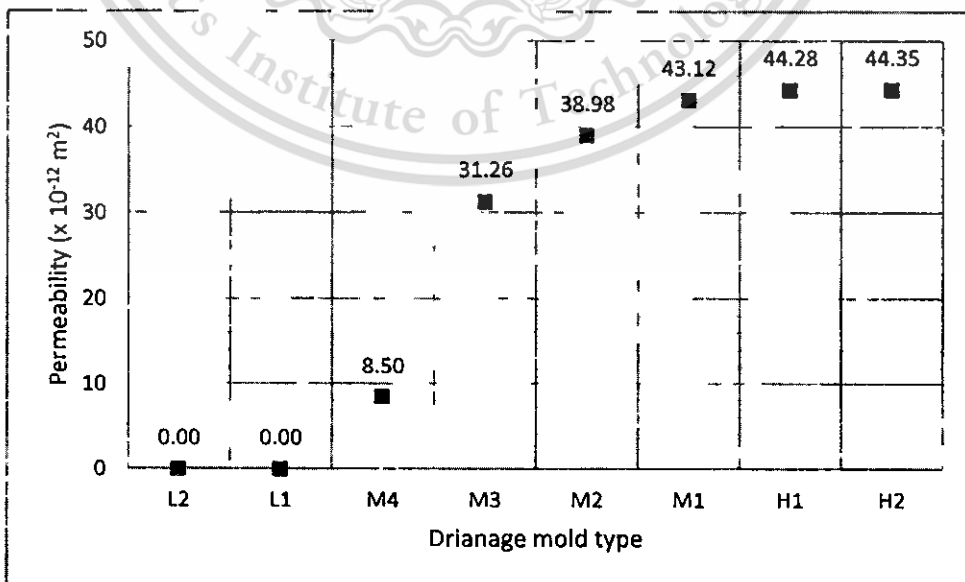


Figure 4.3 Gas permeability coefficient of molds having different drainage bases.

This material is reserved for educational use only, not allowed for commercial use.

Forbidden to modify the content, and cite the document when use.

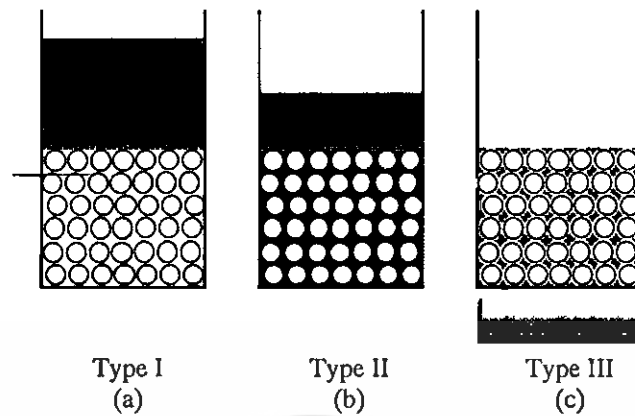


Figure 4.4 Infiltration types of open-cell aluminium foam structure: (a) no infiltration, (b) full infiltration with residue metal and (c) full infiltration without residue metal.

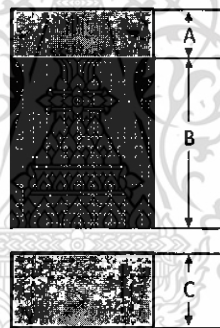


Figure 4.5 Defined zones of molten metal infiltration in space holder: A = residue metal, B = retained metal and C = infiltrate metal.

Figure 4.6 shows photographs of aluminium foams prior to preform elimination, showing corresponding foam structures with those depicted in **Figure 4.4**. Percentage of each infiltration zone and type of infiltration of each aluminium foam are illustrated in **Figure 4.7**. It can be seen from this figure that aluminium foam having permeability of zero contained majority of residue metal and the rest of retained metal. Due to the absence of permeability of the mold, there was no assisting pressure during infiltration and hence molten metal could not completely fill the space locating among spherical performs. As a result of this, aluminum foam produced with zero permeability mold was incomplete and classified as type I of infiltration. For aluminium foams produced using molds with permeability coefficients $8.50 \times 10^{-12} - 38.98 \times 10^{-12} \text{ m}^2$, they contained all metal infiltration zones defined in **Figure 4.5** and are classified as type II of infiltration. Residue and infiltrate metals were found to increase, while retained metal was found to decrease with increasing mold permeability. The residue and retained

metals were much lower and higher, respectively, comparing with those of aluminium foams produced using mold with permeability of zero. This showed the important function of permeability in producing aluminium foam using infiltration method. To receive a complete aluminium foam, sufficient mold permeability is required to allow molten metal to fulfill infiltration into space existing in preforms. For aluminium foams produced using molds with permeability coefficients $44.28 \times 10^{-12} - 44.35 \times 10^{-12} \text{ m}^2$, the produced aluminium foams contained only retained and infiltrate metals and are classified as type III of infiltration. The retained and infiltrate metal were found to decrease and increase, respectively, with increasing mold permeability. The amount of retained and infiltrate metals was significantly lower and higher, respectively, comparing with those found in aluminium foams with type II of infiltration. The degree of infiltration of the produced aluminium foams can be determined by saturation (extent of fill space within preforms by molten metal) given by Equation (2.14) – (2.17) and density given by Equation (3.5). By replacing parameters² in Equations (2.14) – (2.17), saturation and density of the produced aluminium foams can be obtained as shown in **Figure 4.8**. It can be seen from this figure that the trend of change with permeability coefficient of saturation and density was similar. Type II aluminium foams exhibited highest saturation and density, followed by type I and type III aluminium foams, respectively. It is interesting to notice from this figure that, for a constant initial vacuum pressure, pouring temperature and preform size, aluminium foams can be produced to obtain required densities by using molds with suitable permeability. The control of

² Substituting $m_f = 104.1, 122.9$ and 137.62 g of spherical preform size = 4.1, 5.0 and 6.3 mm of dense samples with $\rho_{ACZA} = 2.79 \text{ g/cm}^3$ in Equation (2.16) gives $V_{m'} = 37.32, 43.83$ and 49.33 cm^3 . Replacing $V_{m'} = 37.32, 43.83$ and 49.33 cm^3 , $V_f = 148.16, 157.90$ and 153.41 cm^3 of spherical preform size = 4.1, 5.0 and 6.3 mm in Equation (2.15) gives $V_m = 0.25, 0.28$ and 0.32 . Replacing $V_p = 152.86, 161.86$ and 170.85 cm^3 of spherical preform size = 4.1, 5.0 and 6.3 mm in Equation (2.17) with $\rho_{preform} = 1.67 \text{ g/cm}^3$ and $m_p = 150 \text{ g}$ gives $V_r = 0.59, 0.55$ and 0.53 . Replacing V_r and V_m in Equation (2.14) gives $S = 0.61, 0.62$ and 0.68 for spherical preform size = 4.1, 5.0 and 6.3 mm of dense samples respectively.

Substituting $m_f = 47.28, 35.46$ and 33.98 g of spherical preform size = 4.1, 5.0 and 6.3 mm of spongy samples with $\rho_{ACZA} = 2.79 \text{ g/cm}^3$ in Equation (2.16) gives $V_{m'} = 16.95, 12.71$ and 12.18 cm^3 . Replacing $V_{m'} = 16.95, 12.71$ and 12.18 cm^3 , $V_f = 147.87, 155.59$ and 174.77 cm^3 g of spherical preform size = 4.1, 5.0 and 6.3 mm in Equation (2.15) gives $V_m = 0.11, 0.08$ and 0.07 . Replacing $V_p = 152.86, 161.86$ and 170.85 cm^3 of spherical preform size = 4.1, 5.0 and 6.3 mm in Equation 2.16 with $\rho_{preform} = 1.67 \text{ g/cm}^3$ and $m_p = 150 \text{ g}$ gives $V_r = 0.59, 0.55$ and 0.53 . Replacing V_r and V_m in Equation (2.14) gives $S = 0.28, 0.18$ and 0.15 for spherical preform size = 4.1, 5.0 and 6.3 mm of spongy samples respectively.

foam structure using variation of mold permeability in this work has not been reported elsewhere.

In order to receive aluminum foams with spongy and dense structures, molds with drainage types H2 and M3 were chosen respectively. Conditions for producing aluminium foams to obtain such structures with different pore size are given in **Table 4.3**. Examples of an aluminium foam before and after leaching of performs are shown in **Figure 4.9**. **Figure 4.10** shows an example of aluminium foams having spongy and dense structures with different pore sizes. Densities of the produced aluminium foams are given in

Table 4.4. It can be seen clearly from this table that spongy and dense aluminium foams with density in the range $0.14 - 0.33 \text{ g/cm}^3$ and $0.76 - 0.95 \text{ g/cm}^3$, respectively, can be produced using molds with different permeabilities, while conditions of other production parameters were identical. Percentage of each infiltration zone of spongy and dense aluminium foams is shown in **Figure 4.11** and **Figure 4.12**, respectively. For spongy aluminium foams, no residue metal was present at all, while, retained and infiltrate metals were found to slightly decrease and increase, respectively, with increasing spherical preform size. For dense aluminium foams, on the other hand, no infiltrate metal was found at all, while, retained and residue metals were found to increase and decrease, respectively, with increasing spherical preform size. It is interesting to note that the trend of retained metal percentage against spherical preform size was opposite for spongy and dense aluminium foams. Due to a high surface tension of molten metal, higher size of space within spherical preforms of higher size would be responsible for the more and less metal to infiltrate resulting in more spongy and more dense aluminium foams with increasing spherical preform size, respectively. This phenomenon is clearly seen in the plot of saturation against mold permeability coefficient shown in **Figure 4.13** in that more and less saturation were found in dense aluminium foam (mold permeability coefficient of $31.26 \times 10^{-12} \text{ m}^2$) with increasing pore size and spongy aluminium foam (mold permeability coefficient of $44.35 \times 10^{-12} \text{ m}^2$) with increasing pore size, respectively.

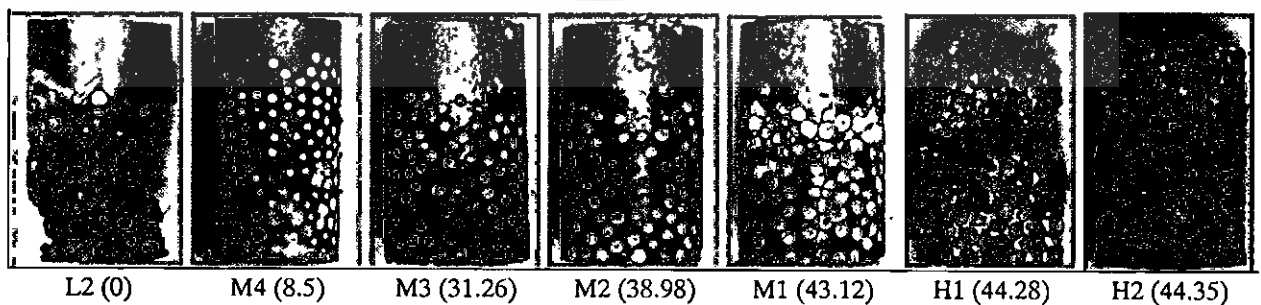


Figure 4.6 Photographs of 6.3 mm pore size aluminium foams produced using molds with drainage bases having different permeability (initial vacuum pressure, pouring temperatures and molten metal weight were kept constant as -100 kPa, 715 - 720 °C and 348 g, respectively).

This material is reserved for educational use and not to be used for commercial use.

Forbidden to modify the content, and cite the document when use.

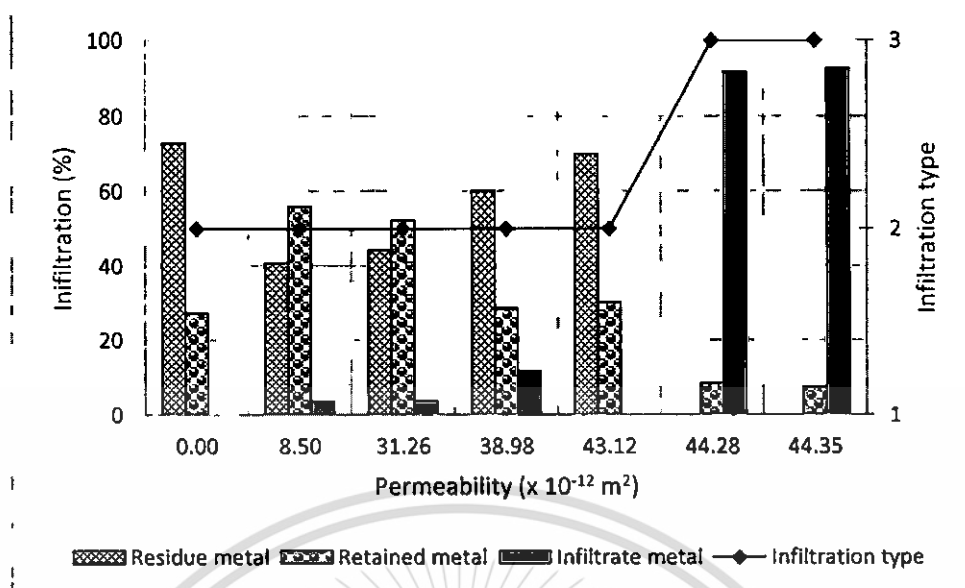


Figure 4.7 Infiltration characteristic of 6.3 mm pore size aluminium foams produced using molds with drainage bases having different permeability (initial vacuum pressure, pouring temperatures and molten metal weight were kept constant as -100 kPa, 715 - 720 °C and 348 g, respectively).

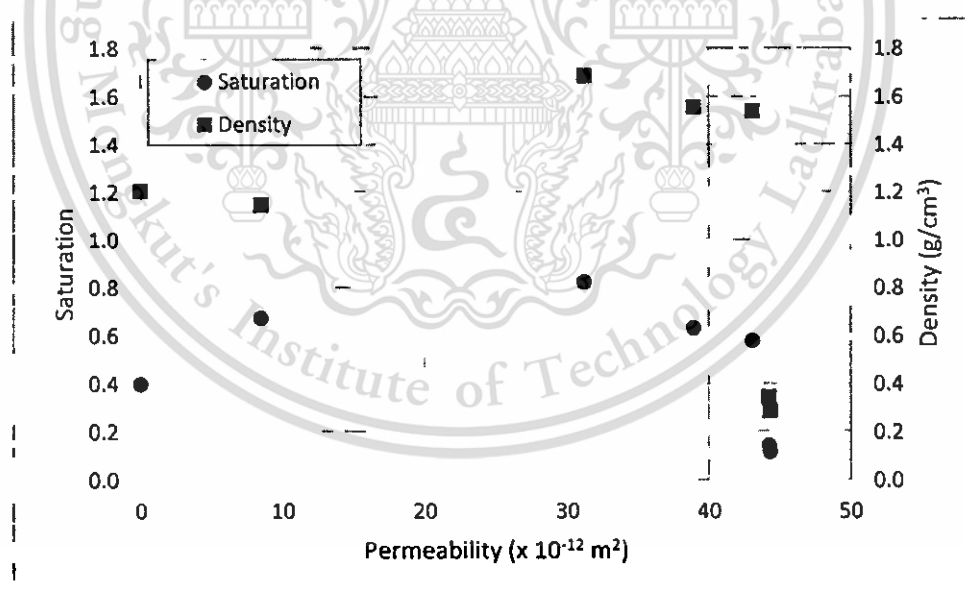


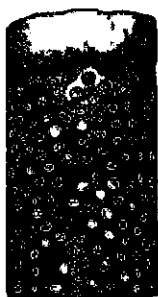
Figure 4.8 Saturation and density of 6.3 mm pore size aluminium foams produced using molds with drainage bases having different permeability (initial vacuum pressure, pouring temperatures and molten metal weight were kept constant as -100 kPa, 715 - 720 °C and 348 g, respectively).

Table 4.3 Conditions for production of three different pore size AC2A aluminium foams with spongy and dense structures.

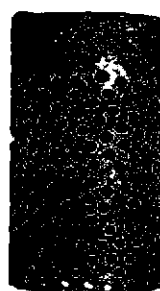
Mold drainage types	Spherical preform size (mm)	Pouring temperature(°C)	Initial vacuum pressure (kPa)
H2	4.0 – 4.2	620	-20
	4.9 – 5.1	620	-20
	6.2 – 6.4	620	-20
M3	4.0 – 4.2	620	-20
	4.9 – 5.1	620	-20
	6.2 – 6.4	620	-20

Table 4.4 Density of aluminium foams produced from AC2A aluminium alloy using conditions shown in Table 4.3.

Mold drainage types (H2)			Mold drainage types (M3)		
Sample	Pore size (mm)	Density (g/cm ³)	Sample	Pore size (mm)	Density (g/cm ³)
1	4.0 – 4.2	0.27	13	4.0 – 4.2	0.83
2		0.31	14		0.76
3		0.23	15		0.82
4		0.21	16		0.81
5	4.9 – 5.1	0.33	17	4.9 – 5.1	0.93
6		0.21	18		0.95
7		0.21	19		0.91
8		0.21	20		0.91
9	6.2 – 6.4	0.14	21	6.2 – 6.4	0.91
10		0.20	22		0.94
11		0.17	23		0.94
12		0.25	24		0.93



(a)



(b)

This material is reserved for educational use only, not allowed for commercial use.

Forbidden to modify the content, and cite the document when use.

Figure 4.9 Aluminium foams produced using mold drainage type M3 (in Table 4.2) $31.26 \text{ K} \cdot 10^{-12}$, $630 \text{ }^\circ\text{C}$, -95 kPa : (a) before and (b) after space holder removal.

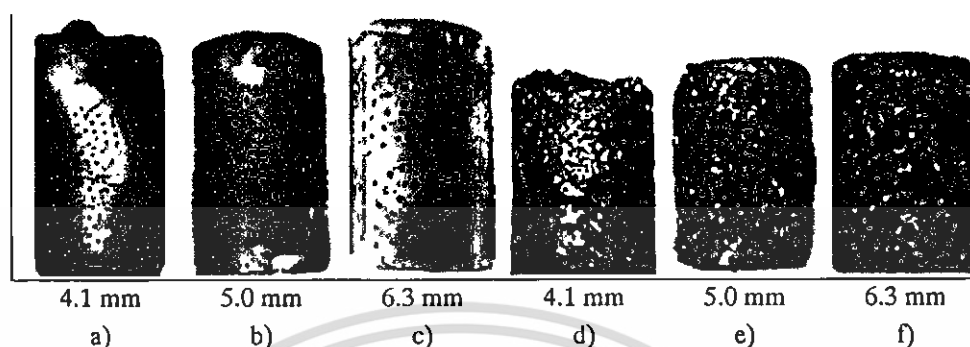


Figure 4.10 Photographs of 4.1, 5.0 and 6.3 mm pore size aluminium foams produced using molds with drainage bases having permeability coefficients: (a) – (c) 31.26×10^{-12} and (d) – (f) $44.35 \times 10^{-12} \text{ m}^2$ (initial vacuum pressure, pouring temperature and molten metal weight were kept constant as -20 kPa , $620 \text{ }^\circ\text{C}$ and 353 g , respectively).

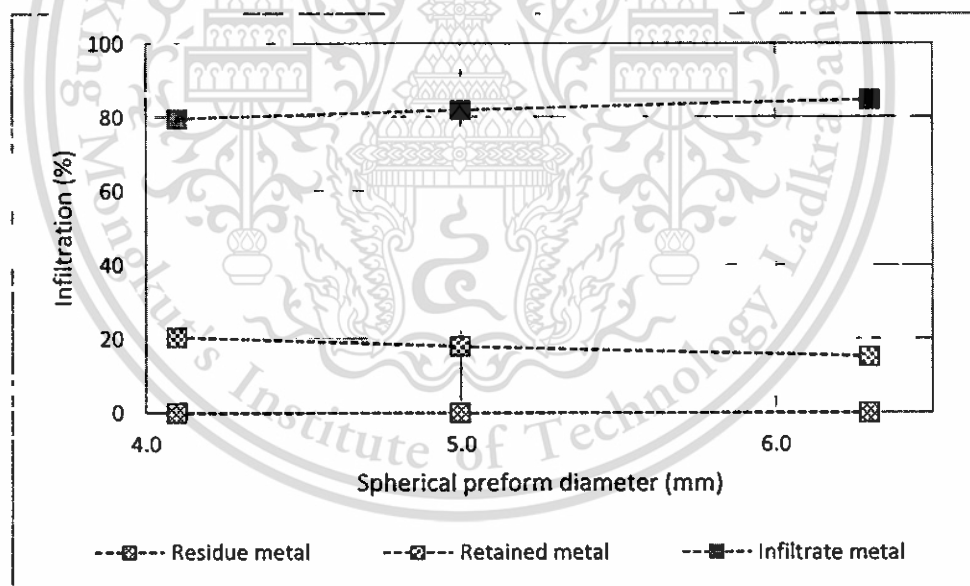


Figure 4.11 Infiltration characteristics of spongy aluminium foams produced using different spherical preform sizes (initial vacuum pressure, pouring temperatures, molten metal weight and mold permeability coefficient were kept constant as -20 kPa , $620 \text{ }^\circ\text{C}$, 236 g and $44.35 \times 10^{-12} \text{ m}^2$ respectively).

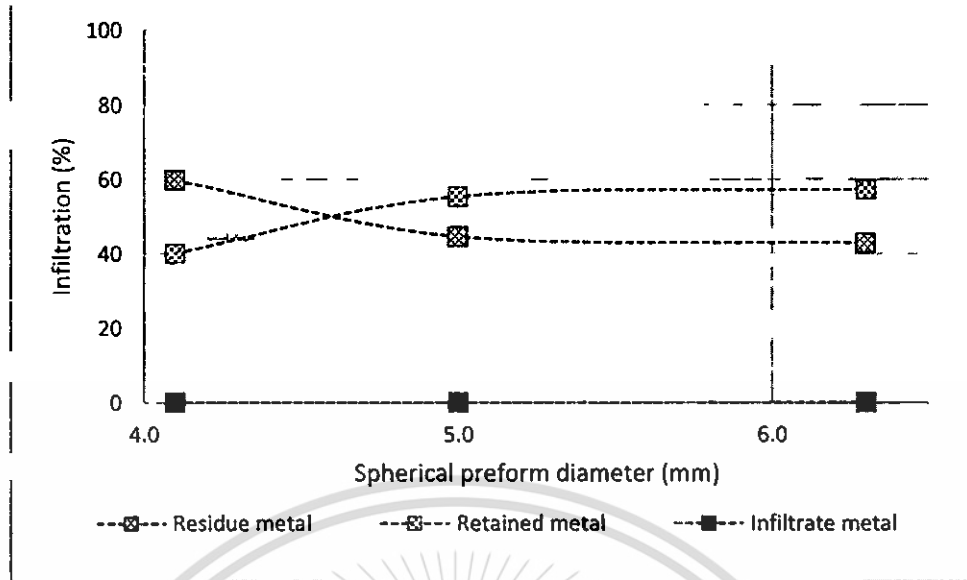


Figure 4.12 Infiltration characteristics of dense aluminium foams produced using different spherical preform sizes (initial vacuum pressure, pouring temperatures, molten metal weight and mold permeability coefficient were kept constant as -20 kPa, 620 °C, 233 g and $31.26 \times 10^{-12} \text{ m}^2$ respectively).

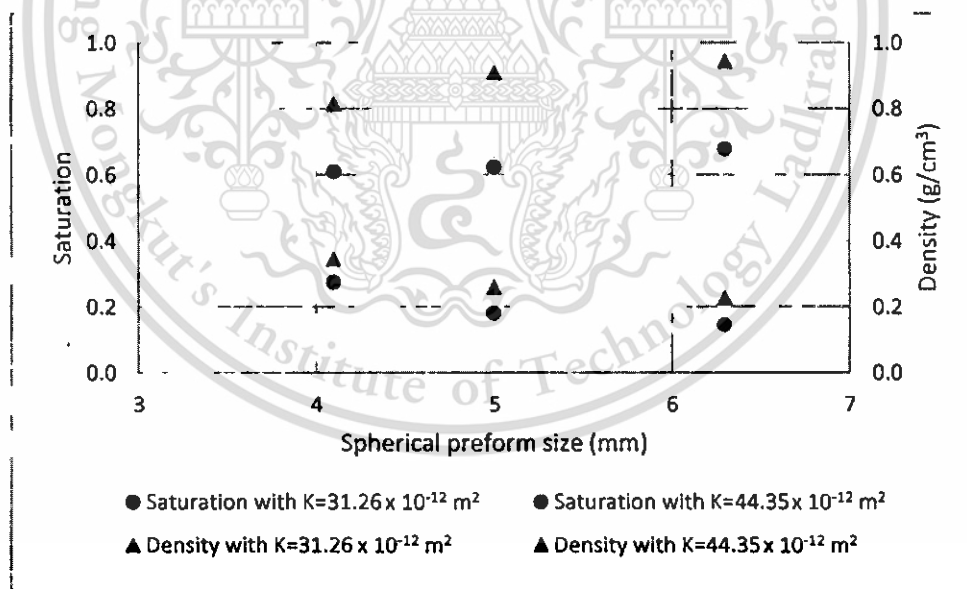


Figure 4.13 Saturation of 4.1, 5.0 and 6.3 mm pore size aluminium foams produced using molds with drainage bases having permeability coefficients $31.26 \times 10^{-12} \text{ m}^2$ and $44.35 \times 10^{-12} \text{ m}^2$ (initial vacuum pressure, pouring temperature and molten metal weight were kept constant as -20 kPa, 620 °C and 353 g, respectively).

4.1.2.1 High Mold Permeability Associating with High Pouring Temperature

Apart from the control of mold permeability, aluminium foams with different structures can be obtained by varying other production parameters such as pouring temperature, mold and preform preheat temperature, preform packing density and initial applied pressure. **Figure 4.14** shows photographs of 6.3 mm pore size aluminium foams (prior to leaching preforms) produced using different initial vacuum pressures, while, other production parameters were kept constant (mold permeability coefficient = $44.35 \times 10^{-12} \text{ m}^2$, pouring temperature = $725 \text{ }^\circ\text{C}$ and molten metal weight = 353 g). Based on the infiltration type defined in **Figure 4.4**, all of the produced aluminium foams fell into type III, except for the one produced under gravitational pressure (the initial vacuum pressure of 0 kPa) which exhibited type I, as summarised in **Figure 4.15**. To find out reason of different infiltration behaviour of this result, threshold pressure which is a minimum pressure to assist molten metal filling in space within spherical preforms was determined for different spherical preform sizes using Equation 2.4 and physical variables³ surface tension (σ_{LV}) [84], wetting angle (θ) [48]. Threshold pressure was predicted to be higher with decreasing the size of spherical preforms as shown in **Figure 4.16**. The minimum pressure to assist molten metal infiltration into space of spherical preforms with size of 4.1 , 5.0 and 6.3 mm was predicted to be -0.71 , -0.58 and -0.46 kPa respectively. The predicted threshold pressures seem to agree well with experiments of this work. Only the aluminium foam produced using initial vacuum pressure of -0.2 kPa which differed from the prediction. The actual threshold pressure of this aluminium foam may be reached the required threshold pressure of -0.46 kPa due to the addition of pressure supplying above the preforms by molten metal itself. However, without initial vacuum pressure, the molten metal itself could not infiltrate the preforms resulting aluminium foam with type I structure.

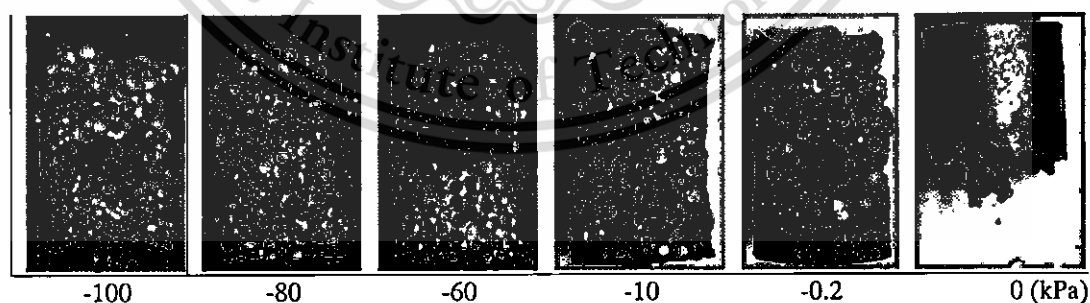


Figure 4.14 Photographs of 6.3 mm pore size aluminium foams produced using different initial vacuum pressures (mold permeability coefficient, pouring temperature and molten metal weight were kept constant as $44.35 \times 10^{-12} \text{ m}^2$, $725 \text{ }^\circ\text{C}$ and 353 g , respectively).

³ Substituting $\sigma_{LV} = 0.945 \text{ N/m}$, $\theta = 140 \text{ degree}$, $r_h = 2.05 \times 10^{-3} \text{ m}$ of 4.1 mm pore size, $r_h = 2.50 \times 10^{-3} \text{ m}$ of 5.0 mm pore size, $r_h = 3.15 \times 10^{-3} \text{ m}$ of 6.3 mm pore size in Equation (2.4) gives $P_{th} = -0.71$, -0.58 and -0.46 kPa respectively.

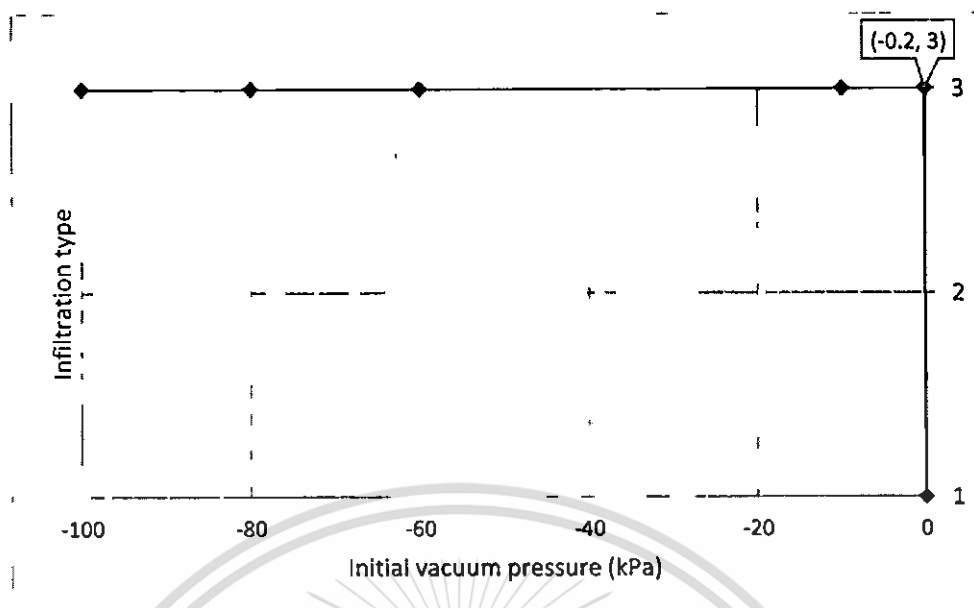


Figure 4.15 Infiltration characteristic of 6.3 mm pore size aluminium foams produced using different initial vacuum pressures (mold permeability coefficient, pouring temperature and molten metal weight were kept constant as $44.35 \times 10^{-12} \text{ m}^2$, $725 \text{ }^\circ\text{C}$ and 353 g , respectively).

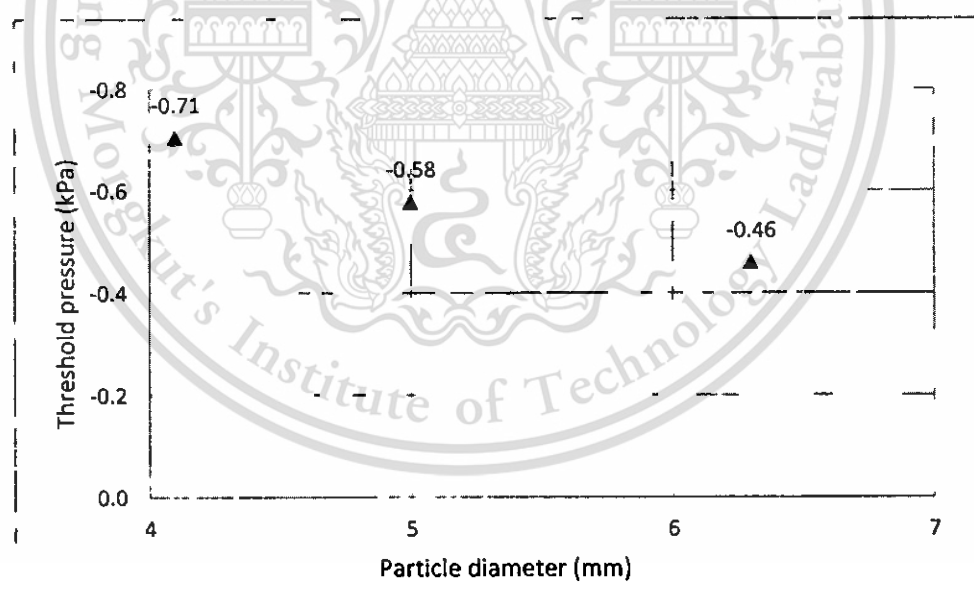


Figure 4.16 Predicted threshold pressures of aluminium foams produced using different spherical preform diameters.

4.1.2.2 Low Mold Permeability Associating with Low Pouring Temperature

Apart from types I and III, variation of vacuum pressure can also be used to produce aluminium foams with type II structure as shown for example in **Figure 4.17** for 6.3

mm pore size aluminium foams produced using different initial vacuum pressures, while, other production parameters were kept constant (mold permeability coefficient = $31.26 \times 10^{-12} \text{ m}^2$, pouring temperature = 620 - 630 °C and molten metal weight = 221 g). The pouring temperature and mold permeability coefficient of this aluminium foam production were significantly lower than those shown in **Figure 4.14** and hence type II structure aluminium foam can be obtained as shown in **Figure 4.18** including percentage of each infiltration zone of the produced aluminium foams. The low molten metal temperature and mold permeability coefficient resulted in complete solidification of molten metal prior to infiltrate through mold bases but molten metal was liquid enough to infiltrate space within spherical preforms. The degree of infiltrate was, however, slightly different with variation of initial vacuum pressure. Residue and retained metals were found to decrease and increase with increasing initial vacuum pressure (higher minus values), respectively, as shown in **Figure 4.18**. Higher initial vacuum pressure means more metal can infiltrate into space within the preforms and hence results in less residue metal. This expectation is consistent with saturation and density analysis as shown in **Figure 4.19**. Replacing measured saturation with other parameters⁴, S is expected to be 0.45 – 0.85.

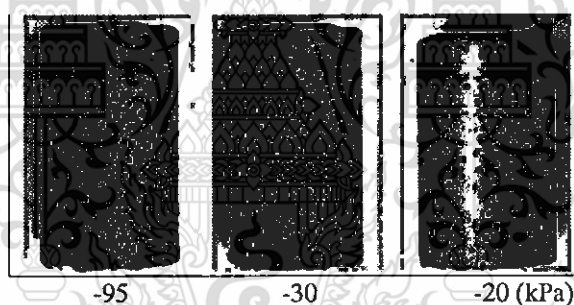


Figure 4.17 Photographs of 6.3 mm pore size aluminium foams produced using different initial vacuum pressures (mold permeability coefficient, pouring temperatures and molten metal weight were kept constant as $31.26 \times 10^{-12} \text{ m}^2$, 620 - 630 °C and 221 g, respectively).

⁴ Substituting S (measured saturation) = 0.89, 0.74 and 0.67, P = -95, -30 and -20 kPa respectively in Equation (2.24) with $P_b = -0.46 \text{ kPa}$ (Calculated in Figure 4.16) gives $\lambda = 0.71$ (which is the slope of curve fitted between $\ln(1 - S)$ in y-axis and $[\ln P_b - \ln P]$ in x-axis). Replacing $\lambda = 0.71$, $P_b = -0.46 \text{ kPa}$ and $P = -100 - (-10) \text{ kPa}$ gives S (predicted saturation) = 0.45 – 0.85.

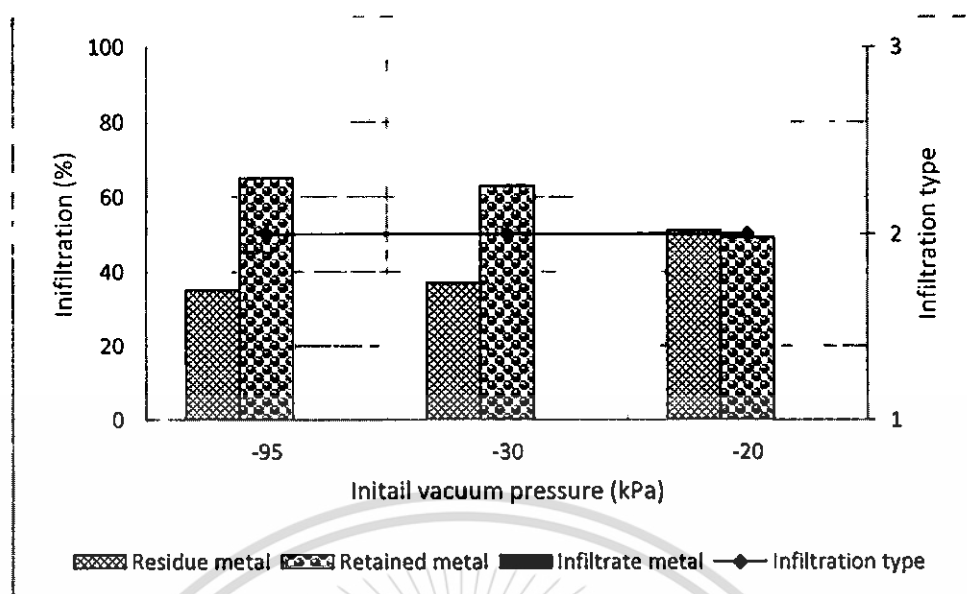


Figure 4.18 Infiltration characteristic of 6.3 mm pore size aluminium foams produced using different initial vacuum pressures (mold permeability coefficient, pouring temperature and molten metal weight were kept constant as $31.26 \times 10^{-12} \text{ m}^2$, 620 – 630 °C and 221 g, respectively).

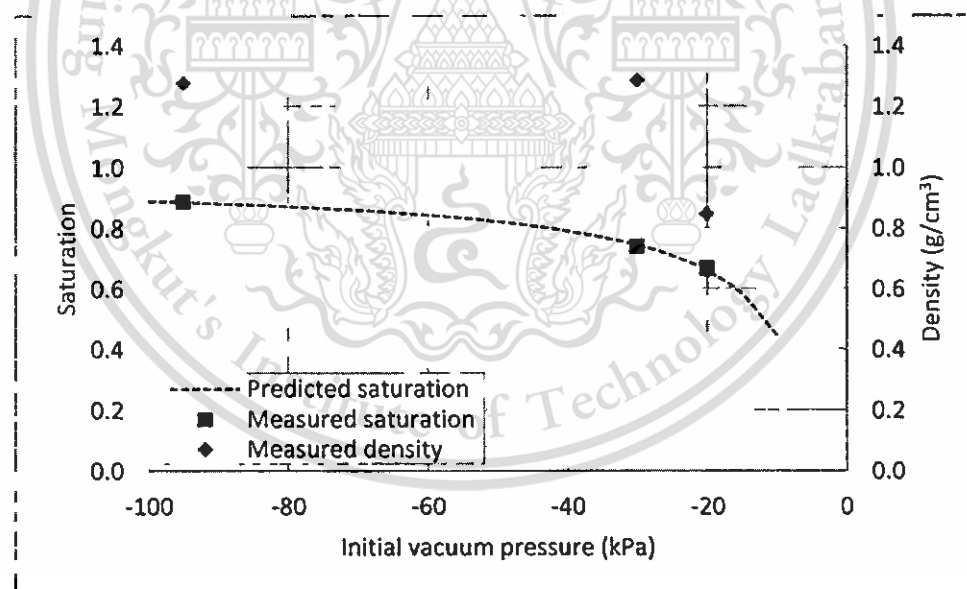


Figure 4.19 Predicted and measured saturation of 6.3 mm pore size aluminium foams produced using different initial vacuum pressures (mold permeability coefficient, pouring temperatures and molten metal weight were kept constant as $31.26 \times 10^{-12} \text{ m}^2$, 620 - 630 °C and 221 g, respectively).

4.1.2.3 High Mold Permeability Associating with Low Pouring Temperature

This material is reserved for educational use only, not allowed for commercial use.

Forbidden to modify the content, and cite the document when use.

For type III aluminium foam structure, density can be varied by varying initial vacuum pressure, as shown for example in **Figure 4.20** for 6.3 mm pore size aluminium foams produced using different initial vacuum pressures, while, other production parameters were kept constant (mold permeability coefficient = $44.35 \times 10^{-12} \text{ m}^2$, pouring temperature = $620 \text{ }^\circ\text{C}$ and molten metal weight = 276 g). Infiltration characteristics of these aluminium foams were shown in **Figure 4.21**. From this figure, retained and infiltrate metals were found to decrease and increase, respectively, with increasing initial vacuum pressure (higher minus values). The trend of the change of retained metal with initial vacuum pressure was in opposite with that found in type II aluminium foam structure as illustrated in **Figure 4.18**. However, similar explanation can be applied. Higher initial vacuum pressure means more metal can infiltrate into space within the preforms and due to the high permeability of the mold, more metal infiltrated through mold bases as well. As a result of this, less retained metal was obtained with increasing initial vacuum pressure (higher minus values). These features accorded with the saturation and density results as shown in **Figure 4.22**. Replacing measured saturation with other parameters⁵, S is expected to be 0.45 – 0.85.

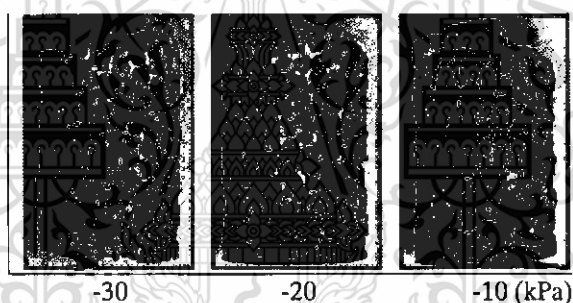


Figure 4.20 Photographs of 6.3 mm pore size aluminium foams produced using different initial vacuum pressures (mold permeability coefficient, pouring temperature and molten metal weight were kept constant as $44.35 \times 10^{-12} \text{ m}^2$, $620 \text{ }^\circ\text{C}$ and 276 g, respectively).

⁵ Substituting S (measured saturation) = 0.12, 0.17 and 0.25, $P = -30, -20$ and -10 kPa respectively in Equation (2.24) with $P_b = -0.46 \text{ kPa}$ (Calculated in Figure 4.16) gives $\lambda = -0.14$ (which is slope from fitted curve between $\ln(1 - S)$ in y-axis and $[\ln P_b - \ln P]$ in x-axis). Replacing $\lambda = -0.14$, $P_b = -0.46 \text{ kPa}$ and $P = -100 - (-10) \text{ kPa}$ gives S (predicted saturation) = 0.05 – 0.25.

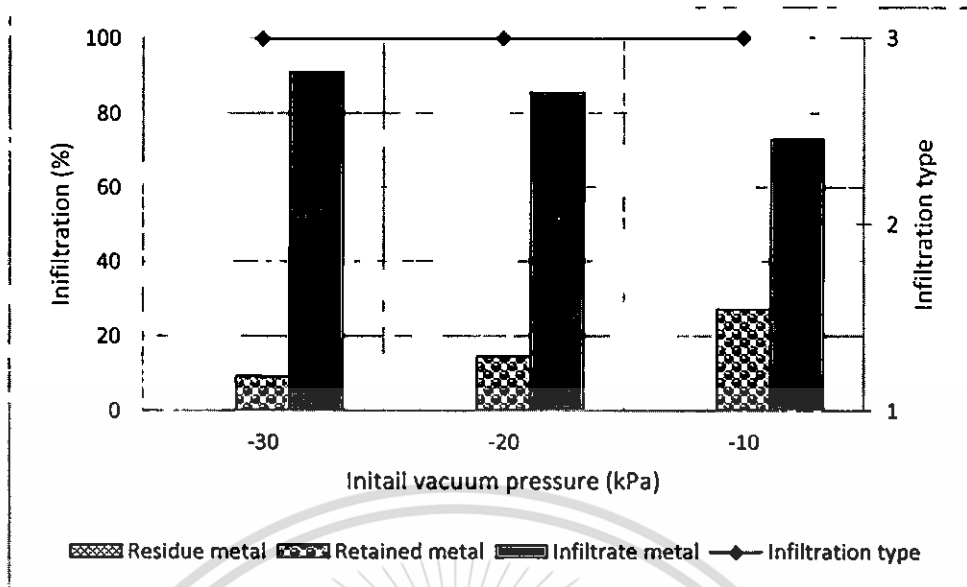


Figure 4.21 Infiltration characteristic of 6.3 mm pore size aluminium foams produced using different initial vacuum pressures (mold permeability coefficient, pouring temperature and molten metal weight were kept constant as $44.35 \times 10^{-12} \text{ m}^2$, $620 \text{ }^\circ\text{C}$ and 276 g , respectively).

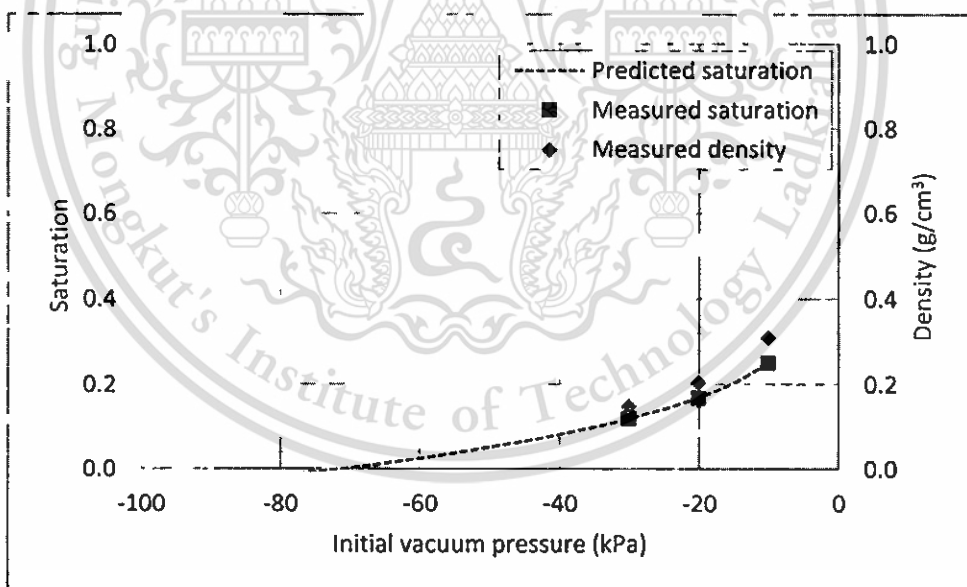


Figure 4.22 Predicted and measured saturation of 6.3 mm pore size aluminium foams produced using different initial vacuum pressures (mold permeability coefficient, pouring temperature and molten metal weight were kept constant as $44.35 \times 10^{-12} \text{ m}^2$, $620 \text{ }^\circ\text{C}$ and 276 g , respectively).

4.1.3 Effect of Melt Temperature

This material is reserved for educational use only, not allowed for commercial use.

Forbidden to modify the content, and cite the document when use.

4.1.3.1 High Mold Permeability

Figure 4.23 shows photographs of 6.3 mm pore size aluminium foams produced using different pouring temperatures, while other production parameters were kept constant (mold permeability coefficient = $44.35 \times 10^{-12} \text{ m}^2$, initial vacuum pressure = -100 kPa and molten metal weight = 334 g). Infiltration characteristics of these aluminium foams are shown in Figure 4.24. It can be seen that increasing pouring temperature resulted in increasing infiltrate metal and decreasing retained metal of the produced aluminium foams whose structure was all classified as type III, as shown in Figure 4.24.

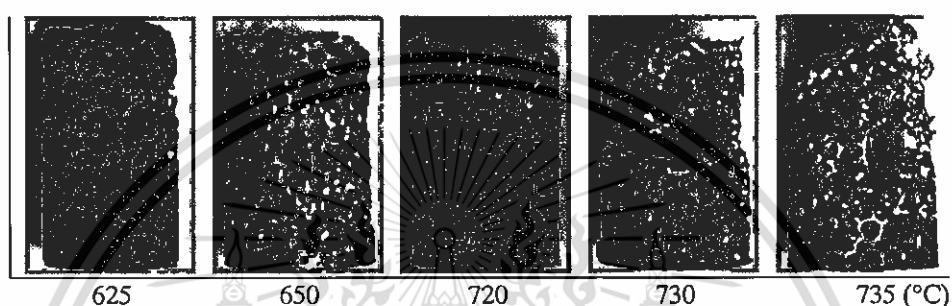


Figure 4.23 Photographs of 6.3 mm pore size aluminium foams produced using different pouring temperatures (mold permeability coefficient, initial vacuum pressure and molten metal weight were kept constant as $44.35 \times 10^{-12} \text{ m}^2$, -100 kPa and 334 g, respectively).

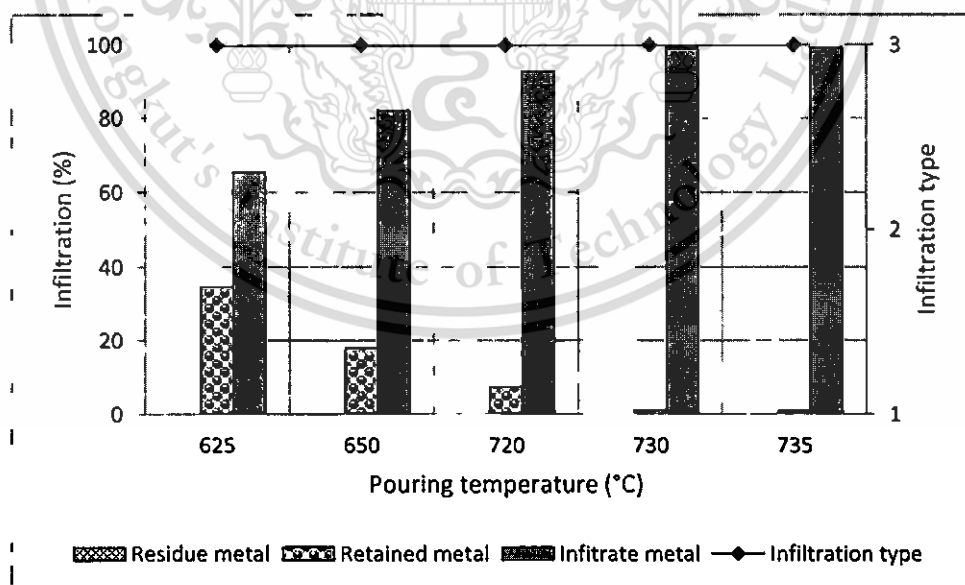


Figure 4.24 Infiltration characteristic of 6.3 mm pore size aluminium foams produced using different pouring temperatures (mold permeability coefficient, initial vacuum pressure and molten metal weight were kept constant as $44.35 \times 10^{-12} \text{ m}^2$, -100 kPa and 334 g, respectively).

Figure 4.25 shows results of saturation and bulk density versus pouring temperature of the aluminium foams shown in **Figure 4.23**. Saturation and bulk density of the produced aluminium foams were found to decrease with increasing pouring temperature. Molten metal with higher temperatures undoubtedly contained more fluidity and more heat to be extracted prior to solidify and hence the aluminium foams produced with higher pouring temperatures contained less retained metal as shown in **Figure 4.24** and less saturation as shown in **Figure 4.25**.

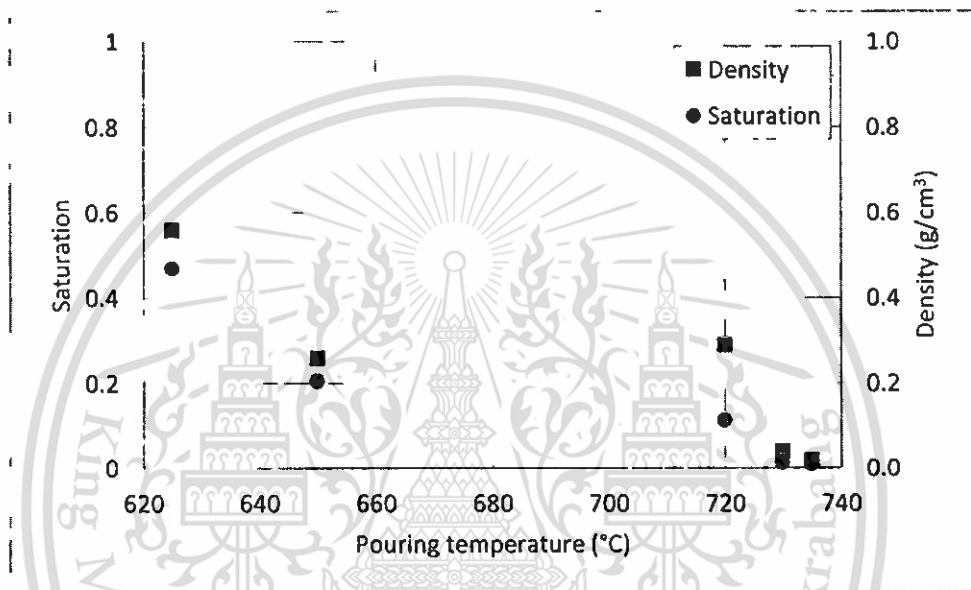


Figure 4.25 Density and saturation of 6.3 mm pore size aluminium foams produced using different pouring temperatures (mold permeability coefficient, initial vacuum pressure and molten metal weight were kept constant as $44.35 \times 10^{-12} \text{ m}^2$, -100 kPa and 334 g, respectively).

4.1.3.2 Low Mold Permeability

Varying pouring temperature, provided molds with low permeability were employed, was found to provide aluminium foams with type II for low pouring temperature and type III for higher pouring temperatures as shown in **Figure 4.26** and **Figure 4.27**. The saturation of the low pouring temperature of 630°C was highest comparing with other pouring temperature as shown in **Figure 4.28**. This is because molten metal completely solidified prior to infiltrate through mold base and hence large amount of metal retained in the space of preforms. Higher pouring temperatures resulted in more metal to infiltrate and hence less metal retained in the space of the preforms. Too high pouring temperature, such as 690°C, therefore left retained metal in-connected. It is interested to note that large incomplete structure can occur in some pouring temperature. If pouring temperature is high enough to allow some molten metal to infiltrate through

mold base but low enough to have remained molten metal to solidify prior to fulfill the preform space which has been left empty by infiltrate metal, such incomplete foam structure defect will occur, such as the pouring temperature of 660°C of this work.

Figure 4.29 shows density and saturation of aluminium foams produced by three schemes of productions—varying mold permeability $0 - 44.35 \text{ K} \cdot 10^{-12} \text{ m}^2$, initial vacuum pressure $-100 - 0 \text{ kPa}$ and pouring temperature $625 - 730^\circ\text{C}$. The productions gave a wide range of saturation of $0.01 - 0.93$ and hence resulted in aluminium foams with a wide range of density of $0.02 - 1.69 \text{ g/cm}^3$. It was found that the degree of saturation is fitted quite well with a directly proportional function with aluminium foam density.

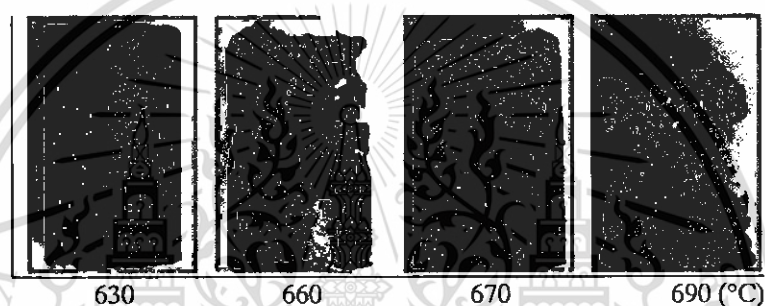


Figure 4.26 Photographs of 6.3 mm pore size aluminium foams produced using different pouring temperatures (mold permeability coefficient, initial vacuum pressure and molten metal weight were kept constant as $31.26 \times 10^{-12} \text{ m}^2$, -95 kPa and 267 g , respectively).

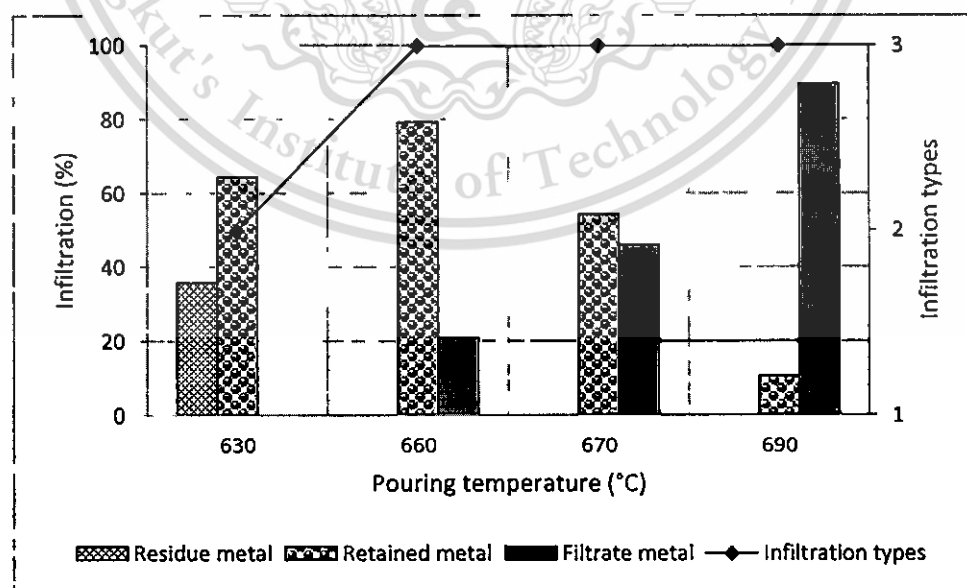


Figure 4.27 Infiltration characteristic of 6.3 mm pore size aluminium foams produced using different pouring temperatures (mold permeability coefficient, initial vacuum

This material is reserved for educational use only, not allowed for commercial use.

Forbidden to modify the content, and cite the document when use.

pressure and molten metal weight were kept constant as $31.26 \times 10^{-12} \text{ m}^2$, -95 kPa and 267 g, respectively).

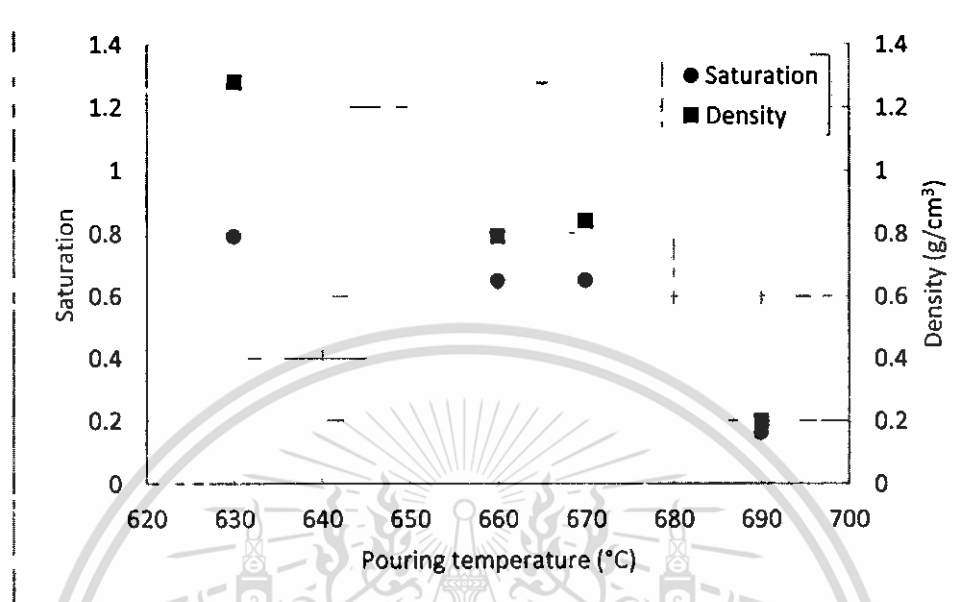


Figure 4.28 Saturation and density of 6.3 mm pore size aluminium foams produced using different pouring temperatures (mold permeability coefficient, initial vacuum pressure and molten metal weight were kept constant as $31.26 \times 10^{-12} \text{ m}^2$, -95 kPa and 267 g, respectively).

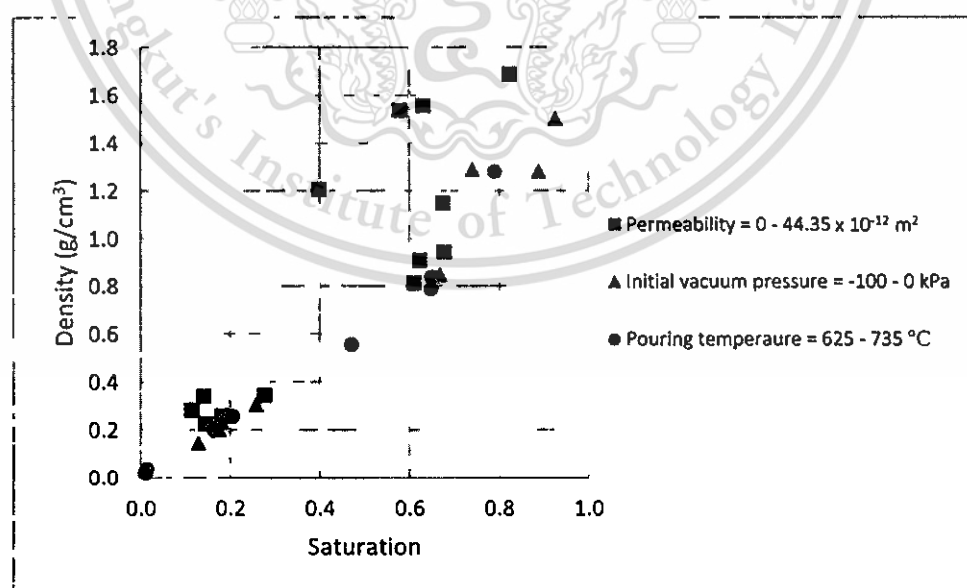


Figure 4.29 Saturation and density of 6.3 mm pore size aluminium foams produced using different conditions.

4.2 Structure of Aluminium Foams

Aluminium foams produced by space holder method in this work contained three main structures: incomplete, dense and spongy, as shown in **Figure 4.30**. These three structures are obtained by controlling infiltration behaviour of molten metal as best described by a schematic shown in **Figure 4.4**. Details of specific parameters of production to give such particular structures have been given in the previous section. This section will give details of spongy and dense structure of aluminium foams in terms of uniformity. Aperture which is a window hole connecting between pores of dense open cell foam will also described.

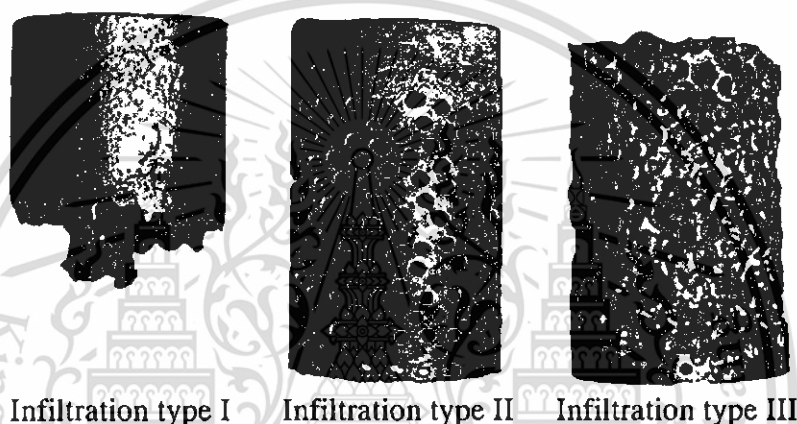


Figure 4.30 Photographs of infiltrated aluminium foams having different infiltration type (type I: mold drainage type H2, pouring temperature 725 °C and initial vacuum pressure 0 kPa, type II: mold drainage type M3, pouring temperature 675 °C and initial vacuum pressure -95 kPa, and type III: mold drainage type H2, pouring temperature 650 °C and initial vacuum pressure -100 kPa).

4.2.1 Uniformity of Structure

Figure 4.31 - Figure 4.32 show, for example, photographs of cross section along the length of aluminium foams produced with spherical preforms of mean diameter 4.1 mm and having dense and spongy structure, respectively. It can be observed that structure of dense aluminium foams was more uniform than that of spongy aluminium foams. This tendency was also applied for aluminium foams produced with spherical preforms of other sizes as shown by density along the length of the aluminum foams in **Figure 4.33**. A general decreasing tendency of density of aluminium foams with increasing height towards the opposite direction of infiltration was observed for both foam structures and for all spherical preform sizes. **Figure 4.34** shows porosities at positions each of ten mm interval from foam bottom of all foam structures. Since porosity is inversely propositional relation to density. An opposite trend of porosity change with foam locations was found for dense aluminium foams particularly for foams produced

This material is reserved for educational use only, not allowed for commercial use.

Forbidden to modify the content, and cite the document when use.

with higher preform sizes. Based on this image analysis for porosity at sections, there was no obvious tendency between porosity and positions of spongy aluminium foams. However, x-ray photographing methods showed the existing of more metal at bottom of a spongy aluminium foam as shown in **Figure 4.35**. The difference of porosity results obtained by 2-D image analysis method and 3-D x-ray based methods could be possible if dense metal located at positions less than 10 mm. For combination of density results obtained by weight-volume calculation and porosity results obtained by 2-D and 3-D imaging methods, both dense and spongy aluminium foams seem to contain higher density (lower porosity) at bottom and lower density (higher porosity) at top of the foams. This structure variation could not inevitable for infiltration production method since molten metal flow through mold bases until solidification or no assisted different pressure. More retained metal therefore presented in the opposite direction of infiltration. In addition, more variation in density was found in spongy aluminium foams and in aluminium foams produced using larger preform sizes.

Basically, uniformity of final produced metal foams will depend on how the foams are produced. The aluminium foams in this work were produced using space holder method and infiltration-based casting method. The uniformity of the final foams will therefore depend on how uniform metal to fill in space among preforms. However, initial pack of preforms is also equally important to final foam structure. **Figure 4.36** shows, for example, μ CT images of 6.3 mm spherical preforms after packing in a plaster mold using vibration for 60 s. Vibration was used to receive spherical preforms with random close packing which theoretically equals to 64% [85] Ref format?. Space, or in other words metal to fill, locates among the spherical preforms therefore occupies 36%. The maximum porosity of aluminium foams produced by space holder method using spherical preforms with random close packing should be 64%. Higher porosities can occur if metal does not fill space completely. The dense aluminium foams produced in this work contained porosities in the range 59 – 70% which are close to the theoretically random close packing of 64%. Any lower porosities at some locations within aluminium foams may come from either insufficient packing of preforms or high edge-to-volume effect. The latter reason may be the main contribution for the low porosities found at bottom of dense aluminium foams shown in **Figure 4.35**. High porosities in the range 83 – 93% of spongy aluminium foams were nicely obtained by this infiltration production method by leaving retained metal less than the theoretical space of random close packing of 36%. By controlling the degree of saturation under various production parameters, aluminium foams with different densities can be obtained. The degree of saturation was found to be almost directly proportional to the density of aluminium foams produced in this work as shown in **Figure 4.37**.

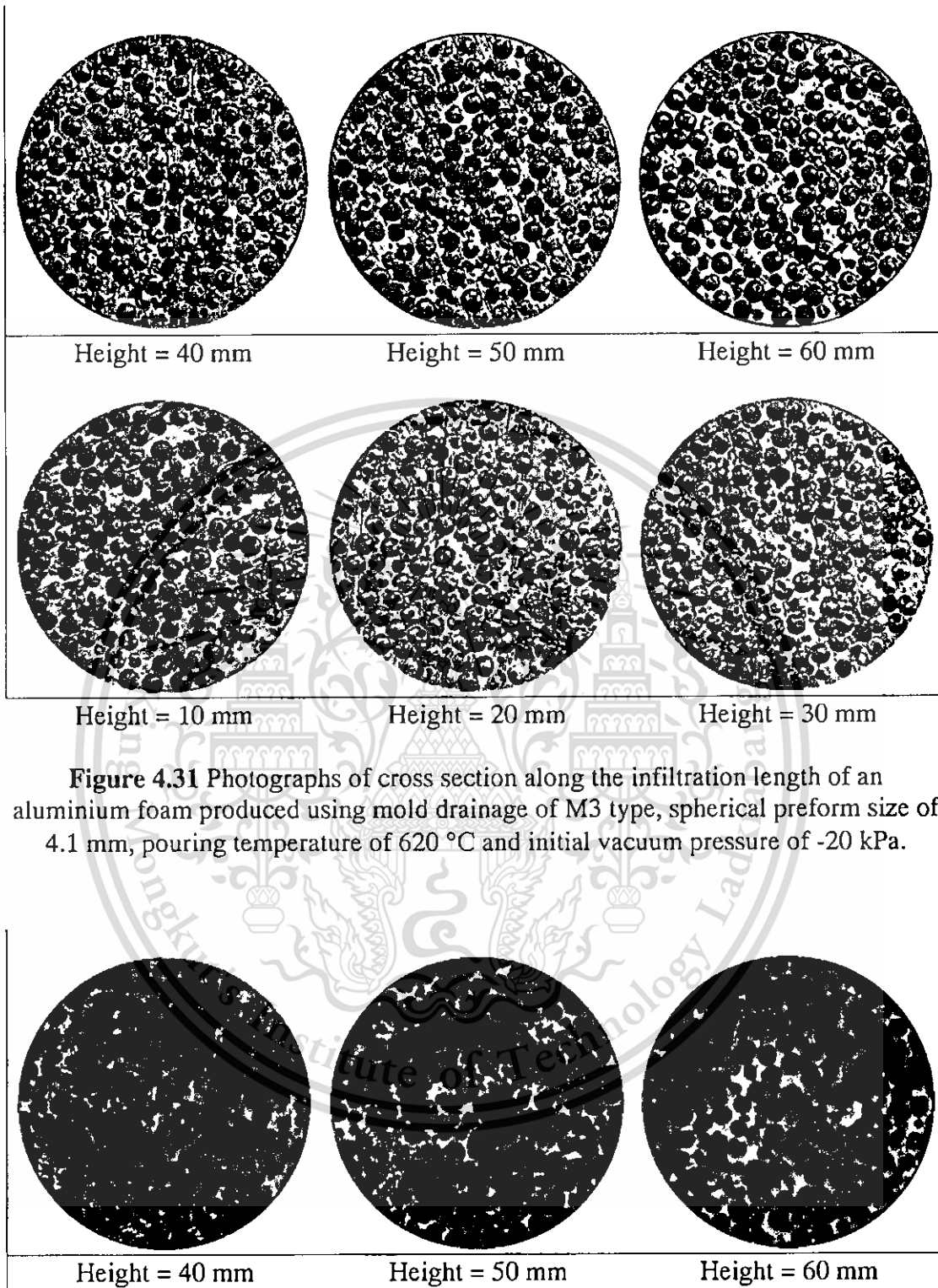
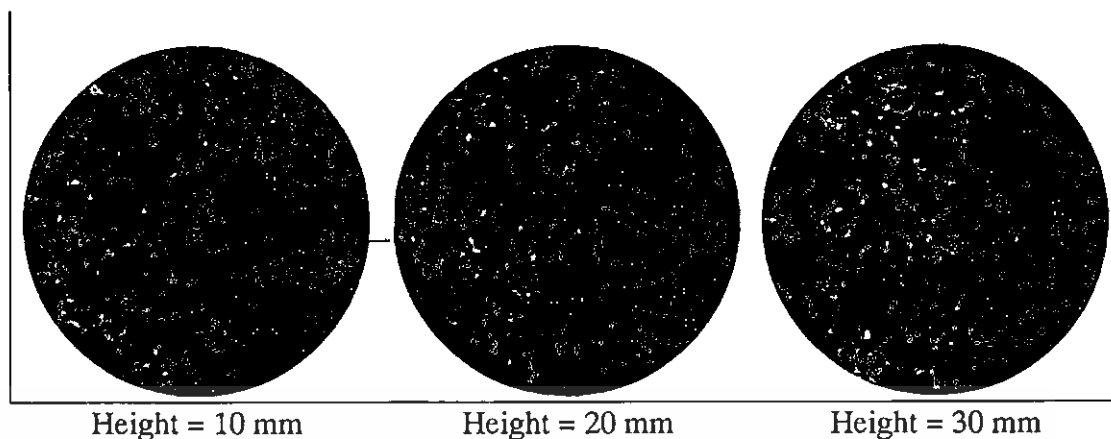


Figure 4.31 Photographs of cross section along the infiltration length of an aluminium foam produced using mold drainage of M3 type, spherical preform size of 4.1 mm, pouring temperature of 620 °C and initial vacuum pressure of -20 kPa.

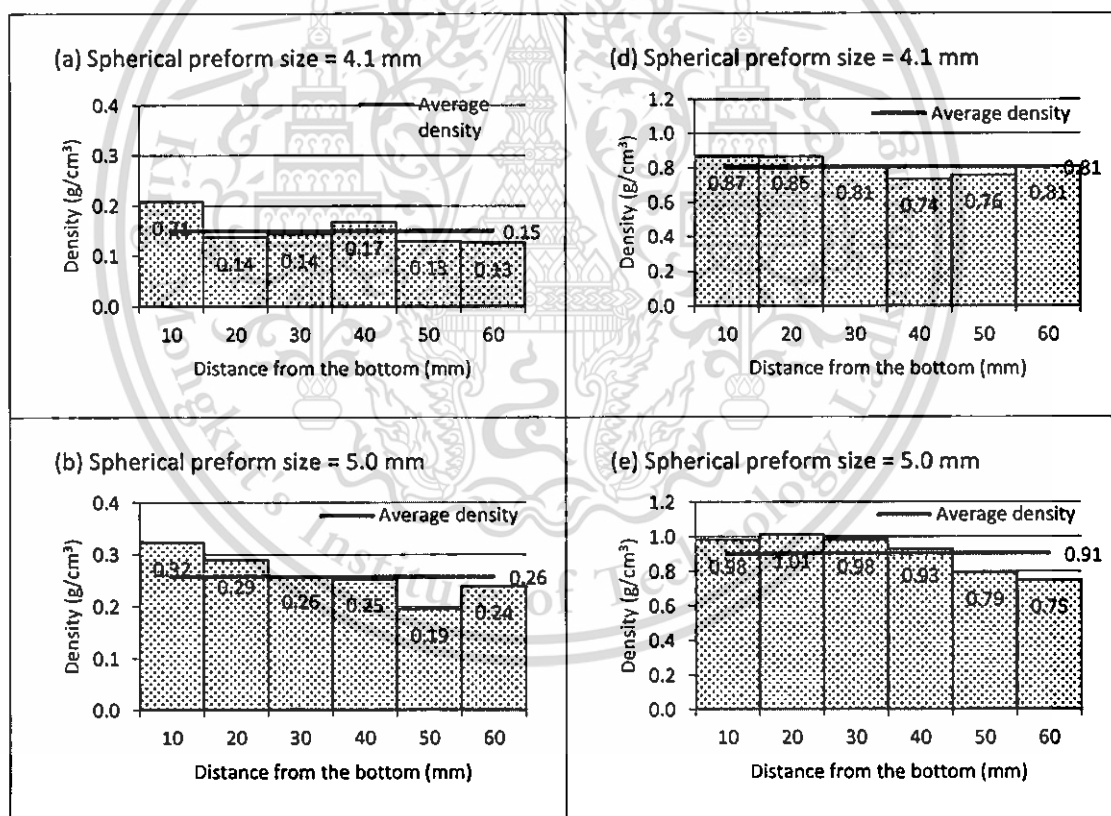


Height = 10 mm

Height = 20 mm

Height = 30 mm

Figure 4.32 Photographs of cross section along the infiltration length of an aluminium foam produced using mold drainage of H2 type, spherical preform size of 4.1 mm, pouring temperature of 620 °C and initial vacuum pressure of -20 kPa.



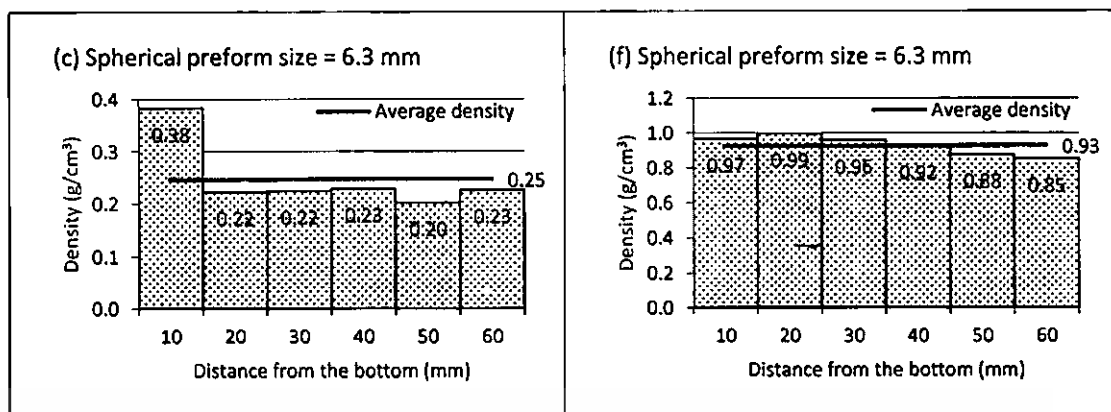
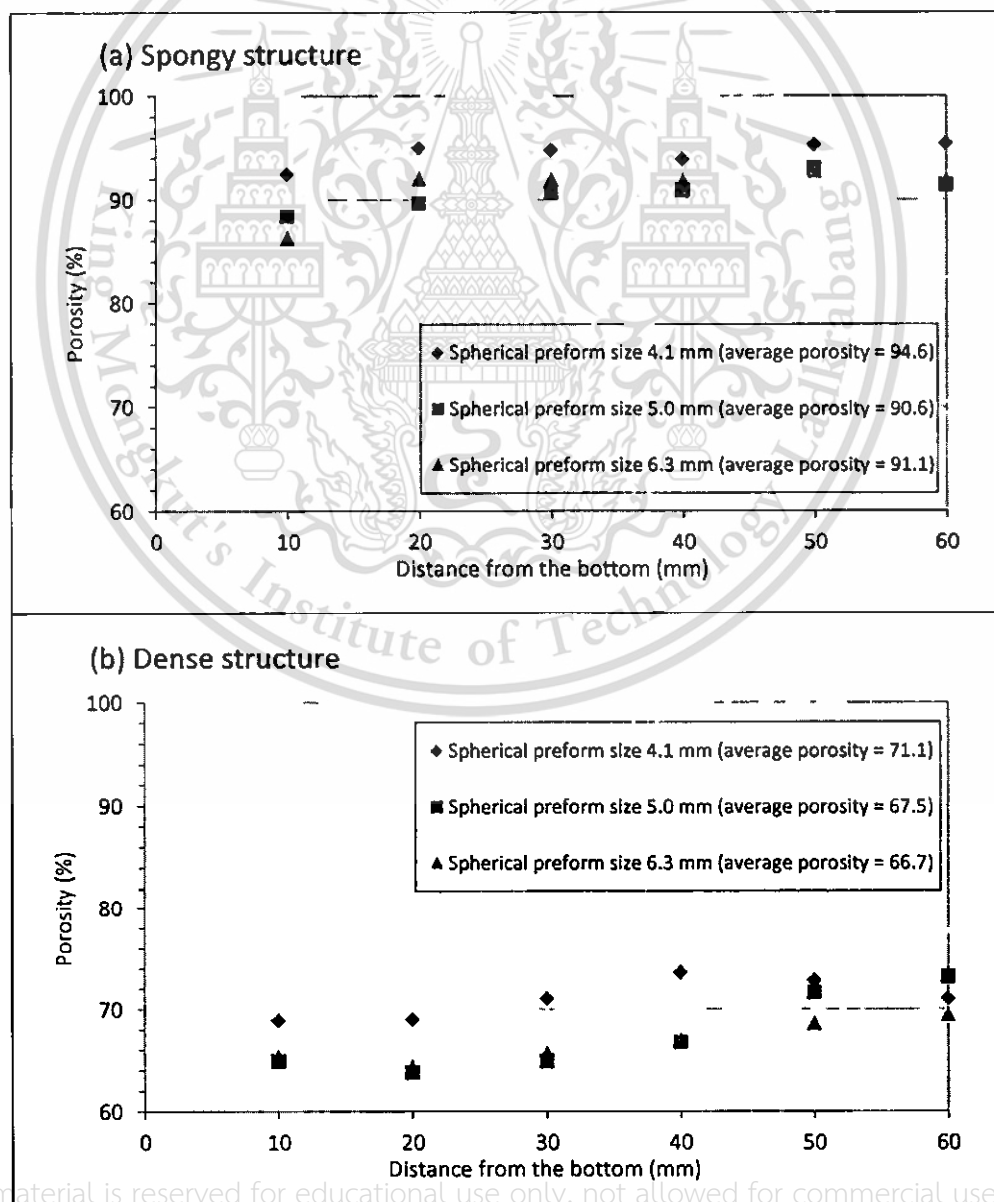


Figure 4.33 Density distribution of aluminium foams measured from bottom to top in vertical axis: (a) – (c) spongy and (e) – (f) dense structure of the foams produced using spherical preform sizes 4.1, 5.0 and 6.3 mm.



This material is reserved for educational use only, not allowed for commercial use.

Forbidden to modify the content, and cite the document when use.

Figure 4.34 Porosity distribution of aluminium foams measured from bottom to top in vertical axis: (a) spongy and (b) dense structure of the foams produced using spherical preform sizes 4.1, 5.0 and 6.3 mm.

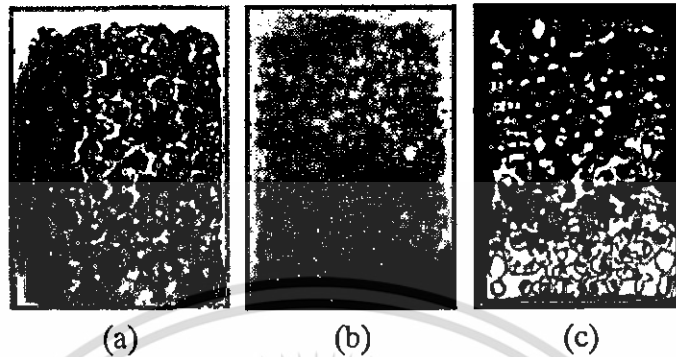


Figure 4.35 Spongy aluminium foam: (a) photograph, (b) x-ray and (c) CT-scan images.

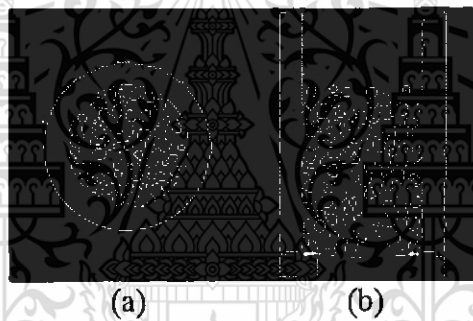
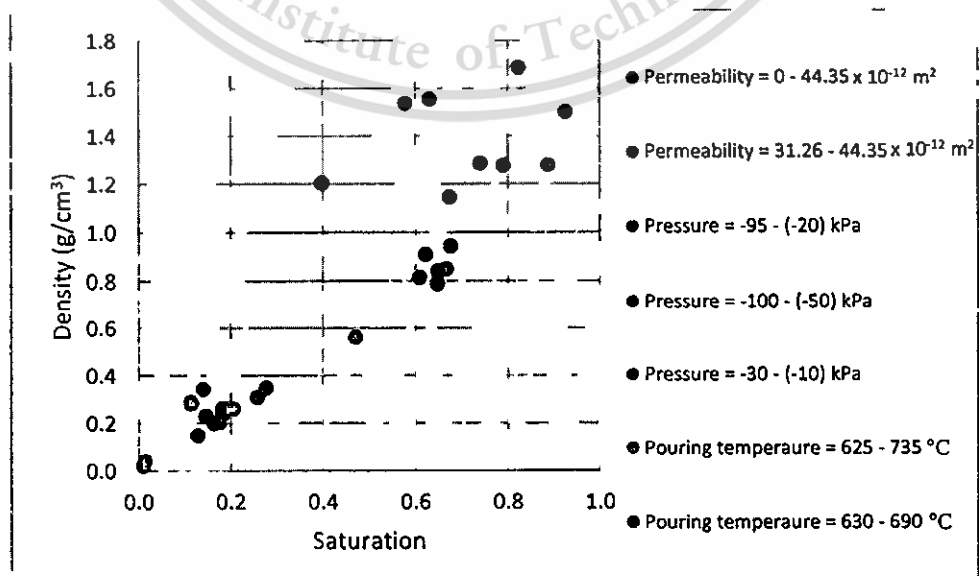


Figure 4.36 μ CT images of 6.3 mm spherical preforms after packing in plaster mold: vibrated time 60 s, weight 150 g: (a) top view and (b) front view.



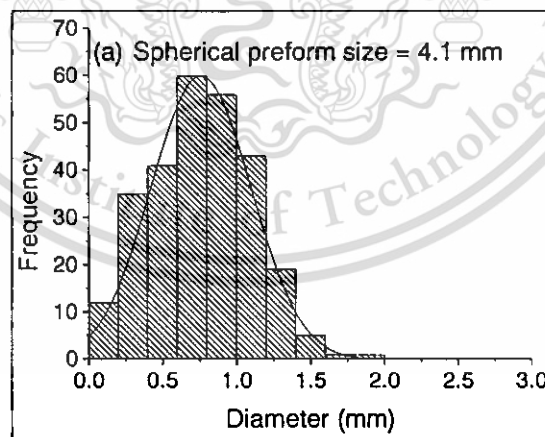
This material is reserved for educational use only, not allowed for commercial use.

Forbidden to modify the content, and cite the document when use.

Figure 4.37 Saturation and density of 6.3 mm pore size aluminium foams produced using different conditions.

4.2.2 Aperture Size

Aperture, which is contact areas between space holders (pore opening), is a unique character of dense metallic foams produced using space holder method. It is a structural parameter significantly influencing on sound absorption performance of aluminium foams as reviewed earlier in Section 2.7.1. In this section, aperture size of aluminium foams (produced using conditions given in **Table 4.3**) having dense structure with different pore sizes was reported. Image analysis technique represented in **Figure 3.9** was used for measuring aperture size. Results of aperture size distribution of the dense aluminium foams produced using spherical preform sizes 4.1, 5 and 6.3 mm are shown in **Figure 4.38** (a), (b) and (c) respectively. Their aperture size averages in terms of arithmetic mean of population are 0.76, 1.12 and 1.14 mm, respectively. The trend of the increase in aperture size average with increasing spherical preform size is understandable since the curvature of molten metal around spherical preforms between two preforms will be further away for large preform sizes. As a result, solidified metal at those disjointed area will appear as apertures having larger sizes for larger preforms. The trend of increasing aperture size with increasing spherical preform size was found in both measurement using image analysis method and predictions⁶ using Equations (2.25). However, all predicted aperture sizes are underestimated as shown in **Figure 4.39**. Discrepancies in measuring the size of apertures which appeared in different planes may result in the disagreement results.



⁶ Replacing $P = -20$ kPa, $\sigma = 0.945$ N/m, $\theta = 140$ degree, $R = 2.05, 2.5$ and 3.15 mm (for spherical preform size = 4.1, 5.0 and 6.3 mm respectively) in Equation (2.25).

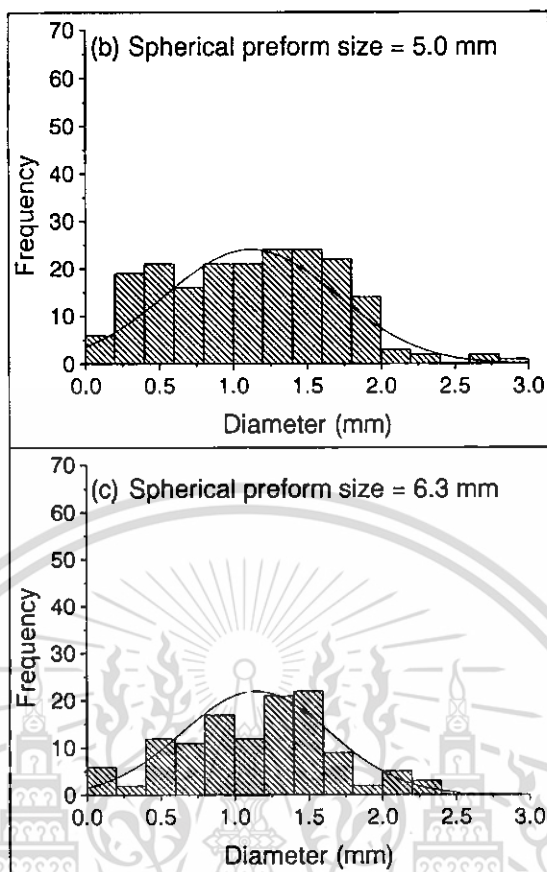


Figure 4.38 Size distribution of apertures of dense aluminium foams produced using infiltration method with conditions given in Table 4.3 for preform sizes: (a) 4.1, (b) 5 and (d) 6.3 mm.

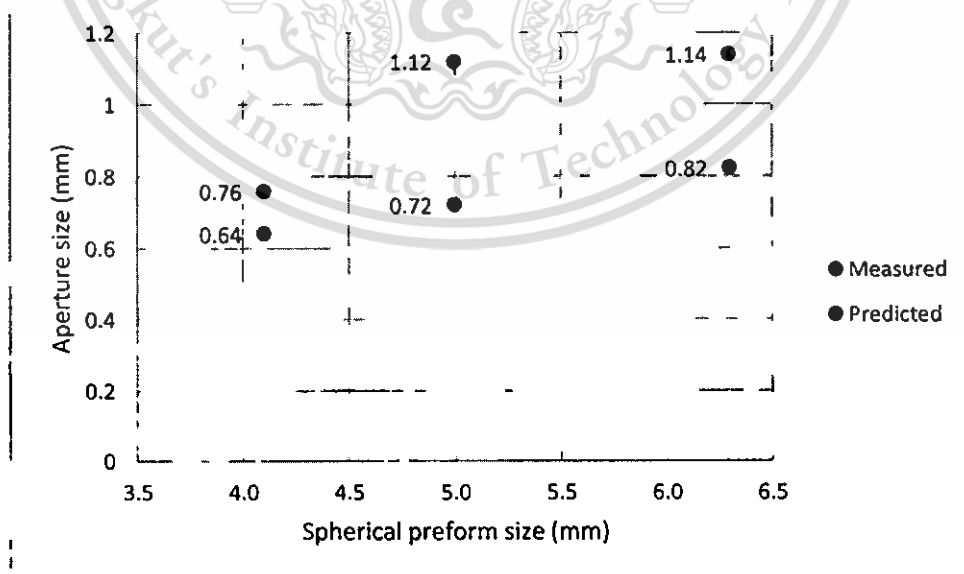


Figure 4.39 Predicted and measured apertures of dense aluminium foams produced using infiltration method with conditions given in Table 4.3 for preform sizes: (a) 4.1, (b) 5 and (d) 6.3 mm.

This material is reserved for educational use only, not allowed for commercial use.

Forbidden to modify the content, and cite the document when use.

4.3 Compressive test

Figure 4.40 - Figure 4.41 show stress-strain curves of compression test up to 80% strain of different pore size aluminium foams having dense (low porosity) and spongy (high porosity) structures, respectively. All aluminium foams exhibited foam characteristic in that long plateau stress regime presented. Dense aluminium foams were found about 60 to nearly 90 times stronger than spongy aluminium foams. Both dense and spongy foams produced with spherical preforms of larger sizes exhibited higher strength than those produced with spherical preforms of smaller sizes. However, there was no noticeable difference in strength among spongy foams produced with different preform sizes for compressive strains up to 40%. Aluminium foams produced with larger preform sizes contained thicker solid walls which should contribute to the higher strengths. It should be noted that the preforms of 4.1 mm mean spherical diameter gave detrimental effect on the compressive behaviour of dense aluminium foams. The reason of low strength of this aluminium foam may relate to the high number of defects, which can be clearly seen at external surface, of incomplete fill of this foam. Small channels of space between small preforms made them difficult to be completely filled by molten metal, and hence more incomplete fill defects were found in the aluminium foams produced with 4.1 mm preforms.

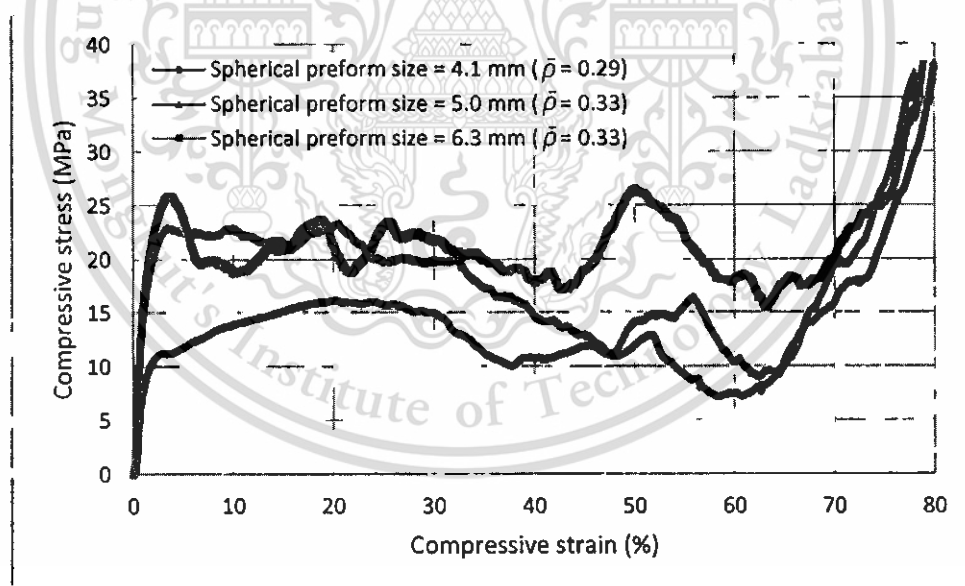


Figure 4.40 Compressive stress-strain curves of dense aluminium foams produced by preforms having mean spherical diameters 4.1, 5.0 and 6.3 mm and molds having permeability coefficient of $31.26 \times 10^{-12} \text{ m}^2$.

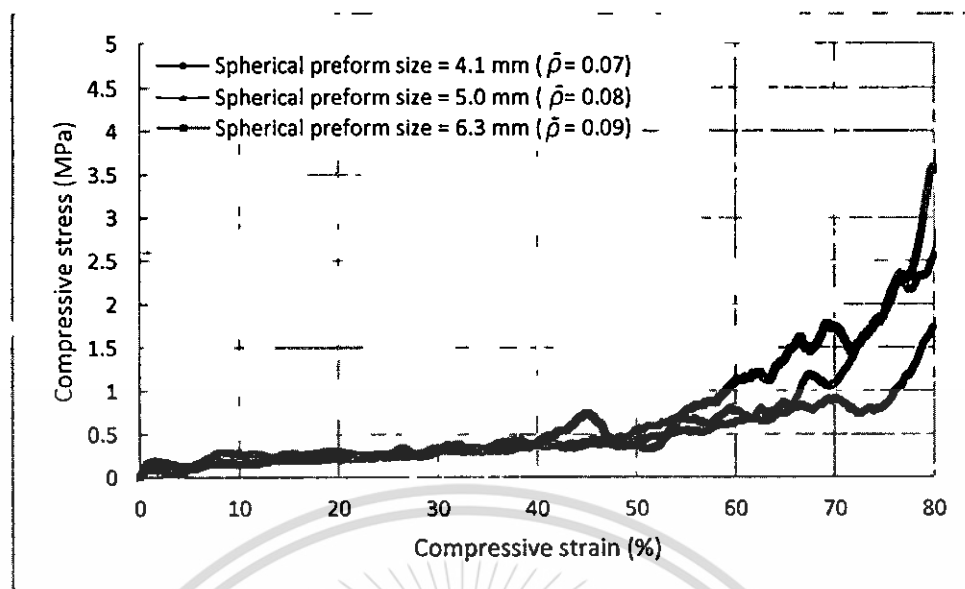


Figure 4.41 Compressive stress-strain curves of aluminium foams produced by preforms having mean spherical diameters 4.1, 5.0 and 6.3 mm and molds having permeability coefficient of $44.35 \times 10^{-12} \text{ m}^2$.

Aluminium foams with dense structure deformed in different way of that with spongy structure. **Figure 4.42** showed typical compressive behaviour of dense aluminium foams. The stress-strain plot can be clearly divided into three main parts. In the first part, aluminium foam deformed elastically and appeared without any harmful damage as shown in the first inset photograph of **Figure 4.42**. In the second part, plastic deformation was clearly seen and cracks appeared in the foam as can be seen in the second inset photograph of **Figure 4.42**. The cracks lined in particular rows of spherical pores. Sudden drops of load bearing came from major cracks within the foam. The fractures of foam walls during this deformation consumed large energy and strain. In the third part, required force to compress was ascending due to densification of the foam as shown in the third inset photograph of **Figure 4.42**. For spongy aluminium foams whose typical compressive curve is illustrated in **Figure 4.43**, even though there are three main parts of stress-strain similar to those found in dense aluminium foams, compressive behaviour appeared different in detail. In the first part, the spongy foam showed elastic deformation but with significant smaller yield stress and strain. The foam under this deformation exhibited no damage appearance as shown in the first inset photograph of **Figure 4.43**. In the second part, the spongy foam deformed plastically. Continuously ascending stress without any significant drop was found. Some line cracks were found in the spongy foam, as shown in the second inset photograph of **Figure 4.43**, however, there was no large piece of crack panels as found in the dense foam. At almost the end of plastic deformation, there was a noticeable drop of stress prior to sudden rise of stress at the third part of deformation due to densification of the spongy foam. The appearance of the spongy foam during the densification deformation is shown in the third inset photograph of **Figure 4.43**. Mechanical properties of

representative dense and spongy aluminium foams produced with different spherical preform sizes are summarised in parallel with their physical properties in **Table 4.5.**

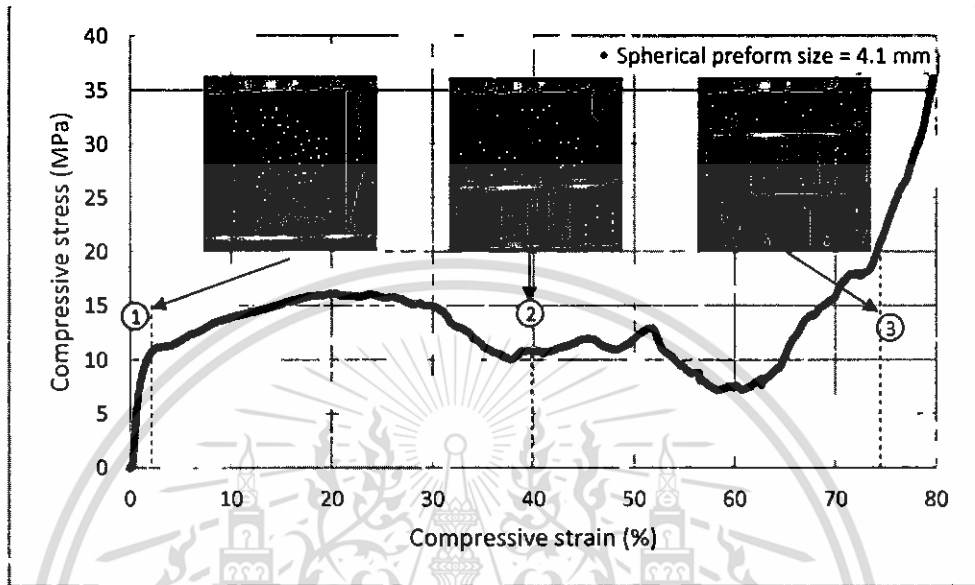


Figure 4.42 Compressive stress-strain curve of a dense aluminium foam produced by preforms having a mean spherical diameter of 4.1 mm and a mold having permeability coefficient of $31.26 \times 10^{-12} \text{ m}^2$ (Inset photographs showed the foam specimen at different strains during compression).

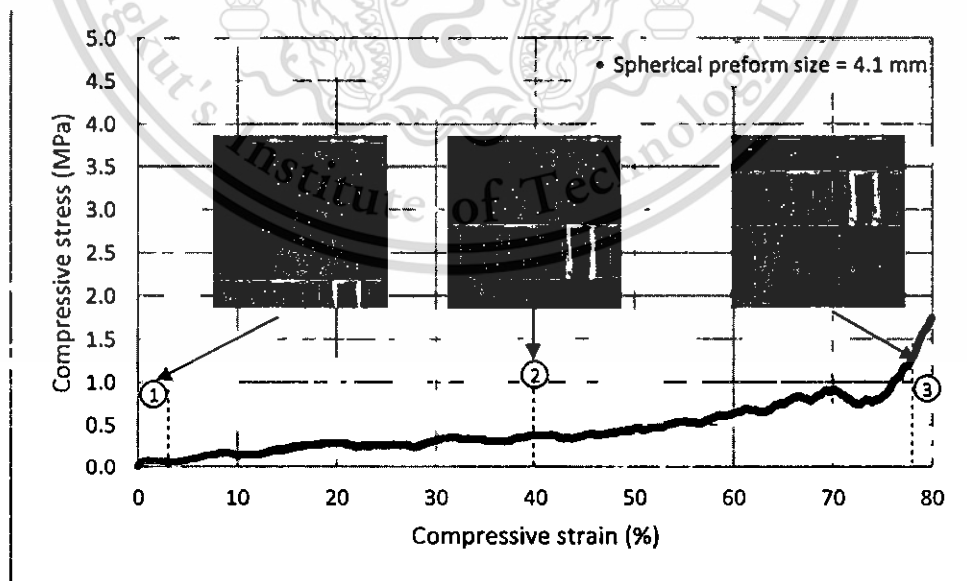


Figure 4.43 Compressive stress-strain curve of a spongy aluminium foam produced by preforms having a mean spherical diameter of 4.1 mm and a mold having permeability coefficient of $44.35 \times 10^{-12} \text{ m}^2$ (Inset photographs showed the foam specimen at different strains during compression).

Table 4.5 Physical and mechanical properties of produced aluminium foams.

Properties	Dense-4	Dense-5	Dense-6	Spongy-4	Spongy-5	Spongy-6
Physical properties :						
Foam diameter (mm)	53.37	53.50	53.56	53.40	53.14	53.23
Foam height (mm)	57.7	60.39	61.89	61.74	65.61	64.15
Spherical preform size (mm)	4.1	5.0	6.3	4.1	5.0	6.3
Porosity (%)	71	67	67	93	92	91
Relative density	0.31	0.35	0.35	0.08	0.08	0.10
Mechanical properties :						
Young's modulus (MPa)	1,060	1,704.3	1,914.3	20.1	36.9	12.2
Plateau stress (MPa)	11.51	22.84	25.23	0.26	0.24	0.26
Densification strain (%)	73.41	64.10	64.10	78.56	78.99	77.85
Energy absorption at densification ($\text{MJ}\cdot\text{m}^{-3}$)	9.15	11.28	13.21	0.34	0.45	0.51

Figure 4.44 and **Figure 4.45** show measured modulus, E and yield strength, σ_{pl} of different structure aluminium foams of this work plotted as a function of relative density. Experimental data were fitted using a scaling law for mechanical properties prediction. The empirical models of modulus and yield strength can be derived from experimental data giving relations $E = 0.7E_s\bar{\rho}^{3.09}$ and $\sigma_{pl} = 5.4\sigma_y\bar{\rho}^{3.14}$, respectively. The coefficients of the empirical models are within the range of recommended values, which are 0.1 – 4 for Young's modulus model of open cell foams and 0.1 – 1.0 for compressive strength model of open cell foams [19]. The power values, however, are beyond the recommended values, which are 2 for Young's modulus model of open cell foams and 1.5 for compressive strength model of open cell foams [19]. The particular hollow structure made from spherical preforms in this work may contribute to the different compression behaviour obtained from typical open cell foam structure. General scaling models are therefore recommended to be refined for individual structure of open cell foams. Even though there are some disagreements of mechanical properties against physical properties of the scaling laws of this work aluminium foams, plots of those properties of this work aluminium foams together with those of currently available metal foams are fit very well as shown in **Figure 4.46** - **Figure 4.48**. It can be observed from these figures that mechanical properties of spongy and dense aluminium foams of this work provide nearly lower and upper limits of those of currently available metal foams. Due to aluminium foams with other densities within the range between those of spongy and dense structure can be produced by production parameter variation, aluminium foams produced by spherical preforms in this work should provide the whole range of mechanical properties available by current metal foams in the market.

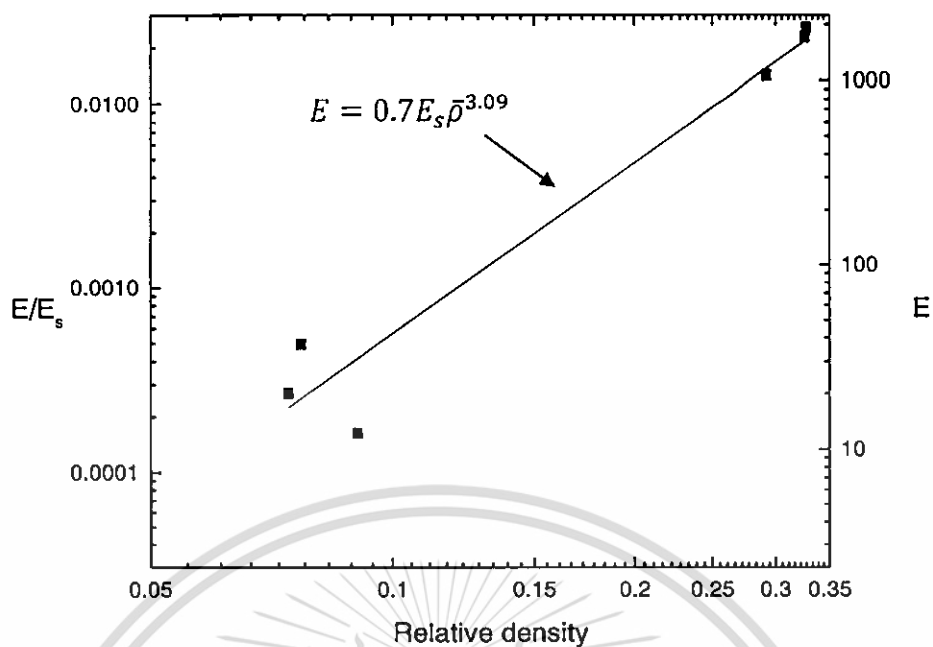


Figure 4.44 Plots of relative Young's modulus (and Young's modulus) against relative density of the produced aluminium foams shown in

Table 4.5.

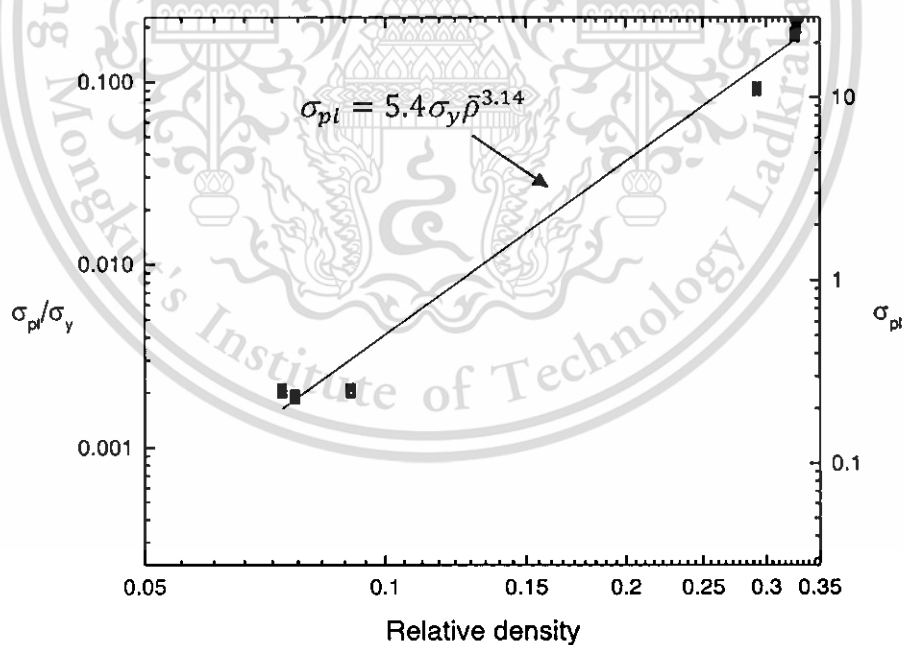


Figure 4.45 Plots of relative plateau stress (and plateau stress) against relative density of the produced aluminium foams shown in

Table 4.5.

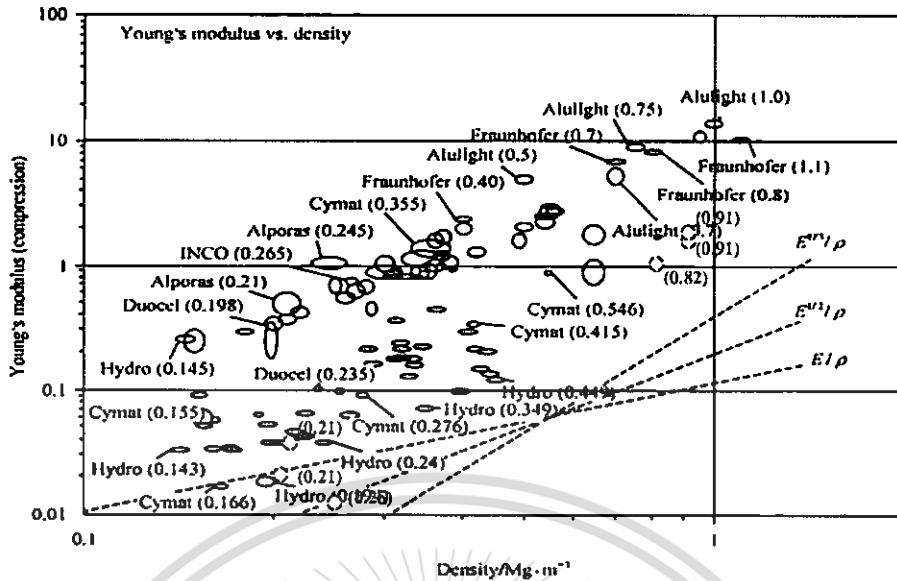


Figure 4.46 Plots of Young's modulus against density of currently-available metal foams [86] (Black symbols) and this work aluminium foams (Red symbols) shown in Table 4.5 (Numbers in parentheses are densities in Mg/m^3).

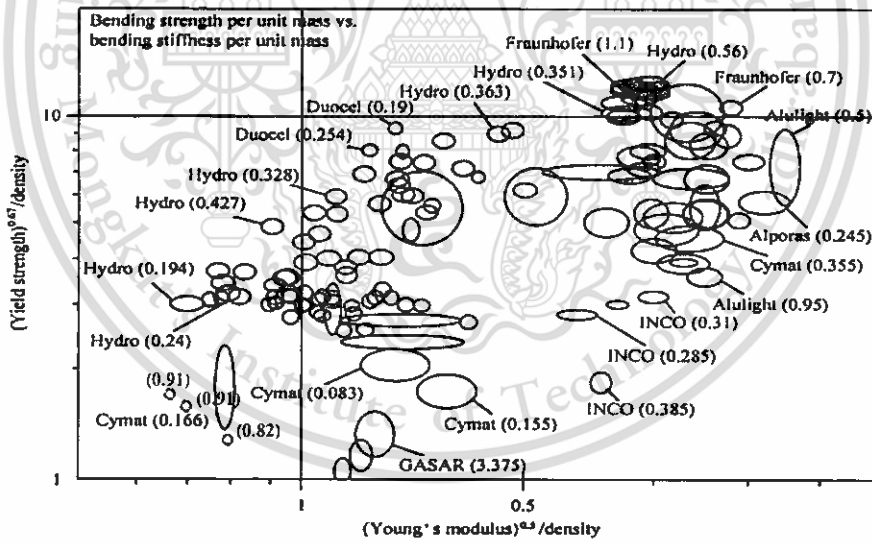


Figure 4.47 Plots of $\sigma_c^{2/3}/\rho$ against $E^{1/2}/\rho$ of currently-available metal foams [86] (Black symbols) and this work aluminium foams (Red symbols) shown in Table 4.5 (Numbers in parentheses are densities in Mg/m^3). $E^{1/2}/\rho\sigma_c^{2/3}/\rho$

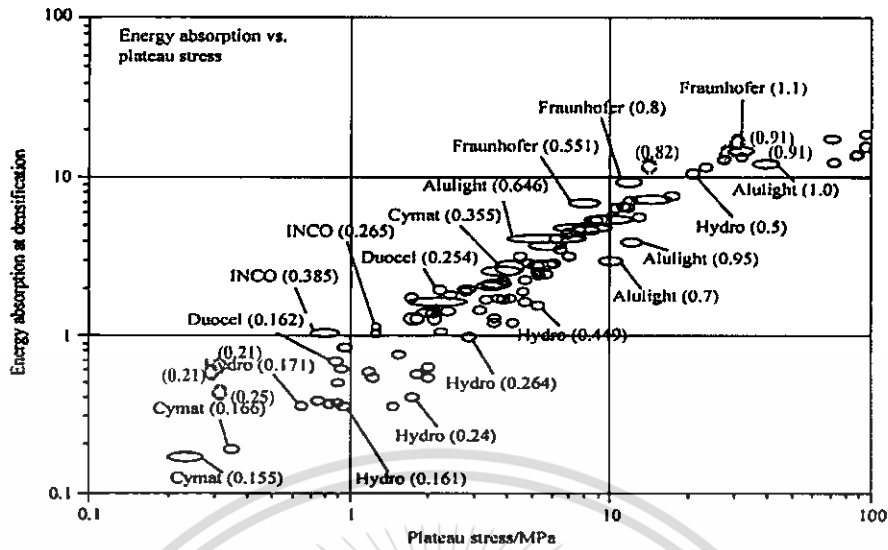


Figure 4.48 Plots of energy absorption at densification against plateau stress of currently-available metal foams [86] (Black symbols) and this work aluminium foams (Red symbols) shown in

Table 4.5 (Numbers in parentheses are densities in Mg/m^3).

4.4 Sound Absorption Test

Table 4.6 Properties of aluminium foams produced by infiltration method.

Sample	Unit cell (number)	Air gap (mm)	Thickness (mm)	Porosity (%)	Pore size (mm)	Aperture (mm)	P/Ap. (ratio)	Density (g/cm^3)
a	2	0, 10, 20, 30	8	70	4.1	0.76	5.39	0.86
b	6	0, 10, 20, 30	25	66	4.1	0.76	5.39	0.83
c	13	0, 10, 20, 30	56	73	4.1	0.76	5.39	0.83
d	26	0, 10, 20, 30	115	71	4.1	0.76	5.39	0.80
e	39	0, 10, 20, 30	173	71	4.1	0.76	5.39	0.80
f	51	0, 10, 20, 30	229	71	4.1	0.76	5.39	0.80
g	63	0	281	70	4.1	0.76	5.39	0.79
h	2	0	8	68	5.0	1.12	4.46	0.79
i	5	0	25	68	5.0	1.12	4.46	0.82
j	11	0	61	67	5.0	1.12	4.46	0.93
k	23	0	126	66	5.0	1.12	4.46	0.94
l	34	0	186	67	5.0	1.12	4.46	0.93
m	46	0	252	66	5.0	1.12	4.46	0.94

n	1	0	9	68	6.3	1.14	4.44	0.88
o	4	0	25	66	6.3	1.14	4.44	0.83
p	9	0	62	67	6.3	1.14	4.44	0.91
q	18	0	128	67	6.3	1.14	4.44	0.93
r	28	0	194	66	6.3	1.14	4.44	0.93
s	38	0	260	66	6.3	1.14	4.44	0.93

4.4.1 Effect of Structural Foam on Sound Absorption Performance

Sound absorption coefficient of aluminium foams with different pore size, porosity and thickness was measured using two-microphone impedance tube method at frequencies in the range 125-3150 Hz. **Figure 4.49** shows plots of sound absorption coefficient versus frequency of different pore size aluminium foam samples with the same thickness of 8 mm. Highest sound absorption coefficient was found at 1,600, 3,150 and 1,250 Hz for aluminium foams with pore size of 4, 5 and 6 mm, respectively.

Increasing sample thickness to 25 and 50 mm, the peak of sound absorption coefficient occurred at lower frequencies, i.e. 1000 and 500 Hz for 25 and 50 mm aluminium foams, respectively, as can be seen in **Figure 4.50** and **Figure 4.51** respectively. This tendency was also found by other investigators [50]. **Figure 4.52 - Figure 4.54** show the change of sound absorption performance of aluminium foams with different thicknesses and pore sizes. For the same foam thickness, the peak of sound absorption coefficient increased with reducing pore size.

Figure 4.55 - Figure 4.60 show the effect of porosity on sound absorption performance of spongy (high percentage porosity) and dense (low percentage porosity) aluminium foams. It can be seen that aluminium foams with low porosity performed better sound absorption than those with high porosity. In addition, for aluminium foams having the same porosity, thicker aluminium foams exhibited better sound absorption than thinner aluminium foams irrespective of pore size.

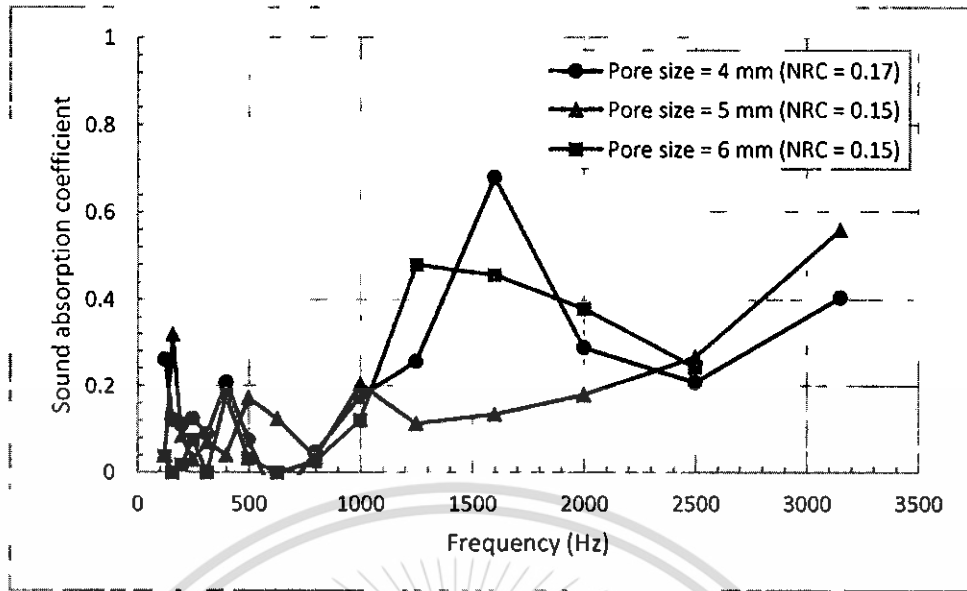


Figure 4.49 Effect of pore size on sound absorption of aluminium foams with sample thickness of 8 mm.

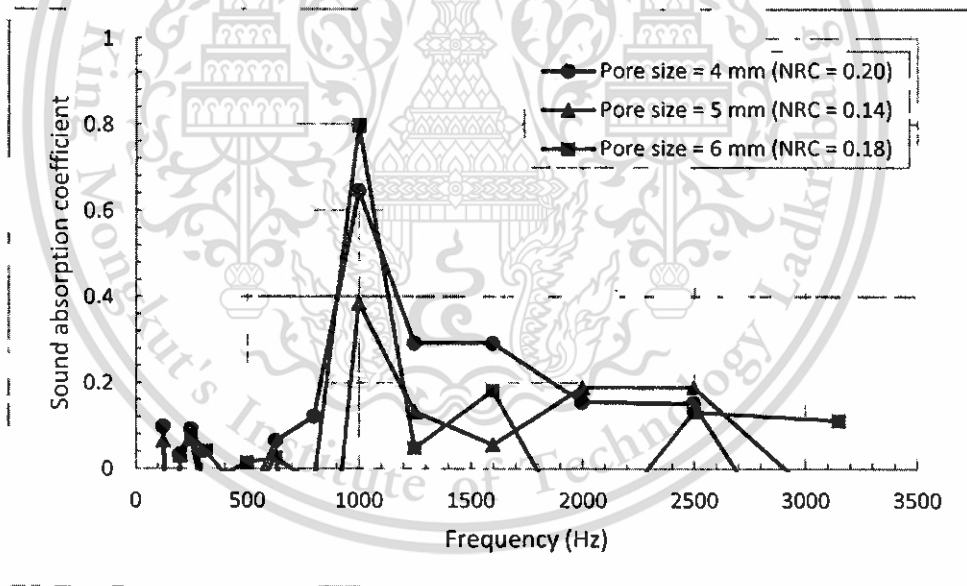


Figure 4.50 Effect of pore size on sound absorption of aluminium foams with sample thickness of 25 mm.

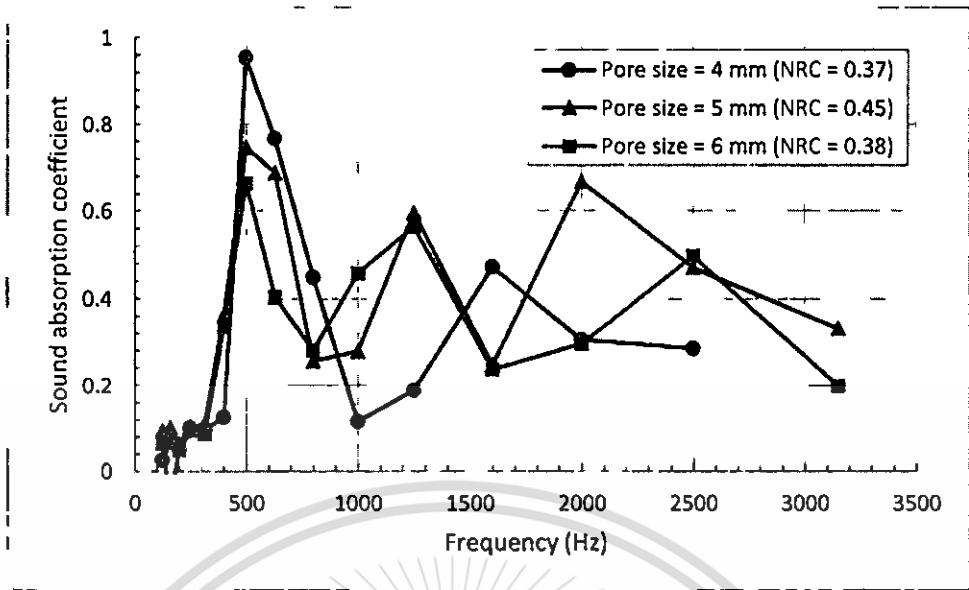


Figure 4.51 Effect of pore size on sound absorption of aluminium foams with sample thickness of 50 mm.

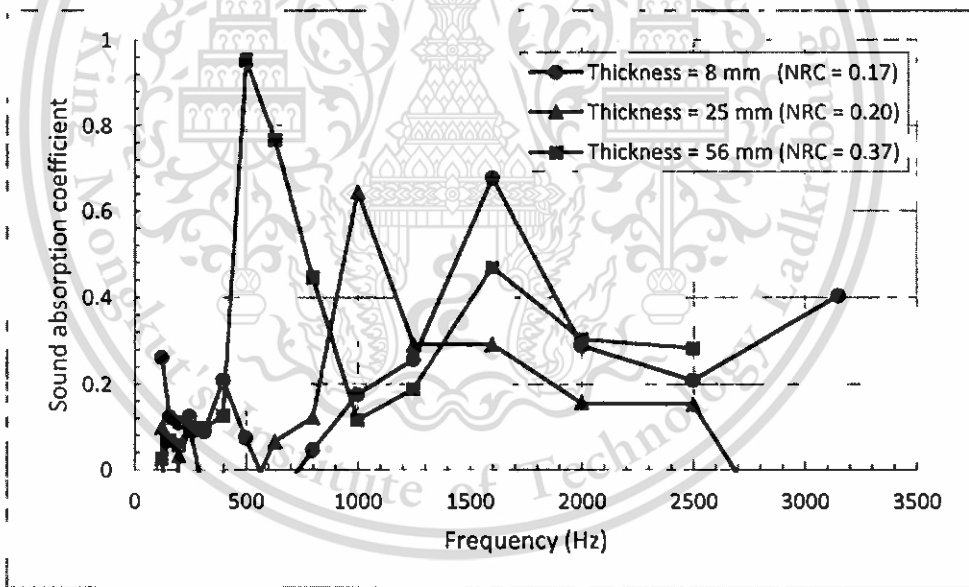


Figure 4.52 Effect of sample thickness on sound absorption coefficient of aluminium foams pore size 4.1 mm (no an air gap cavity).

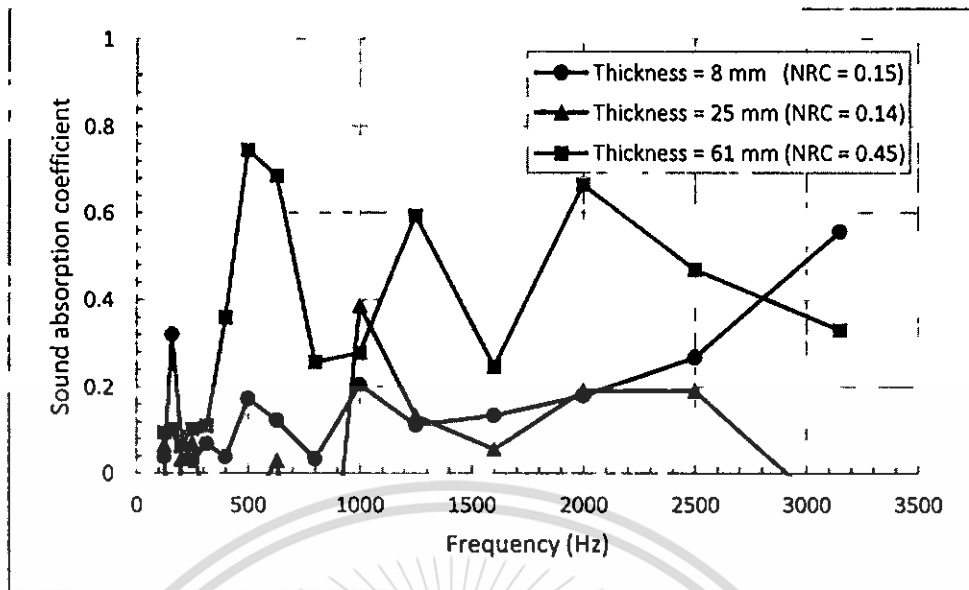


Figure 4.53 Effect of sample thickness on sound absorption coefficient of aluminium foams pore size 5 mm (no an air gap cavity).

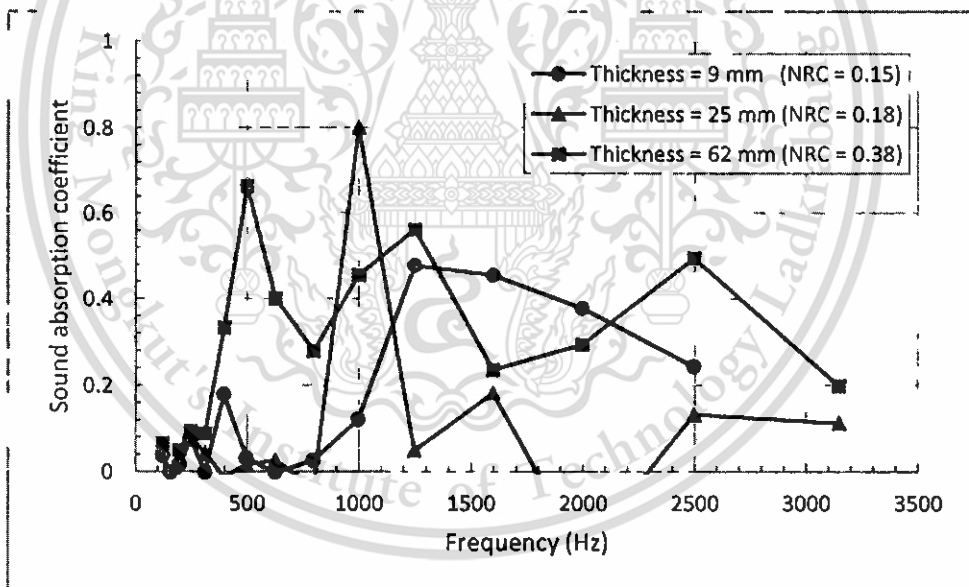


Figure 4.54 Effect of sample thickness on sound absorption coefficient of aluminium foams pore size 6.3 mm (no an air gap cavity).

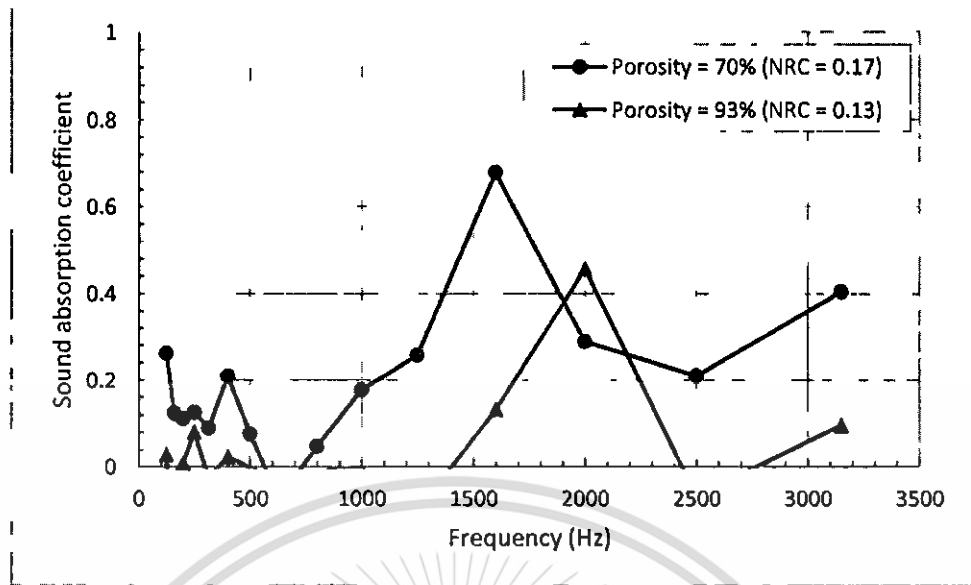


Figure 4.55 Effect of sample porosity (%) on sound absorption coefficient of aluminium foams pore size 4.1 mm with thickness of 8 mm (no an air gap cavity).

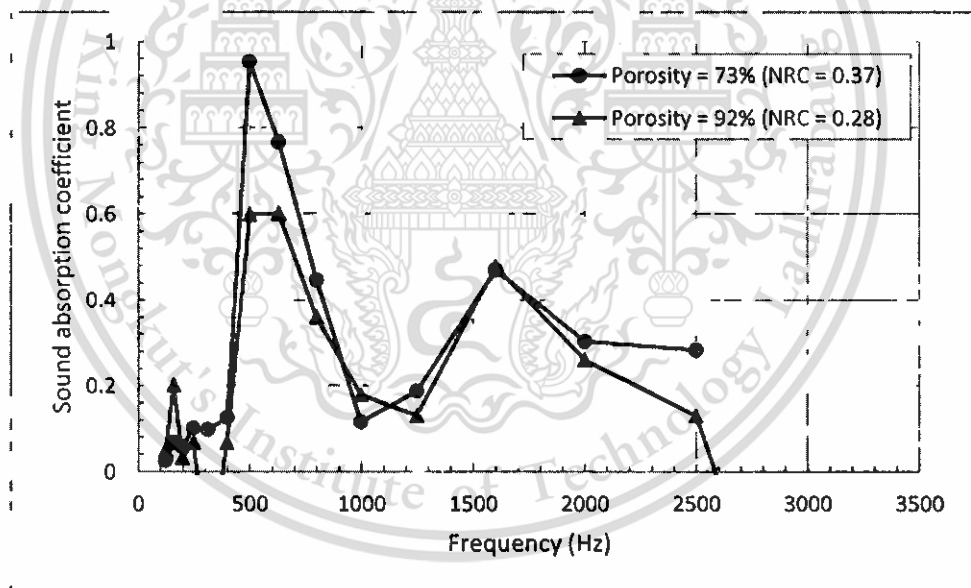


Figure 4.56 Effect of sample porosity (%) on sound absorption coefficient of aluminium foams pore size 4.1 mm with thickness of 50 mm (no an air gap cavity).

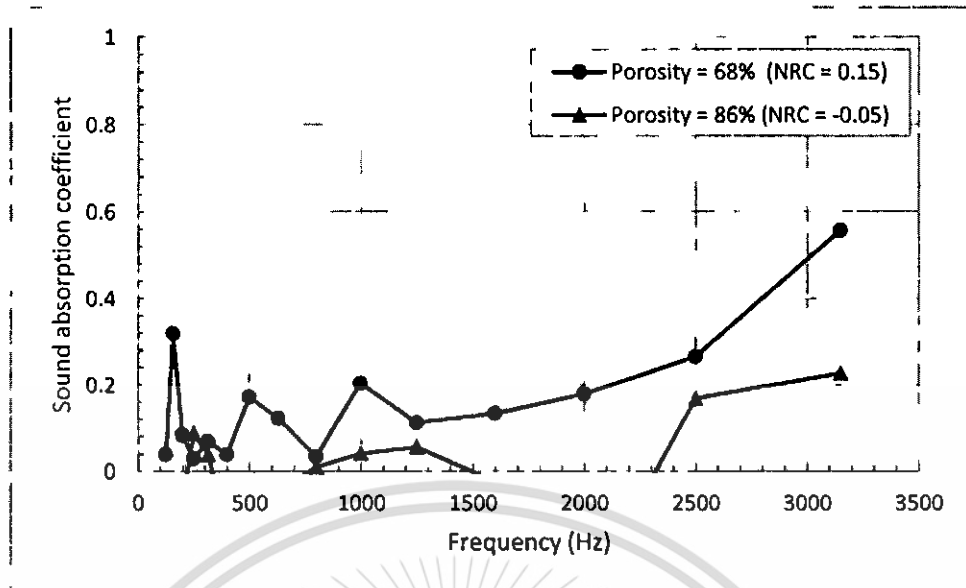


Figure 4.57 Effect of sample porosity (%) on sound absorption coefficient of aluminium foams pore size 5 mm with thickness of 8 mm (no an air gap cavity).

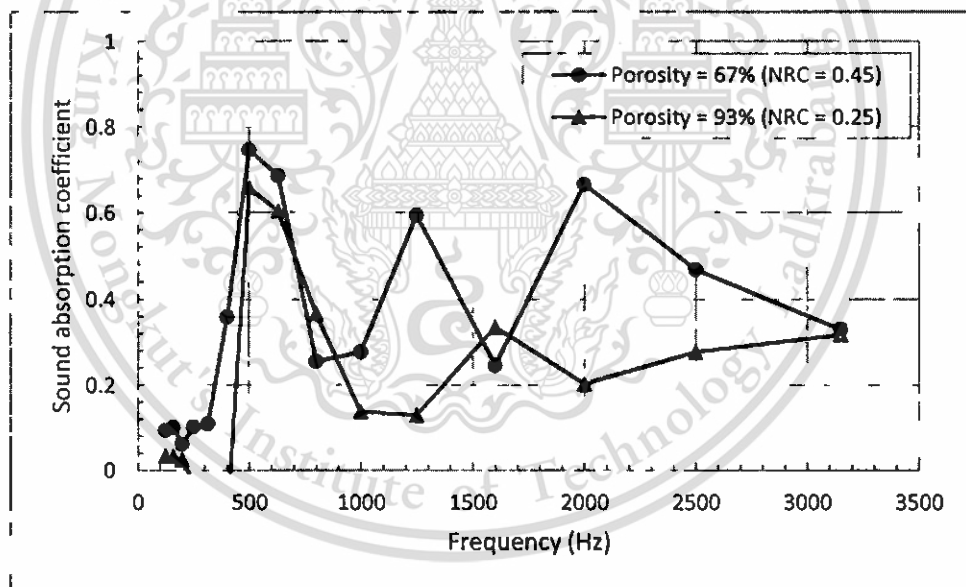


Figure 4.58 Effect of sample porosity (%) on sound absorption coefficient of aluminium foams pore size 5 mm with thickness of 50 mm (no an air gap cavity).

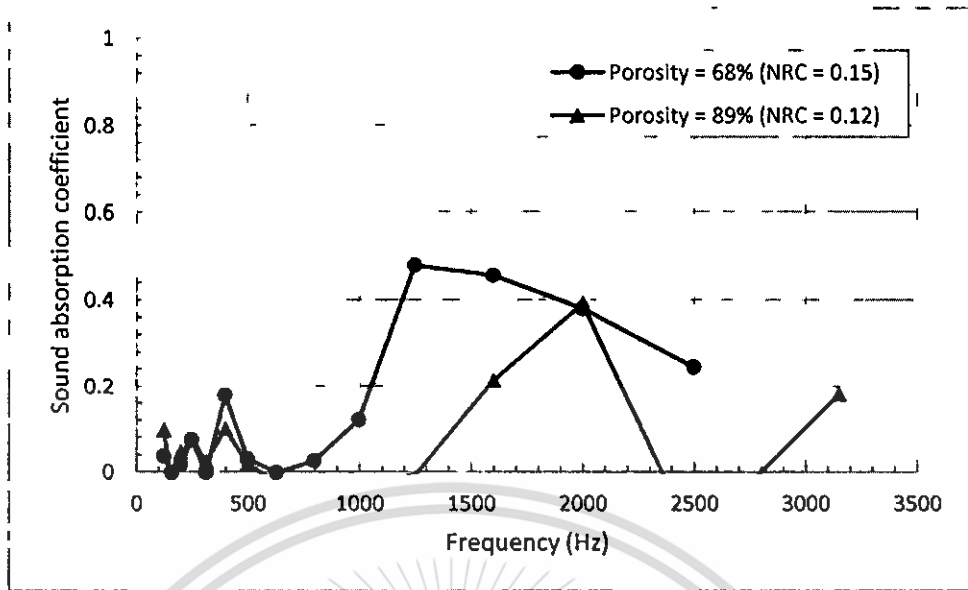


Figure 4.59 Effect of sample porosity (%) on sound absorption coefficient of aluminium foams pore size 6.3 mm with thickness of 8 mm (no an air gap cavity).

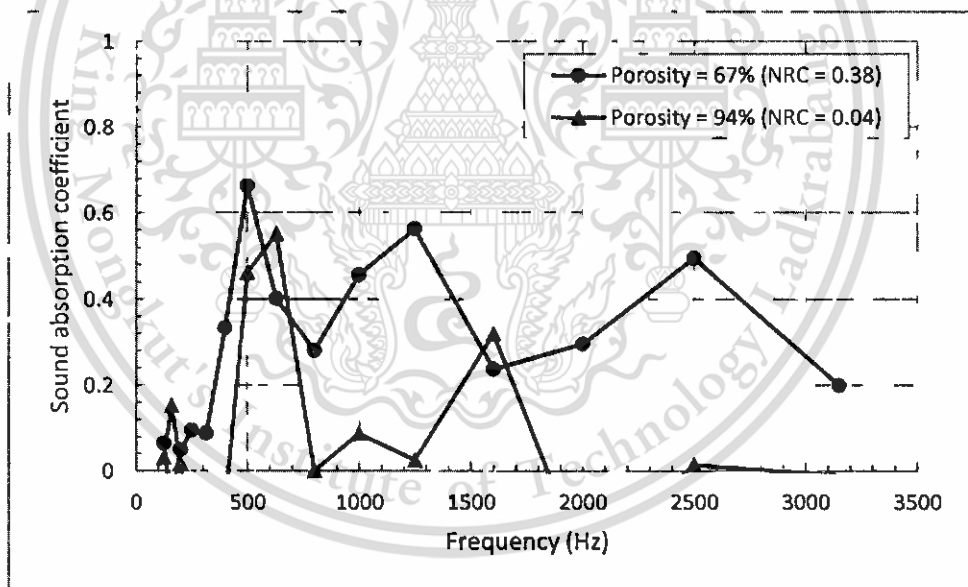


Figure 4.60 Effect of sample porosity (%) on sound absorption coefficient of aluminium foams pore size 6.3 mm with thickness of 50 mm (no an air gap cavity).

4.4.2 The Use of Models for Prediction of Sound Absorption Performance of Al foams

Sound absorption coefficients of aluminium foams with semi-open structure which is identical to aluminium foams used in this work has been predicted using models as

This material is reserved for educational use only, not allowed for commercial use.

Forbidden to modify the content, and cite the document when use.

shown in **Table 2.5** (in Chapter 2). **Table 4.7** shows structural parameters of aluminium foams used in predictions by others.

Table 4.7 Structural parameters used to predict sound absorption coefficients of aluminium foams by previous researchers.

Author	Sample	Unit cell (number)	Air gap (mm)	Thickness (mm)	Porosity (%)	Pore size (mm)	Aperture (mm)	P/Ap (ratio)
Hakamada [87]	A	-	-	-	95	-	-	-
	B	74	0	20	90	0.26	0.04	7.11
	C	75	0	20	85	0.26	0.03	7.53
	D	42	0	20	90	0.46	0.04	10.87
	E	29	0	20	90	0.67	0.07	9.93
	F	74	0	20	85	0.26	0.09	2.91
Li [49]	C	15	0	10	65	1.30	0.32	4.06
	C	15	0	15	65	1.30	0.32	4.06
	C	15	0	20	65	1.30	0.32	4.06
Lu [50]	a	20	0	20	66	0.43	0.14	3.14
	b	20	0	20	63	0.84	0.25	3.34
	c	20	0	20	66	0.86	0.34	2.50
	d	20	0	20	65	1.06	0.40	2.65
	f	20	0	20	60	1.00	0.3	3.33

It can be seen from **Table 4.7**

Table 4.7 that the maximum pore and aperture size of aluminum foam used for sound absorption coefficient predictions in previous research are 1.3 and 0.4 mm, respectively. However, the aluminium foams produced in this work contained pore and aperture size of 4.1 - 6.3 mm and 0.76 – 1.44 mm, respectively, which are significantly higher than those presented in **Table 4.7**. A model based on equivalent electrical circuit approach (EECA) (**Table 2.5**) was used for sound absorption coefficient prediction of aluminium foams in this work. For example, the sound absorption performance of aluminium foam samples can be predicted using the EECA equations given by Equations 2.28 – 2.33. Substituting the parameters⁷ of 6.3 mm foam samples (sample-(a) in table 4.6) in the

⁷ Replacing $L = 8.4$ mm, $D = 4.10$ mm, $t = 3.6 \times 10^{-4}$ m in Equation $n = L/((D + t))$, gives $n = 2$ which is a number of unit cells for sound absorption calculation. Replacing $\rho_0 = 1.14$ kg/m³, $c_0 = 349.58$ m/s (calculated at temperature = 31 °C), $D = 4.10$ mm, $f =$

mentioned equations, a value of α of 5×10^{-5} is obtained for frequency of 125 Hz. Similar calculations were carried out at other frequencies and samples. Prediction and experimental results based on impedance tube method are given in **Figure 4.61 - Figure 4.79**. It was found that experimental results are comparable with calculated results with only some samples, i.e. e, f, g, j, l, m, q and s as shown in **Figure 4.65, Figure 4.66, Figure 4.67, Figure 4.70, Figure 4.72, Figure 4.73, Figure 4.77 and Figure 4.79**. Most samples showed lower sound absorption coefficients of those obtained by measurements than predictions, i.e. a, b, h, i, j, k, n, o and p as shown in **Figure 4.61, Figure 4.63, Figure 4.68, Figure 4.69, Figure 4.70, Figure 4.71, Figure 4.74 and Figure 4.76**. Nevertheless, samples with increasing thickness and decreasing pore size showed more agreement of results between measurement and prediction, i.e. f and g as shown in **Figure 4.66 - Figure 4.67**. Sample j exhibited the best agreement between measurement and prediction at frequencies higher than 400 Hz as shown in **Figure 4.70**. Degree of agreement of sound absorption coefficient results between measurement and prediction can be calculated using equation as shown below

$$\Delta\alpha = \left(\frac{\alpha_{\text{measurement}} - \alpha_{\text{prediction}}}{\alpha_{\text{measurement}}} \right) \times 100 \quad (4.1)$$

Relations between the values of difference between measurement and prediction of sound absorption coefficients and other parameters such as pore/aperture ratio, pore size and sample thickness are shown in **Figure 4.80 - Figure 4.82**. At low frequencies such as 125, 160 and 200 Hz, samples g and s showed the best agreement between prediction and measurement since their difference less than 20 percent as shown in **Figure 4.80**. Samples with thicker thickness and smaller pore size also showed better agreement of sound absorption coefficient results between measurement and prediction.

125 Hz and $\omega = 785.4$ rad/s (calculated from $\omega = 2\pi f$) in Equation 2.28, gives $Z_D = -1865.6i$. Replacing $\eta = 1.9 \times 10^{-5}$ kg/m·s, $t = 4.8 \times 10^{-4}$ (calculated from $t = (1 - \Omega)D/[3.55 - 6(d/D)^{1/2}]$), $d = 6.8 \times 10^{-4}$ m, $\beta = 4.4 \times 10^{-5}$ (calculated from $\beta = (\omega\rho_0\eta)^{1/2}d/2$), $\Omega = 70\%$, $\omega = 785.4$ rad/s and $D = 4.1$ mm in Equation 2.29 and 2.30, gives $R_0 = 0.5$ and $M_0 = 24.4$ respectively. Replacing $Z_D = -1865.6i$ and $z_0 = 14.9 + 732.4i$ (calculated from $z_0 = (R_0 + iM_0)(0.909D/d)$) in Equation 2.31, gives $Z_1 = 14.9 - 1133.3i$. Replacing $z_0 = 14.9 + 732.4i$, $Z_D = -1865.6i$ and $Z_n = 14.9 - 1133.3i$ in Equation 2.32, gives $Z_n = R_n + iM_n = 27.6 + 27.3i$. Finally replacing $R_n = 27.6$, $M_n = 27.3i$, $\rho_0 = 1.14$ kg/m³ and $c_0 = 349.58$ m/s in Equation 2.33 gives $\alpha = 5 \times 10^{-5}$.

This material is reserved for educational use only, not allowed for commercial use.

Forbidden to modify the content, and cite the document when use.

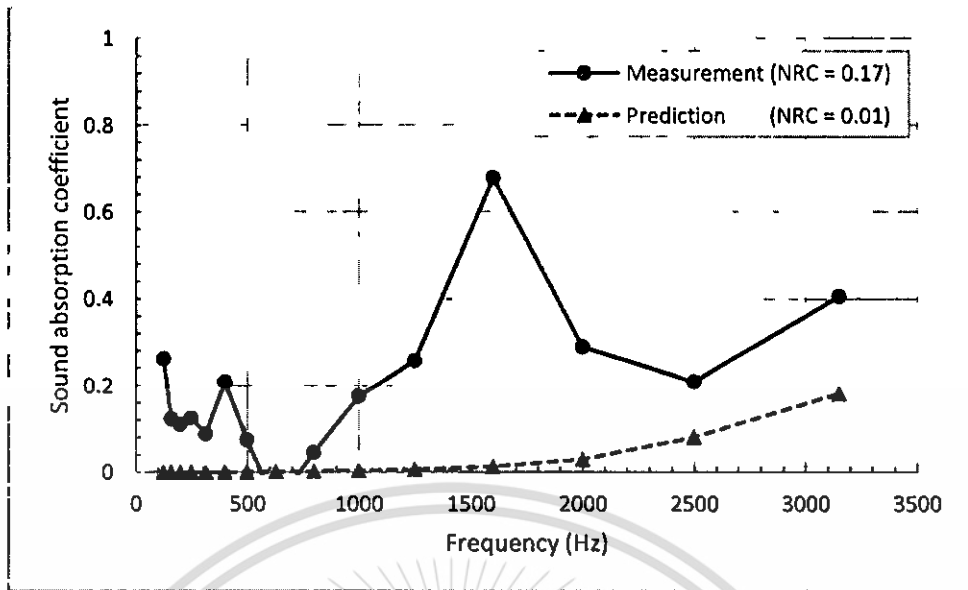


Figure 4.61 Measured and predicted sound absorption coefficients of aluminium foam a (denoted in Table 4.6) with thickness of 8.4 mm.

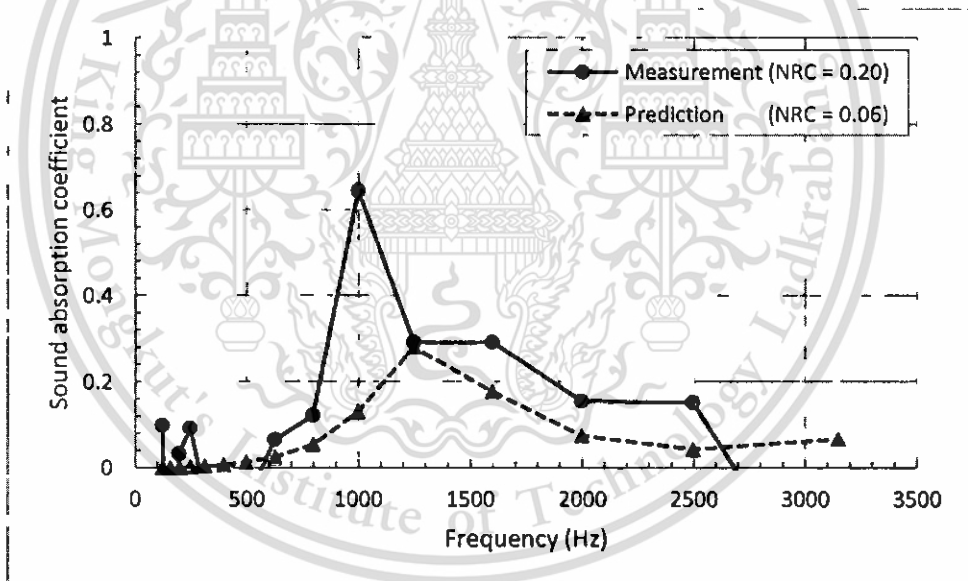


Figure 4.62 Measured and predicted sound absorption coefficients of aluminium foam b (denoted in Table 4.6) with thickness of 24.85 mm.

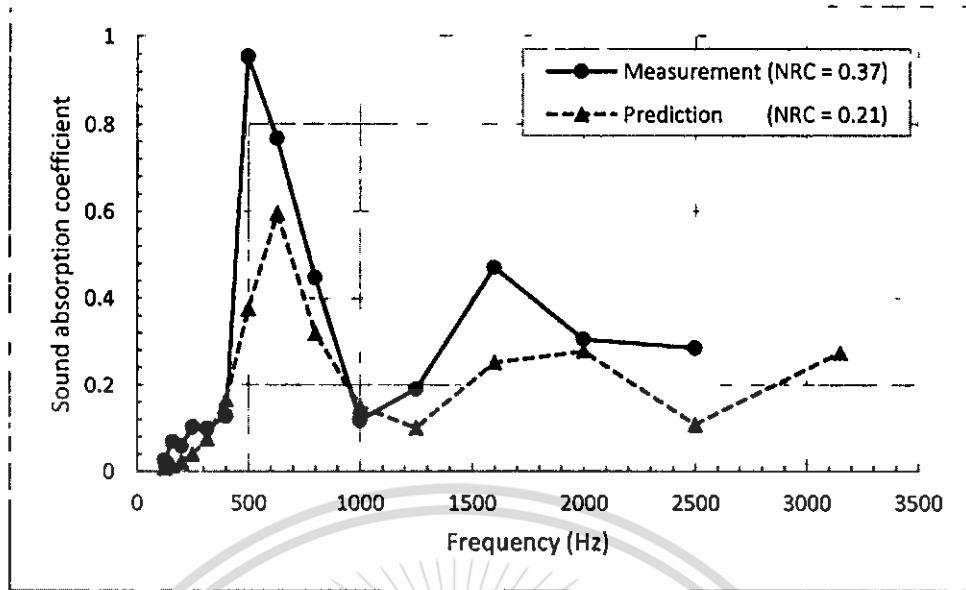


Figure 4.63 Measured and predicted sound absorption coefficients of aluminium foam c (denoted in **Table 4.6**) with thickness of 55.85 mm.

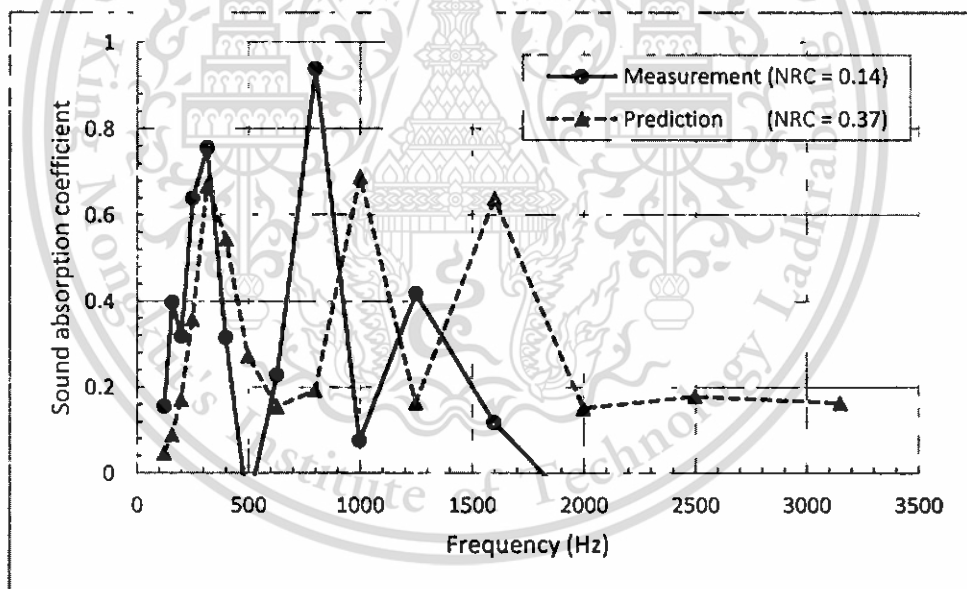


Figure 4.64 Measured and predicted sound absorption coefficients of aluminium foam d (denoted in **Table 4.6**) with thickness of 115.22 mm.

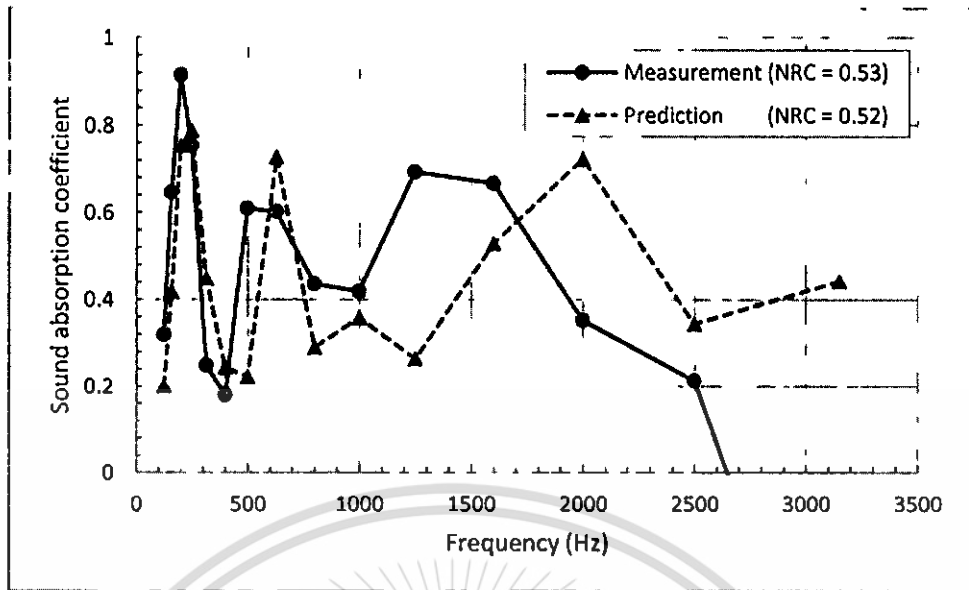


Figure 4.65 Measured and predicted sound absorption coefficients of aluminium foam e (denoted in Table 4.6) with thickness of 172.98 mm.

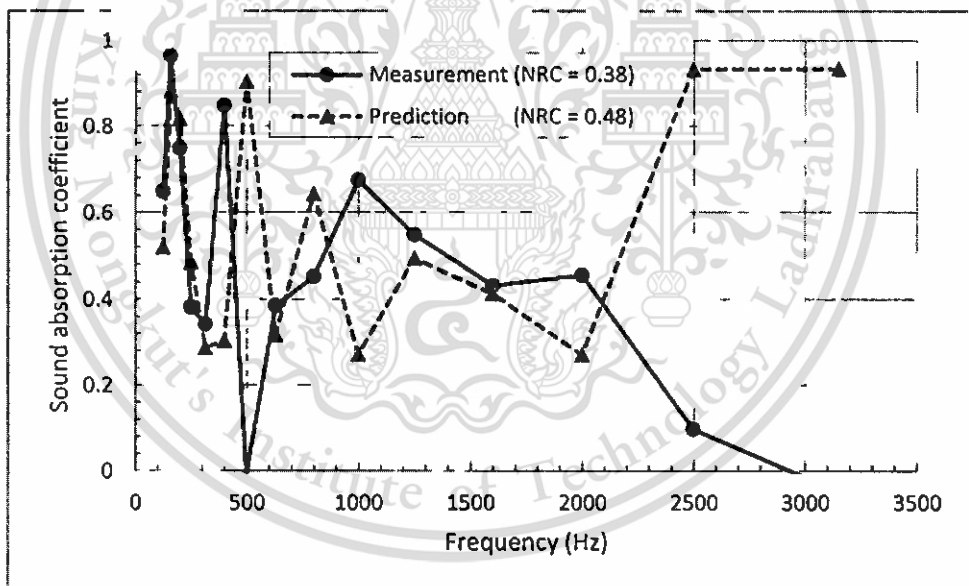


Figure 4.66 Measured and predicted sound absorption coefficients of aluminium foam f (denoted in Table 4.6) with thickness of 229.25 mm.

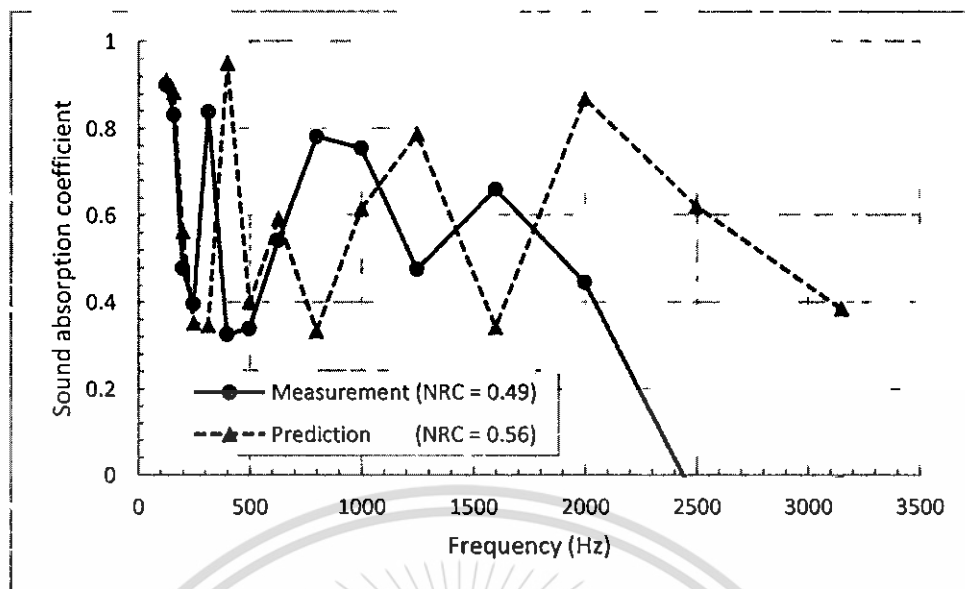


Figure 4.67 Measured and predicted sound absorption coefficients of aluminium foam g (denoted in Table 4.6) with thickness of 281.19 mm.

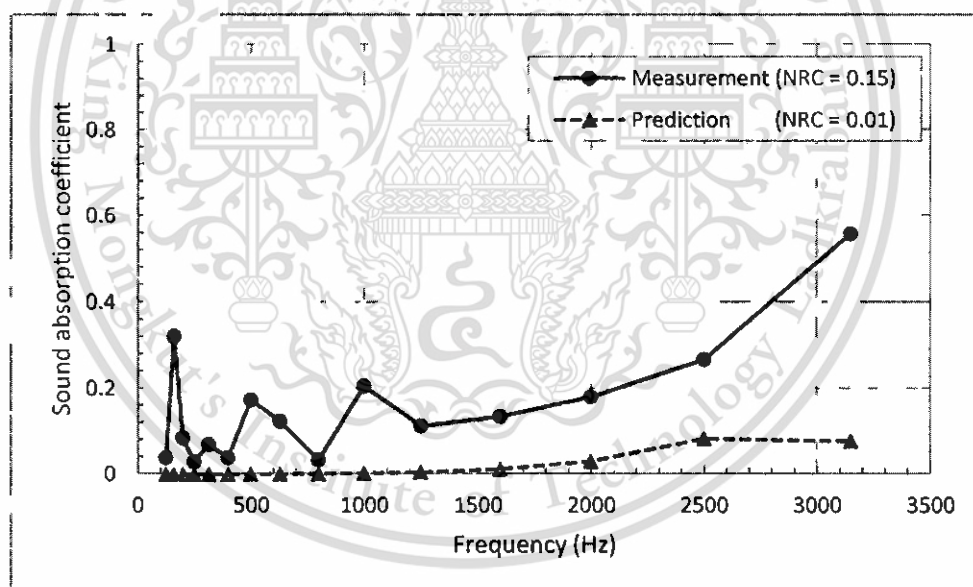


Figure 4.68 Measured and predicted sound absorption coefficients of aluminium foam h (denoted in Table 4.6) with thickness of 8.49 mm.

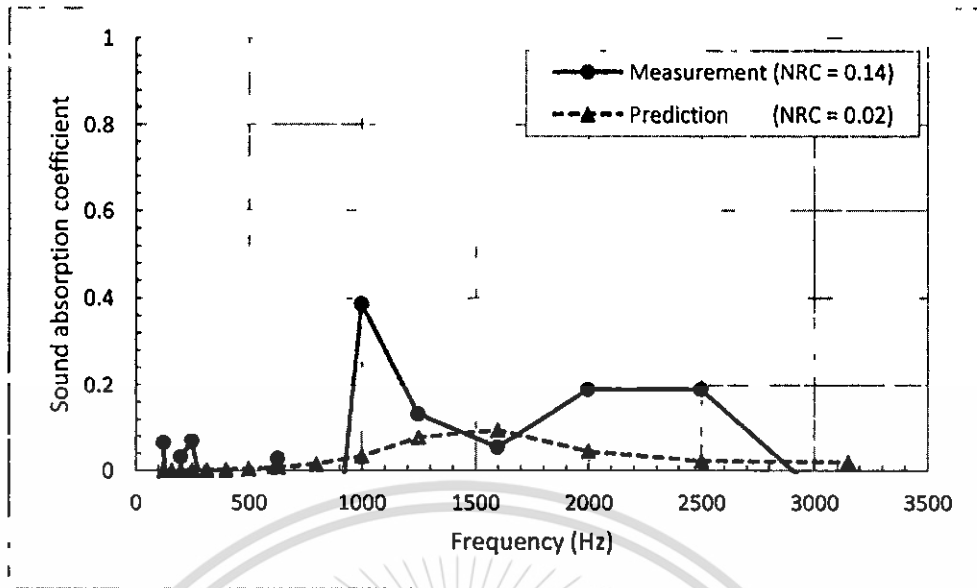


Figure 4.69 Measured and predicted sound absorption coefficients of aluminium foam i (denoted in **Table 4.6**) with thickness of 24.97 mm.

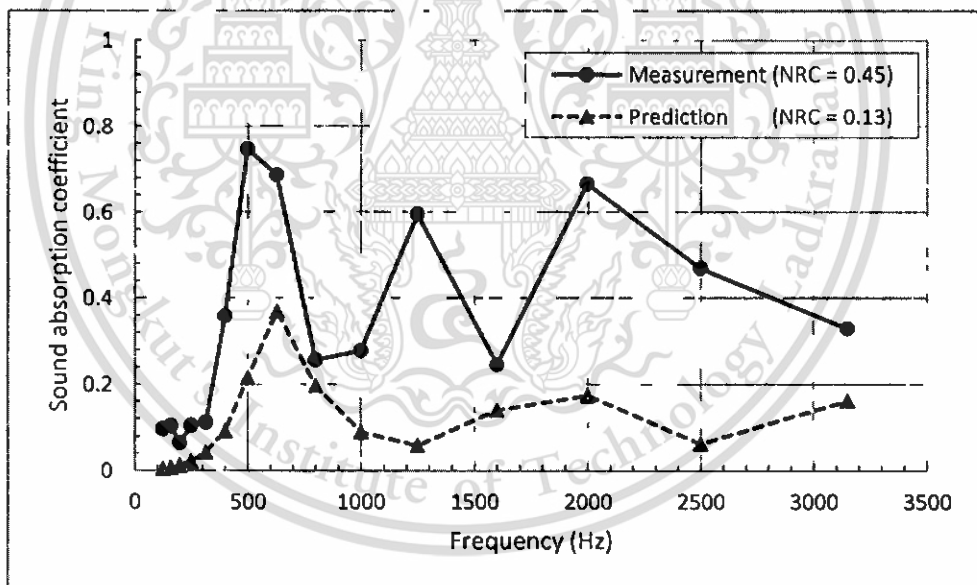


Figure 4.70 Measured and predicted sound absorption coefficients of aluminium foam j (denoted in **Table 4.6**) with thickness of 60.52 mm.

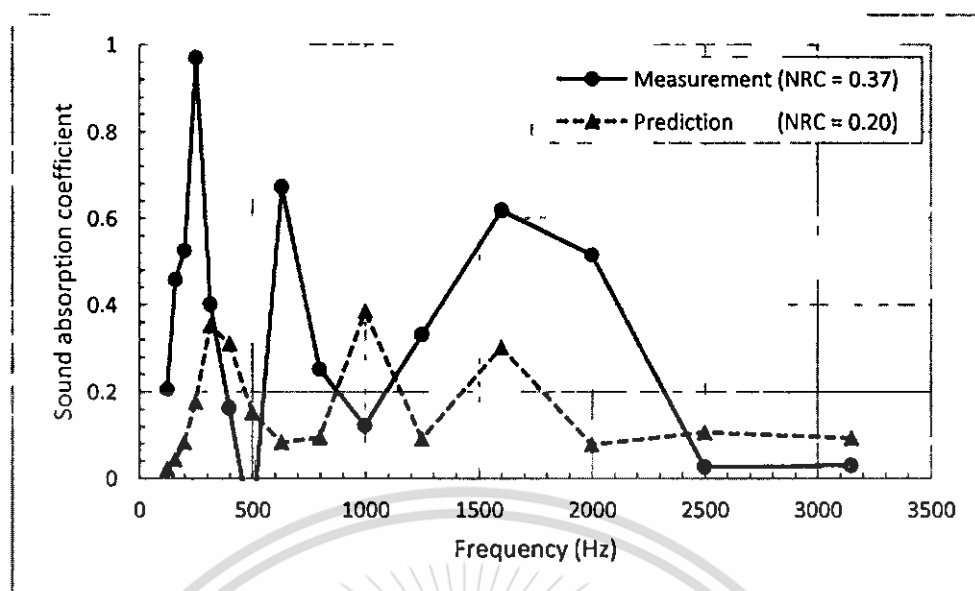


Figure 4.71 Measured and predicted sound absorption coefficients of aluminium foam k (denoted in Table 4.6) with thickness of 125.94 mm.

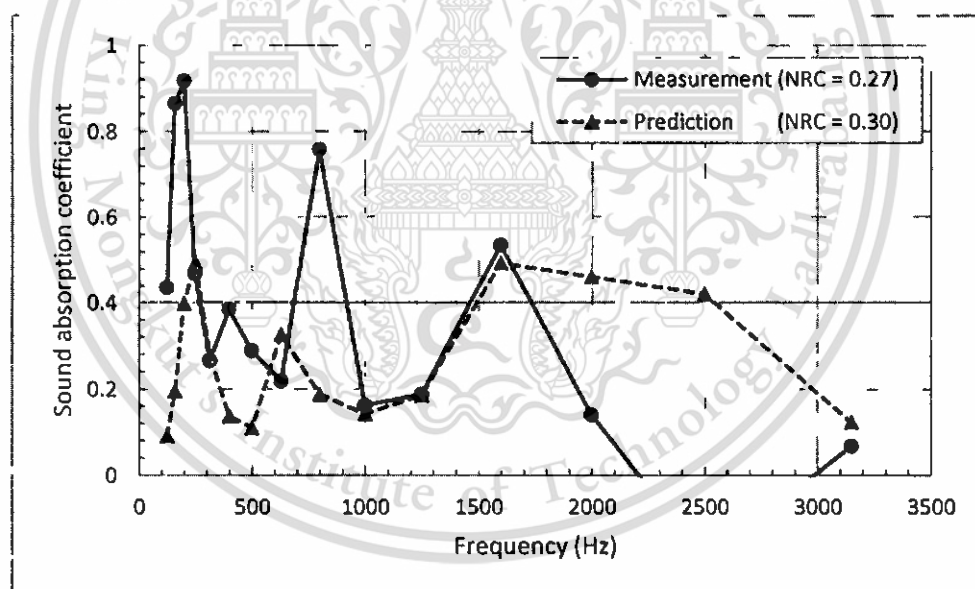


Figure 4.72 Measured and predicted sound absorption coefficients of aluminium foam l (denoted in Table 4.6) with thickness of 186.46 mm.

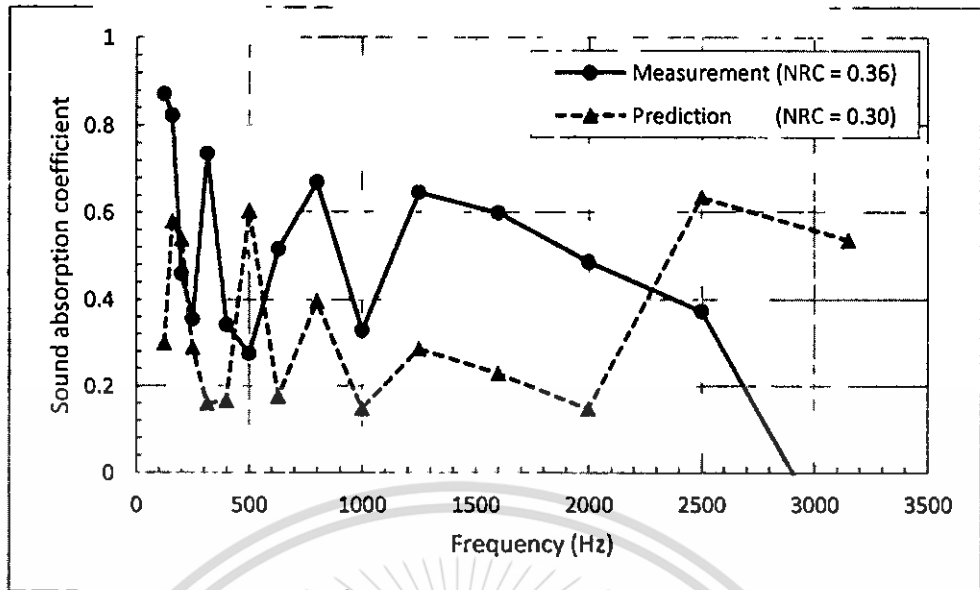


Figure 4.73 Measured and predicted sound absorption coefficients of aluminium foam m (denoted in Table 4.6) with thickness of 251.62 mm.

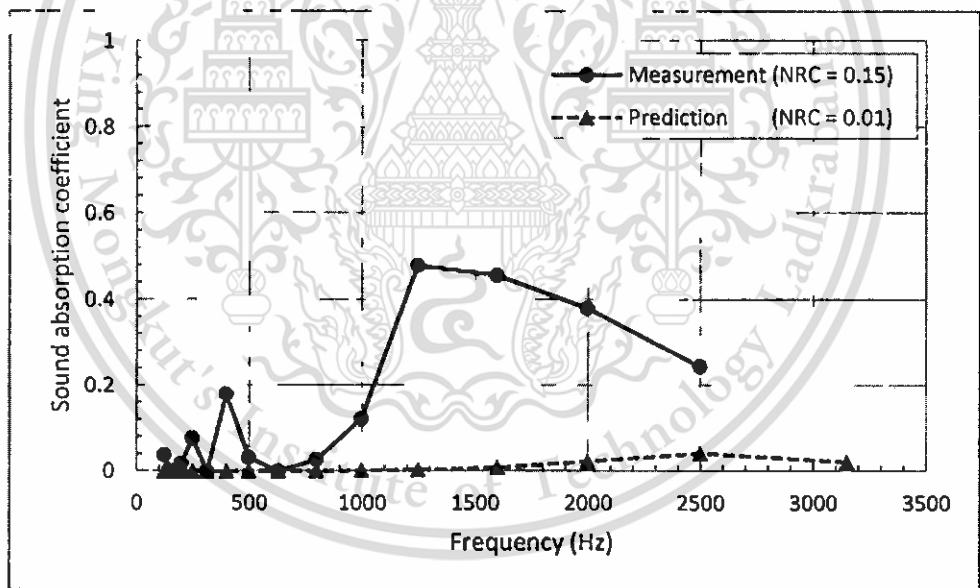


Figure 4.74 Measured and predicted sound absorption coefficients of aluminium foam n (denoted in Table 4.6) with thickness of 8.51 mm.

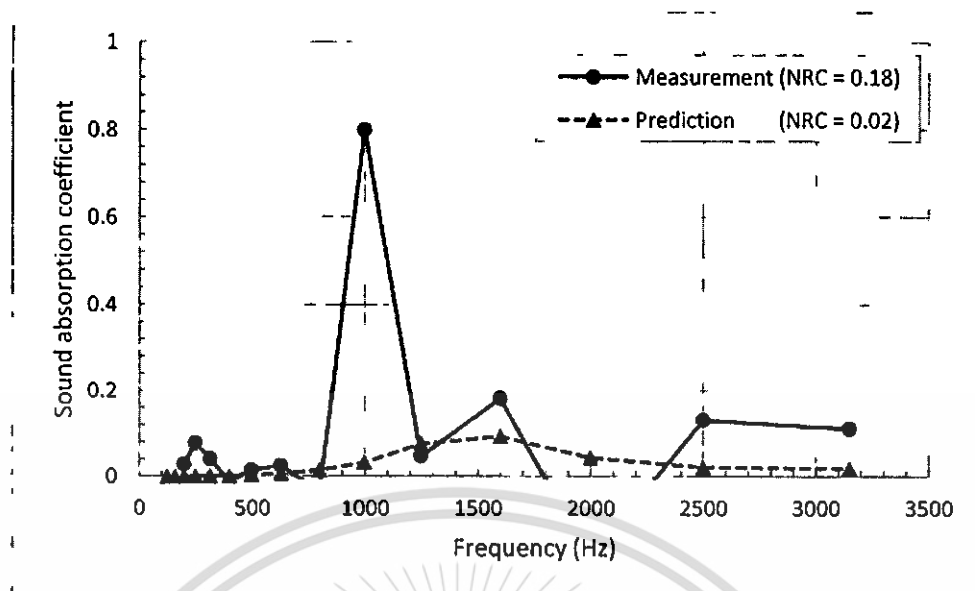


Figure 4.75 Measured and predicted sound absorption coefficients of aluminium foam o (denoted in Table 4.6) with thickness of 24.83 mm.

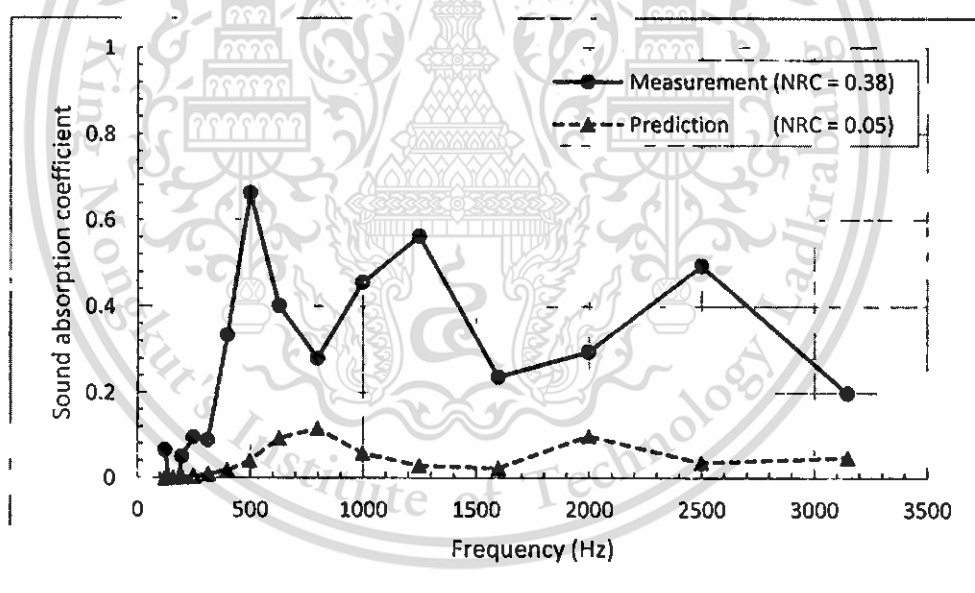


Figure 4.76 Measured and predicted sound absorption coefficients of aluminium foam p (denoted in Table 4.6) with thickness of 61.98 mm.

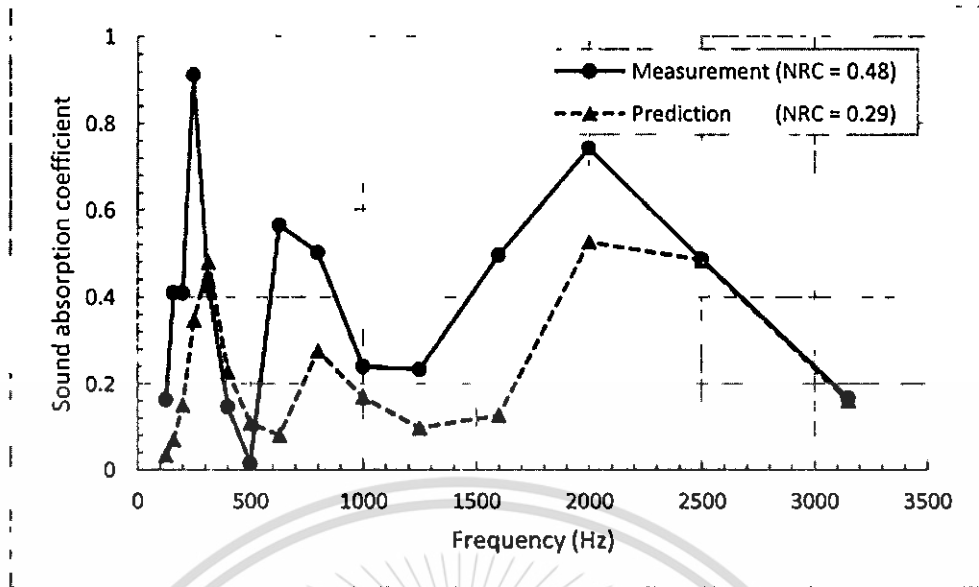


Figure 4.77 Measured and predicted sound absorption coefficients of aluminium foam q (denoted in Table 4.6) with thickness of 127.58 mm.

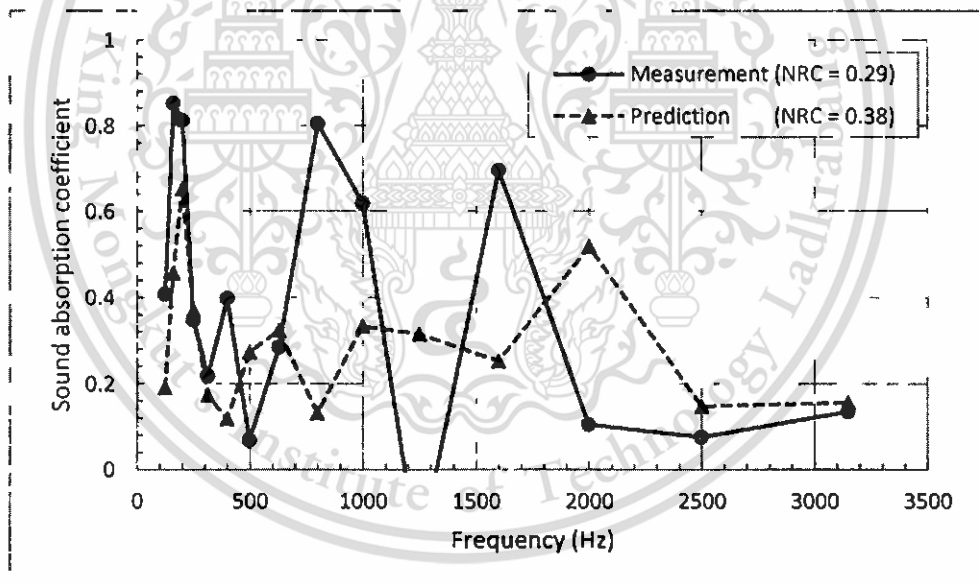


Figure 4.78 Measured and predicted sound absorption coefficients of aluminium foam r (denoted in Table 4.6) with thickness of 194.19 mm.

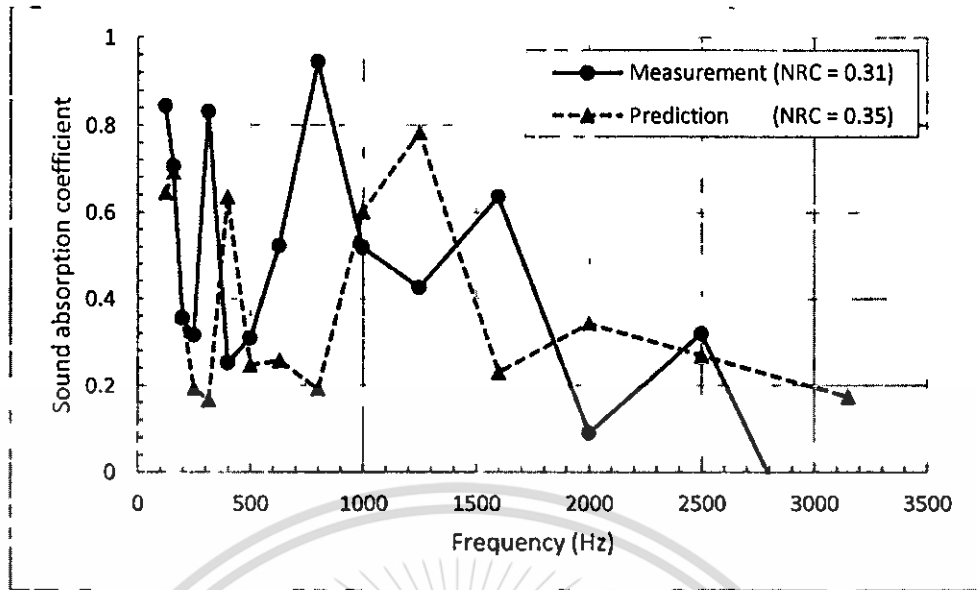


Figure 4.79 Measured and predicted sound absorption coefficients of aluminium foam s (denoted in Table 4.6) with thickness of 260.06 mm.

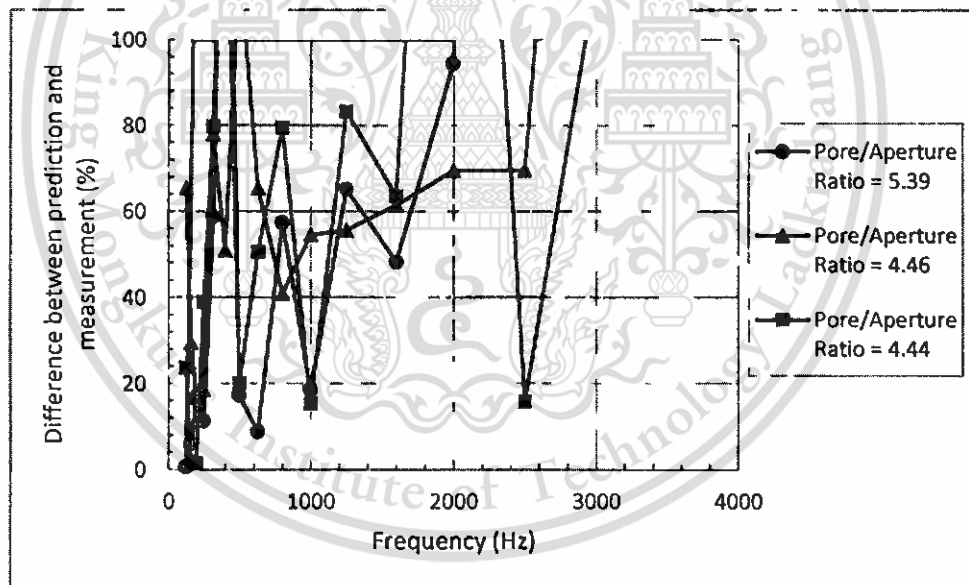


Figure 4.80 Difference between measurement and prediction of sound absorption coefficients of aluminium foams having thicknesses 252 – 281 mm with different pore/aperture ratios.

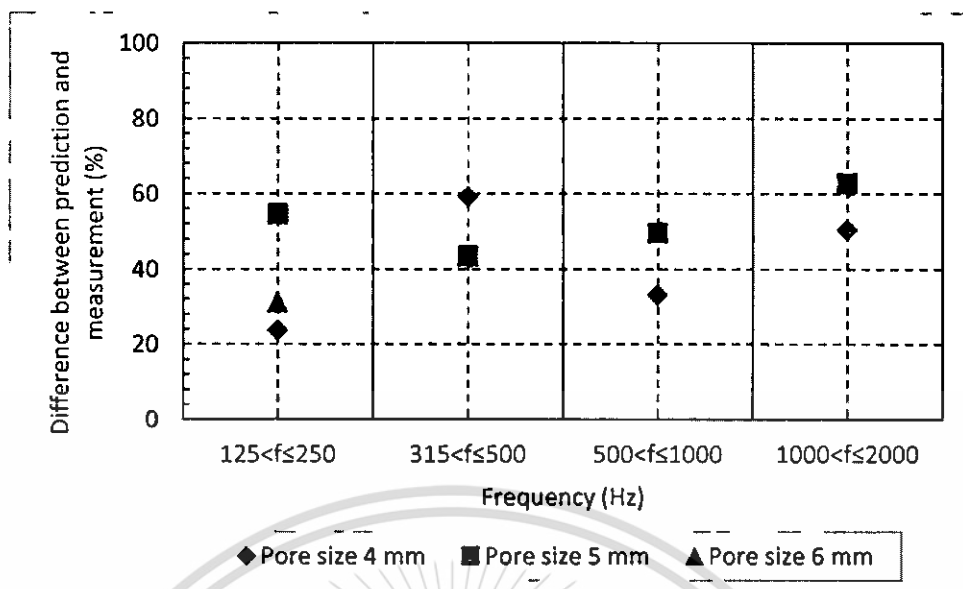


Figure 4.81 Difference between measurement and prediction of sound absorption coefficients of aluminium foams having thicknesses 173 to 194 mm (unit cell 28 - 39) with different pore sizes.

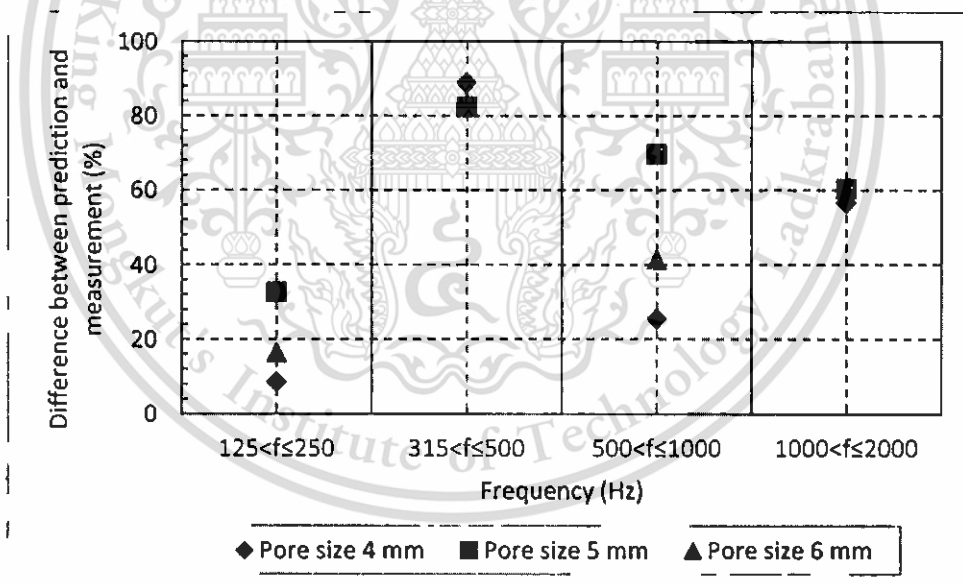


Figure 4.82 Difference between measurement and prediction of sound absorption coefficients of aluminium foams having thicknesses 252 to 281 mm (unit cell 46 - 63) with different pore sizes.

4.4.3 Sound Absorption Material for Automotive applications

From types of noise sources with frequency zones in automotive vehicle data shown in **Figure 2.4** (chapter 2) suggests that noise source of powertrain occurring with mid frequency range 250-1,600 Hz. According to data from [5, 88] indicated that noise

source from powertrain system (exhaust noise) incurs at high sound pressure level. It can be noticed that noise in a passenger compartment as recommend in **Table 2.1** should be used in automotive design.

Nowadays, most sound absorptive materials in automotive are not good in sound absorption at low frequencies as shown in **Figure 2.10** and most of them are inappropriate to be installed outside the automotive compartment. From experiment results of sound absorption measurement of aluminum foams produced in this work as shown in **Figure 4.83 - Figure 4.85**, aluminium foams with all pore size exhibited their sound absorption performance at low frequencies as good as non-woven materials. However, their sound absorption performance was still quite low. Nevertheless, the sound absorption ability at low frequency of aluminium foams can be improved by increasing sample thickness and adjusting installation by having an air cavity at the back of the aluminium foams.

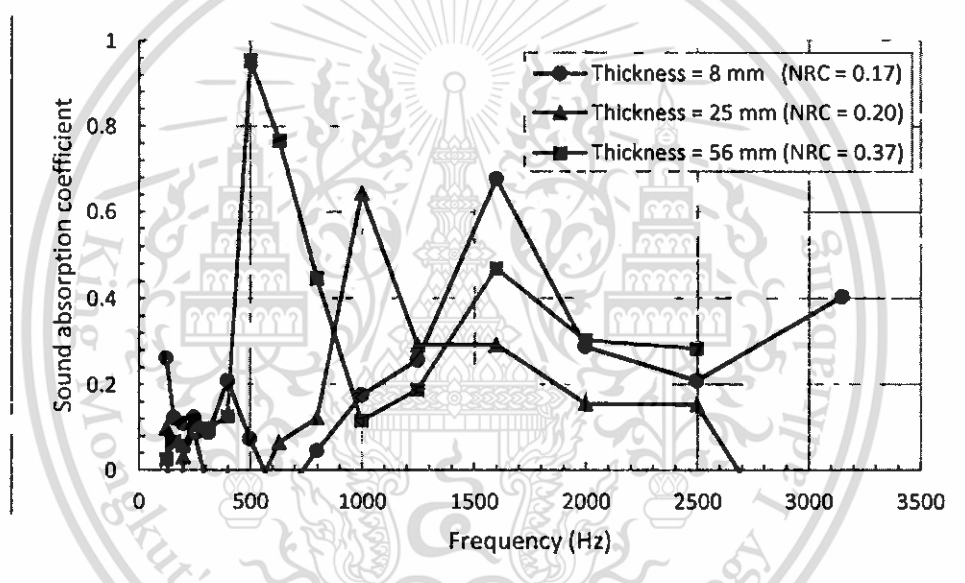


Figure 4.83 Measured sound absorption coefficient of aluminium foams having pore size of 4 mm and thickness of 8, 25 and 56 mm.

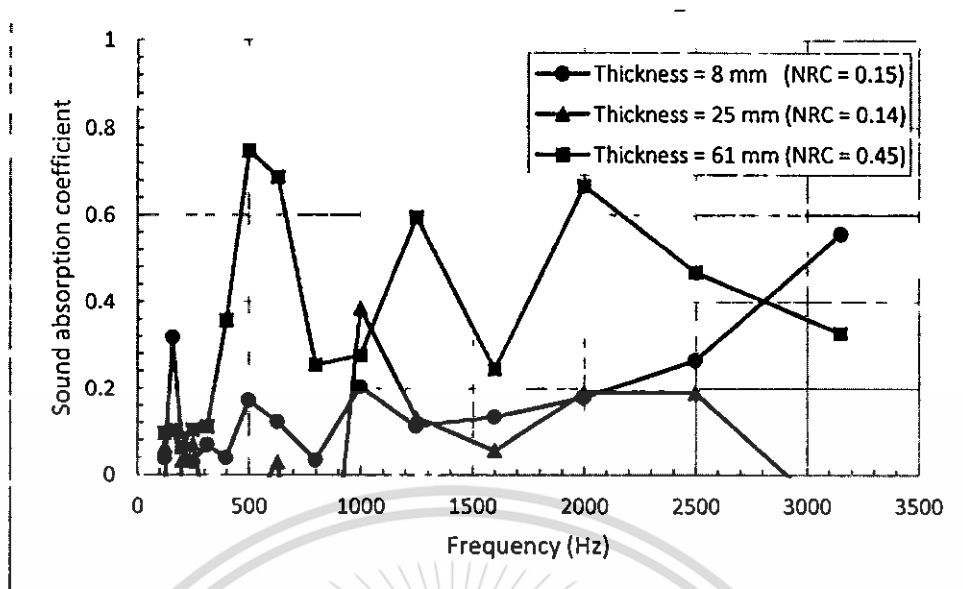


Figure 4.84 Measured sound absorption coefficient of aluminium foams having pore size of 5 mm and thickness of 8, 25 and 61 mm.

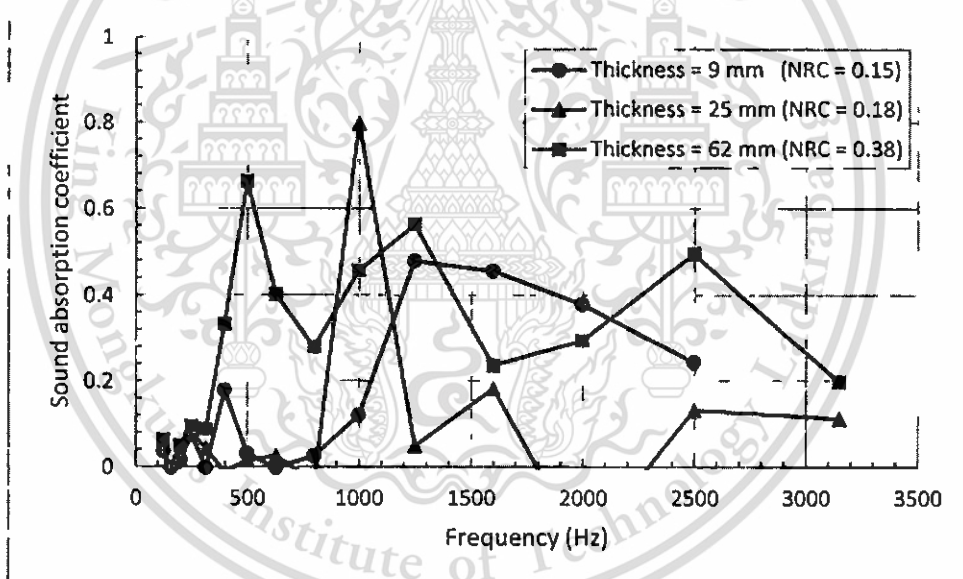


Figure 4.85 Measured sound absorption coefficient of aluminium foams having pore size of 6.3 mm and thickness of 9, 25 and 62 mm.

Examples of sound absorption performance of 5, 25 and 50 mm thickness aluminium foams with installation having different air gaps in the range 0 – 30 mm illustrates in **Figure 4.86 - Figure 4.88**. It was found that aluminum foams can absorb more sound than non-woven materials ($\alpha = 0.5$) at low frequency range of 500 – 1,000 Hz as shown in **Figure 4.87**. Consequently aluminium foams can be used for noise reduction occurred from powertrain system (exhaust noise) in the low frequency range. Aluminium foams produced in this work might be most suitable for use at trunk floor of road vehicles for sound absorption purpose. Because aluminium foam panel which is installed at location of a truck floor can be applied an air gap in order to increase sound absorption performance and can absorb energy from crashing. In addition the

This material is reserved for educational use only, not allowed for commercial use.

aluminium foam panel can transfers thermal energy, especially for electric vehicles which contain large batteries on the floor in the trunk.

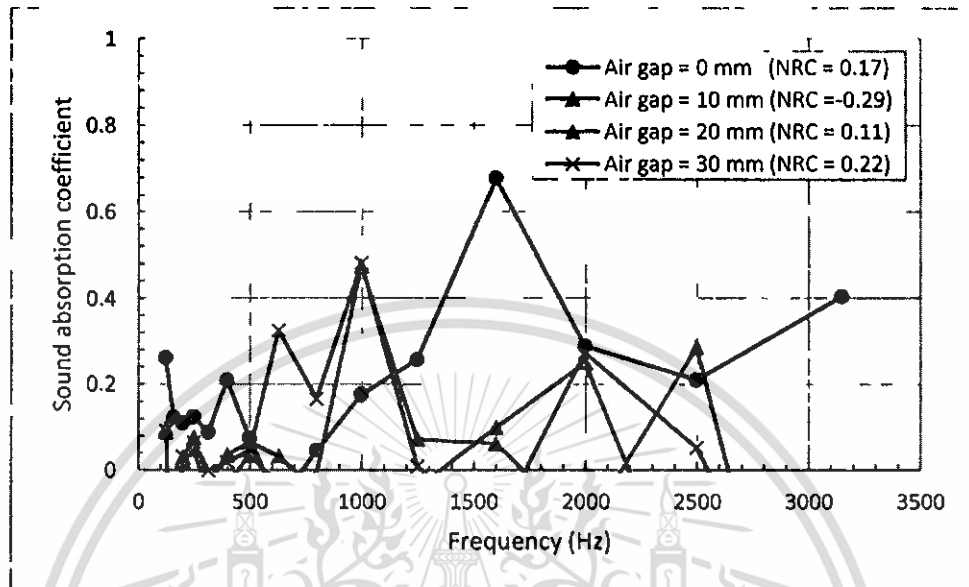


Figure 4.86 Effect of air gap cavity on sound absorption coefficient of aluminium foam samples a with sample thickness of 8 mm.

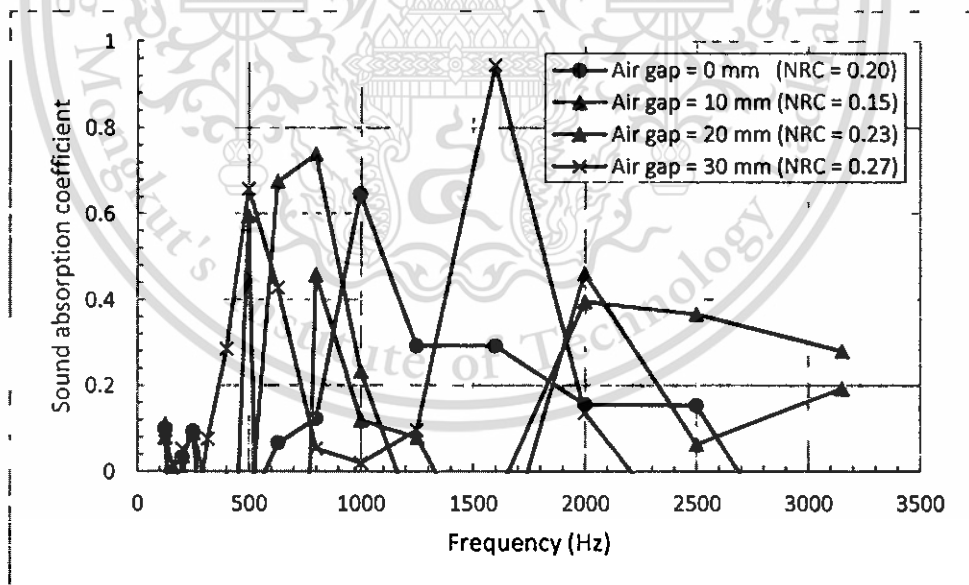


Figure 4.87 Effect of air gap cavity on sound absorption coefficient of aluminium foams for sample b with sample thickness of 25 mm.

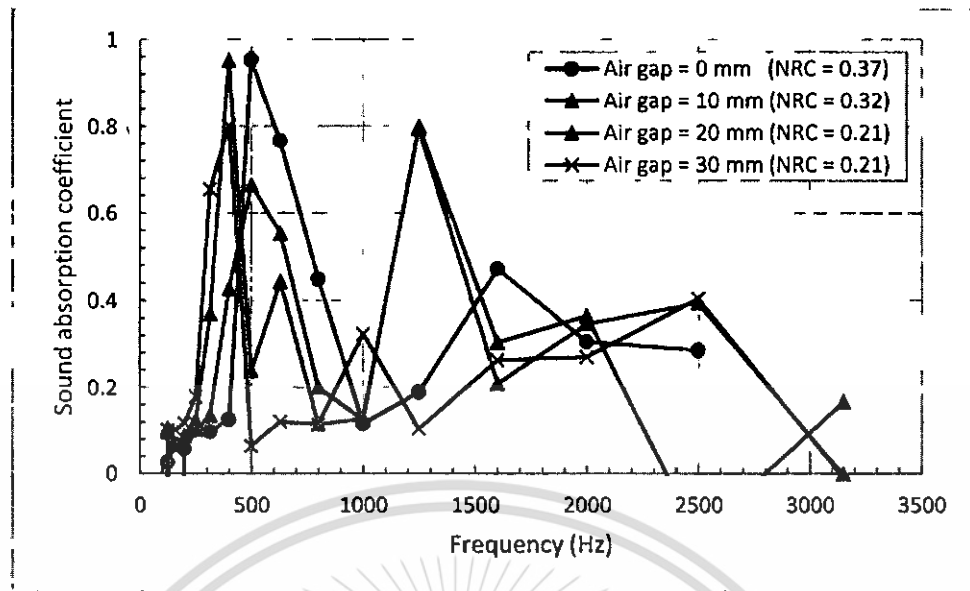


Figure 4.88 Effect of air gap cavity on sound absorption coefficient of aluminium foams for sample c with sample thickness of 50 mm.

CHAPTER 5 CONCLUSIONS AND SUGGESTIONS

5.1 Conclusions

Spherical shape preforms of sizes 4.1, 5.0 and 6.3 mm with a tolerance of ± 0.1 mm made from a water dissoluble substance were used as space holders for open cell aluminium foam production using infiltration technique with AC2A aluminium alloy. Structures and physical properties of the produced aluminium foams were found to be influenced by production parameters which are mold permeability, applied infiltration pressure and melt temperature. Three main structures: incomplete, dense and spongy were obtained mainly from no infiltration, full infiltration with residue metal and full infiltration without residue metal, respectively.

The obtained results of foam structures by varying applied pressures in the ranges -95 to -10 kPa were in good agreement with saturation prediction. The saturation and density of aluminium foams increased when low applied pressure and mold permeability were employed but decreased when high mold permeability was used irrespective to the level of applied pressure. At a constant applied pressure of -20 kPa and pouring temperature of 620 – 630°C, dense and spongy aluminium foams with density of 0.67 and 0.17 g/cm³ were obtained when the molds having gas permeability coefficient of 31.26 and 44.35 x 10⁻¹² m², respectively, were used. It was found that foam structure was significantly affected by mold permeability and pouring temperature. Moreover, Young-Laplace equation gave a good prediction of threshold pressure required to infiltrate into space among preforms.

Pouring temperature was found to inversely proportional to both saturation and infiltration weight (%) which gave enormous impact on foam structure. Low pouring temperatures, such as 620 – 630°C (molds having gas permeability of 31.26 x 10⁻¹² m²), were found to provide the best dense foam structure with residue metal (infiltration type-II). Higher pouring temperatures (irrespective to mold permeability) were found to give aluminium foams with incomplete structure. A ratio between residue and retained metal that gave full infiltration was found to be approximately 40:60. The aluminium foams produced using molds with medium and high permeabilities (pouring temperature of 620 – 630°C) had densities 0.15 - 0.27 and 0.75 - 0.98 g/cm³ respectively.

Aluminium foams with dense structure having infiltration close to 85% contained relatively uniform structure. Optimum production parameters for producing aluminium foams with spongy and dense structure are permeability coefficient of mold of 31.26 and 44.35 x 10⁻¹² m², respectively, together with the applied pressure of -20 kPa and the pouring temperature of 620°C.

Sound absorption coefficients of different thickness open cell aluminium foams produced by spherical preform sizes 4.1, 5 and 6.3 mm were measured using two-microphone impedance tube with transfer function method. It was found that increasing sample thickness enhanced the maximum peak of sound absorption and shifted bandwidth of sound absorption to lower frequencies. In addition, decreasing pore size from 6.3 to 4.1

mm was found to enhance sound absorption performance. The maximum sound absorption coefficient of 0.96 at the frequency of 500 Hz was obtained with the aluminium foam having pore size of 4.1 mm and thickness of 50 mm. Sound absorption performance at low frequencies was found to be improved by introducing an air cavity behind a foam sample, in which the peak of sound absorption coefficient shifted from 1,600 Hz to 500 Hz. A model based on equivalent electrical circuit approach was used to predict sound absorption coefficients of aluminium foams. Difference in sound absorption coefficient between measurement and prediction was found to increase with pore size and unit cell of foam samples.

For sound absorption material in road vehicles, aluminium foams having a combination of good sound absorption and excellent energy absorption performance are suitable to be used as a trunk floor where incident noises occurs at low frequencies in the range of 250 - 800 Hz. Furthermore, aluminium foams can enhance safety with energy absorption from crashing for the trunk.

5.2 Suggestions

The obtained results from experiments in this work suggest to use large space holder sizes to give aluminium foams with a complete structure. Any alternative base plates can be used to control mold permeability and hence foam structure. Better models should be developed to obtain a more comprehensive prediction of sound absorption of aluminium foams having a wide range of structure. Other production parameters which are those not present in this work, such as infiltration rate, preheat temperature of either mold or preform should be investigated to understand their effects on foam structure.

REFERENCES

1. Marberg H. **Acoustics of Light Weight Materials**. [Online]. Available : https://www.semcon.com/Global/Docs/AUTOMOTIVE/Lightweight/Semcon%20Lightweight%20Seminar_Semcon_Acoustics%20of%20lightweight%20materials.pdf.
2. Visèl™ N.R. **Noise and Source of Noise That Surrounds Car**. [Online]. Available : <http://www.peredam-visel.com/>.
3. Gagliardini L. **Vehicle NVH design**. [Online]. Available : https://intranet.sfa.asso.fr/archives/J59VANGSO/presentations/GAGLIARDINI_PSA_SFA_VAN_2010.pdf.
4. Lu J. 2008. "Acoustic Windshield Significantly Reduces Structure-borne and Airborne Noises for Diesel Vehicles and Brings Ecological Benefit." **SAE NVC**, SAE paper no. NVC03-31.
5. Putner J., Fastl H., Lohrmann M., Kaltenhauser A. and Ullrich F. 2012. "Operational transfer path analysis predicting contributions to the vehicle interior noise for different excitations from the same sound source." **This Paper presented at the 41st International Congress and Exposition on Noise Control Engineering 2012 (INTER-NOISE 2012)**. 19-22 August 2012, New York City, USA.
6. Munjal M. L. 2004. "Acoustic Characterization of an Engine Exhaust Source-A Review." **Proceedings of Acoustics**. pp. 117-122.
7. Martin F. **The Acoustics of the Golf VI**. 2008.
8. Foamtec Co., Ltd. **Foamtech aluminium foam leading company**. 2012. [Online]. Available : http://www.foamtech.co.kr/eng02/product/02_01_01_products.php?yun=01.
9. Studiotechnik A. **Sound Pressure**. 2012. [Online]. Available : <http://www.sengpielaudio.com/TableOfSoundPressureLevels.htm>.
10. Studiotechnik A. **Table of the Threshold of pain**. 2012. [Online]. Available : <http://www.sengpielaudio.com/TableOfSoundPressureLevels.htm>.
11. General M. **Sound experts use advanced technologies to make 2013 Malibu cabin quiet**. 2012. [Online]. Available : <http://media.gm.com/media/me/en/gm/news.detail.html/content/Pages/news/me/>

[en/2012/Chevrolet/Reduce_Noise_Chevrolet_Malibu_Engineers_are_All_Ears.html](http://www.parafix.com/en/2012/Chevrolet/Reduce_Noise_Chevrolet_Malibu_Engineers_are_All_Ears.html).

12. 3M T. **Automotive Acoustic Solutions**. 2012. [Online]. Available : <http://www.parafix.com/en/assets/File/Parafix%20%203M%20Automotive%20Acoustics%20Solutions.pdf>.
13. Arenas J. P. and Crocker M. J. 2010. "Recent Trends in Porous Sound-Absorbing Materials." **Sound & Vibration**. vol. 44, no. 7, pp. 12-18.
14. Zent A. and Long J. T. 2007. "Automotive sound absorbing material survey result." **SAE Technical Paper**. no. 2007-01-2186.
15. Patton H. W. 2005. "Smart Acoustic Material for Automotive Applications." Annual Progress Report.
16. Hakamada M., Kuromura T., Chen Y., Kusuda H. and Mabuchi M. 2006. "Sound Absorption Characteristics of Porous Aluminum Fabricated by Spacer Method." **Journal of Applied Physics**. vol.100, no.11, pp. 114908.
17. Banhart J. 2001. "Manufacture, Characterisation and Application of Cellular Metals and Metal Foams." **Progress in Materials Science**. vol. 46, no. 6, pp. 559-632.
18. Banhart J. **Metal foams—From Fundamental Research to Applications. Frontiers in the Design of Materials**. India : Universities Press Limited. 2007.
19. Ashby M. F., Evans T., Fleck N. A., Hutchinson J. W., Wadley H. N. G. and Gibson L. J. **Metal Foams: A Design Guide: A Design Guide**. : Elsevier. 2000.
20. Chumpia A. and Hooman K. 2014. "Performance Evaluation of Single Tubular Aluminium Foam Heat Exchangers." **Applied Thermal Engineering**. vol. 66, no. 1, pp. 266-273.
21. Mostafid A. M. "Entrance and exit effects on flow through metallic foams." Doctoral Dissertation Concordia University. 2007.
22. Garcia-Cordovilla C., Louis E. and Narciso J. 1999. "Pressure Infiltration of Packed Ceramic Particulates by Liquid Metals." **Acta Materialia**. vol. 47, no. 18, pp. 4461-4479.
23. Jinnapat A. and Kennedy A. 2011. "The Manufacture and Characterisation of Aluminium Foams Made by Investment Casting Using Dissolvable Spherical Sodium Chloride Bead Preforms." **Metals**. vol. 1, no. 1, pp. 49-64.

24. Despois J. F., Marmottant A., Salvo L. and Mortensen A. 2007. "Influence of The Infiltration Pressure on The Structure and Properties of Replicated Aluminium Foams." **Materials Science and Engineering: A**. vol. 462, no.1, pp. 68-75.
25. Goodall R., Marmottant A., Salvo L. and Mortensen A. 2007. "Spherical Pore Replicated Microcellular Aluminium: Processing and Influence on Properties." **Materials Science and Engineering: A**. vol. 465, no. 1, pp. 124-135.
26. Goodall R. and Mortensen A. 2007. "Microcellular Aluminium?–Child's Play!" **Advanced Engineering Materials**. vol. 9, no. 11, pp. 951-954.
27. Sbia L. A., Peyvandi A., Soroushian P., Balachandra A. M. and Sobolev K. 2015. "Evaluation of Modified-Graphite Nanomaterials in Concrete Nanocomposite Based on Packing Density Principles." **Construction and Building Materials**. vol. 76, pp. 413-422.
28. Chou K. S. and Song M. A. 2002. "A novel Method for Making Open-Cell Aluminum Foams with Soft Ceramic Balls." **Scripta Materialia**. vol. 46, no. 5, pp. 379-382.
29. Alvéotec. **Honeycomb casting process**. 2013. [Online]. Available : <http://www.alveotec.fr/en/innovation.html>.
30. Globomet. **Styropor Granules Sintering Process**. 2015. [Online]. Available : <http://hollomet.com/en/process.html>.
31. Eom J. H., Kim Y. W. and Raju S. 2013. "Processing and Properties of Macroporous Silicon Carbide Ceramics: A review." **Journal of Asian Ceramic Societies**. vol. 1, no. 3, pp. 220-242.
32. Kennedy A. **Porous Metals and metal foams made from powders**. : INTECH Open Access Publisher. 2012.
33. Furman E. L., Finkelstein A. B. and Cherny M. L. 2012. "Permeability of Aluminium Foams Produced by Replication Casting." **Metals**. vol. 3, no. 1, pp. 49-57.
34. Paek J. W., Kang B. H., Kim S. Y. and Hyun J. M. 2000. "Effective Thermal Conductivity and Permeability of Aluminum Foam Materials1." **International Journal of Thermophysics**. vol. 21, no. 2, pp. 453-464.

35. Wang X. H. and Liu Z. F. 2004. "The Forchheimer Equation in Two-Dimensional Percolation Porous Media." **Physica A: Statistical Mechanics and Its Applications**. vol. 337, no. 3, pp. 384-388.
36. Costa U. M. S., Andrade Jr J. S., Makse H. A. and Stanley H. E. 1999. "The Role of Inertia on Fluid Flow Through Disordered Porous Media." **Physica A: Statistical Mechanics and Its Applications**. vol. 266, no. 1, pp. 420-424.
37. Andrade Jr J. S., Costa U. M. S., Almeida M. P., Makse H. A. and Stanley H. E. 1999. "Inertial Effects on Fluid Flow Through Disordered Porous Media." **Physical Review Letters**. vol. 82, no. 26, pp. 5249.
38. Lienhard J.H. and J. Lienhard. **A heat transfer textbook**. 3rd Edition. Massachusetts USA : Phlogiston Press Cambridge. 2006.
39. Mizumoto M., Murano T. and Kagawa A. 2002. "Microstructure Control of Particle Reinforced Metal Matrix Composites Fabricated by Low-Pressure Infiltration Process." **Materials Transactions**. vol. 43, no. 10, pp. 2629-2634.
40. Rohatgi P. K., Guo R. Q., Iksan H., Borchelt E. J. and Asthana, R. 1998. "Pressure Infiltration Technique for Synthesis of Aluminum–Fly Ash Particulate Composite." **Materials Science and Engineering: A**. vol. 244, no. 1, pp. 22-30.
41. Bahraini M., Weber L., Narciso J. and Mortensen A. 2005. "Wetting in Infiltration of Alumina Particle Preforms with Molten Copper." **Journal of Materials Science**. vol. 40, no. 9-10, pp. 2487-2491.
42. Molina J. M., Rodriguez-Guerrero A., Bahraini M., Weber L., Narciso J., Rodriguez-Reinoso F., and Mortensen A. 2007. "Infiltration of graphite preforms with Al–Si eutectic alloy and mercury." **Scripta Materialia**. vol. 56, no. 11, pp. 991-994.
43. Taha M. A. and El-Mahallawy N. A. 1998. "Metal–Matrix Composites Fabricated by Pressure-Assisted Infiltration of Loose Ceramic Powder." **Journal of Materials Processing Technology**. vol. 73, no. 1, pp. 139-146.
44. Wu J., L Wang and F. Wang. "Preparation of aluminium foam composite." **This paper was presented at The International Conference on Advanced Technology of Design and Manufacture (ATDM 2010), 23-25 November 2010.**
45. HUO D. W., Juan Y. A. N. G., ZHOU X. Y., Hui W. A. N. G. and ZHANG T. K. 2012. "Preparation of Open-Celled Aluminum Foams by Counter-Gravity

- Infiltration Casting.” **Transactions of Nonferrous Metals Society of China.** vol. 22, no. 1, pp. 85-89.
46. Zhang Y. and Zhao Z. D. 2009. “The Production of Foam Aluminium Alloy by Low-Pressure Infiltration Method.” **Acta Metallurgica Sinica (English Letters).** vol. 12, no. 5, pp. 747-751.
 47. Lucai W., Yuyong C., Fang W., Jianguo W. and Xiaohong Y. 2008. “Preparation of Big Size Open-Cell Aluminum Foam Board Using Infiltration Casting.” **Matrix.** vol. 1, pp. 5.
 48. Jinnapat A. and Kennedy A. 2012. “Characterisation and Mechanical Testing of Open Cell Al Foams Manufactured by Molten Metal Infiltration of Porous Salt Bead Preforms: Effect of Bead Size.” **Metals.** vol. 2, no.2, pp. 122-135.
 49. Li Y., Wang X., Wang X., Ren Y., Han F. and Wen C. 2011. “Sound Absorption Characteristics of Aluminum Foam with Spherical Cells.” **Journal of Applied Physics.** vol. 110, no. 11, pp. 113525.
 50. Lu T. J., Chen F. and He D. 2000. “Sound Absorption of Cellular Metals with Semiopen Cells.” **The Journal of the Acoustical Society of America.** vol. 108, no.4, pp. 1697-1709.
 51. Boschetto A., Bottini L., Campana F., Consorti L. and Pilone D. 2013. “Investigation Via Morphological Analysis of Aluminium Foams Produced by Replication Casting.” **Fracture and Structural Integrity.** vol. 26, pp. 1.
 52. Navacerrada M. A., Fernández P., Díaz C. and Pedrero A. 2013. “Thermal and Acoustic Properties of Aluminium Foams Manufactured by the Infiltration Process.” **Applied Acoustics.** vol. 74, no. 4, pp. 496-501.
 53. Fischer S. F., Schüller P., Fleck C. and Bührig-Polaczek A. 2013. “Influence of the Casting and Mould Temperatures on the (micro) Structure and Compression Behaviour of Investment-Cast Open-Pore Aluminium Foams.” **Acta Materialia.** vol. 61, no. 14, pp. 5152-5161.
 54. Sahin Y. and Acilar M. 2003. “Production and Properties of SiCp-Reinforced Aluminium Alloy composites.” **Composites Part A: Applied Science and Manufacturing.** vol. 34, no. 8, pp. 709-718.
 55. Chung W. S., Chang S. Y. and Lin S. J. 1999. “Low Volume Fraction SiC p/AA 380.0 Composites Fabricated by Vacuum Infiltration.” **Journal of Materials Research.** vol. 14, no. 3, pp. 803-810.

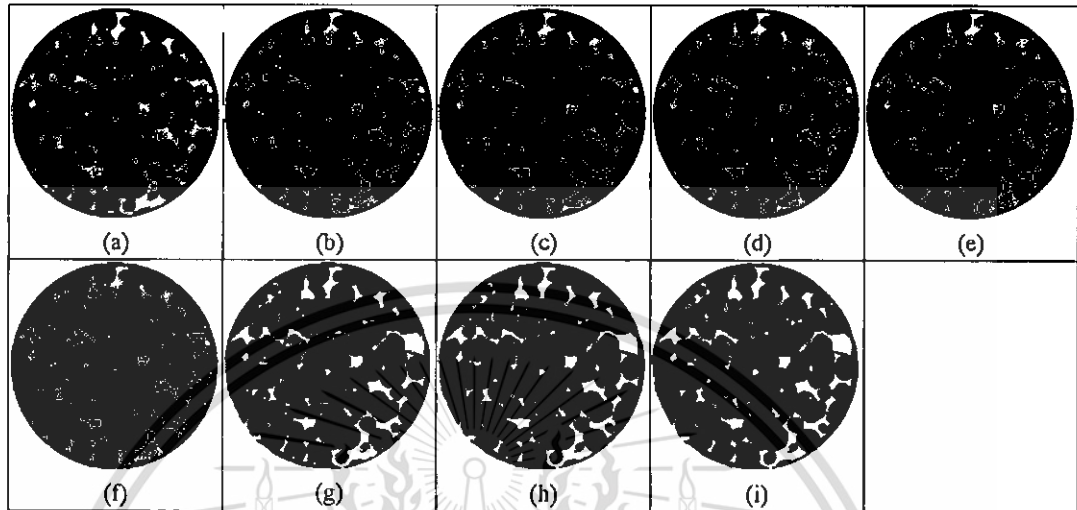
56. Gibson L. J. and Ashby M. F. **Cellular solids: structure and properties.** : Cambridge university press. 1997.
57. Paul A. and Ramamurty U. 2000. "Strain Rate Sensitivity of A Closed-Cell Aluminum Foam." **Materials Science and Engineering: A.** vol. 281, no. 1, pp. 1-7.
58. Kaya A. C. and Fleck C. 2014. "Deformation Behavior of Open-Cell Stainless Steel Foams." **Materials Science and Engineering: A.** vol. 615, pp. 447-456.
59. Tianjian L. 2002. "Ultralight Porous Metals: from Fundamentals to Applications." **Acta Mechanica Sinica.** vol. 18, no.5, pp. 457-479.
60. Andrews E., Sanders W. and Gibson L. J. 1999. "Compressive and Tensile Behaviour of Aluminum Foams." **Materials Science and Engineering: A.** vol. 270, no. 2, pp. 113-124.
61. Zhao C. Y., Lu T. J., Hodson, H. P. and Jackson J. D. 2004. "The Temperature Dependence of Effective Thermal Conductivity of Open-Celled Steel Alloy Foams." **Materials Science and Engineering: A.** vol. 367, no.1, pp. 123-131.
62. Guan D., Wu J. H., Wu J., Li J. and Zhao W. 2015. "Acoustic Performance of Aluminum Foams with Semiopen Cells." **Applied Acoustics.** vol. 87, pp. 103-108.
63. Zhang X., H Li. and S Wang. "A Study on Sound Absorption Behavior of Compound Aluminum Foam." **This paper was presented at The 4th International Conference on Bioinformatics and Biomedical Engineering (iCBBE), 18-20 June 2010. IEEE.**
64. Li Y., Li Z. and Han F. 2014. "Air Flow Resistance and Sound Absorption Behavior of Open-Celled Aluminum Foams with Spherical Cells." **Procedia Materials Science.** vol. 4, pp. 187-190.
65. Bo Z. and Tianning C. 2009. "Calculation of Sound Absorption Characteristics of Porous Sintered Fiber Metal." **Applied Acoustics.** vol. 70, no. 2, pp. 337-346.
66. Wang X. F., Wang X. F., Wei X., Han F. S. and Wang X. L. 2011. "Sound Absorption of Open Celled Aluminium Foam Fabricated by Investment Casting Method." **Materials Science and Technology.** vol. 27, no. 4, pp. 800-804.
67. Zhang, X., S. Wang, and H. Li. "Sound absorption property of multilayered aluminum foam structure." **This paper was presented at The 5th International**

- Conference on Bioinformatics and Biomedical Engineering**, 10-12 May 2011. IEEE.
68. Delany M. E. and Bazley E. N., 1970. "Acoustical Properties of Fibrous Absorbent Materials." **Applied Acoustics**. vol. 3, no. 2, pp. 105-116.
 69. Congyun Z., and Qibai H. 2005. "A Method for Calculating the Absorption Coefficient of A Multi-Layer Absorbent using the Electro-Acoustic Analogy." **Applied Acoustics**. vol. 66, no. 7, pp. 879-887.
 70. Lee F. C. and Chen W. H. 2001. "Acoustic Transmission Analysis of Multi-Layer Absorbers." **Journal of Sound and Vibration**. vol. 248, no. 4, pp. 621-634.
 71. Allard J. and Atalla N. **Propagation of Sound in Porous Media: Modelling Sound Absorbing Materials**. 2nd Edition. John Wiley & Sons. 2009.
 72. Wang X. and Lu T. J. 1999. "Optimized Acoustic Properties of Cellular Solids." **The Journal of the Acoustical Society of America**. vol. 6, no. 2, pp. 756-765.
 73. Yahaya R., Sapuan S. M., Jawaid M., Leman Z., and Zainudin E. S. 2015. "Effect of Layering Sequence and Chemical Treatment on the Mechanical Properties of Woven Kenaf–Aramid Hybrid Laminated Composites." **Materials & Design**. vol. 67, pp. 173-179.
 74. Jawaid M., Khalil H. A. and Bakar A. A. 2011. "Woven Hybrid Composites: Tensile and Flexural Properties of Oil Palm-Woven Jute Fibres Based Epoxy Composites." **Materials Science and Engineering: A**. vol. 528, no. 15, pp. 5190-5195.
 75. Rashdi A. A. A., Sapuan S. M., Ahmad M. M. H. M. and Khalina A. 2009. "Water Absorption and Tensile Properties of Soil Buried Kenaf Fibre Reinforced Unsaturated Polyester Composites (KFRUPC)." **Journal of Food, Agriculture & Environment**. vol. 7, no. 9.
 76. Foamtech aluminium foam leading company. **Acoustic Absorbents**. 2008. [Online]. Available : http://www.foamtech.co.kr/eng02/product/03_01_comparative.php.
 77. ISO-norm 10534-2, 1998, "Acoustics -- Determination of sound absorption coefficient and impedance in impedance tubes -- Part 2: Transfer-function method." **ISO**.

78. ASTM E1050-98, 1998, "Standard Test Method for Impedance and Absorption of Acoustical Materials Using a Tube, Two Microphones, and a Digital Frequency Analysis System." **ASTM International**. West Conshohocken, PA, USA.
79. Banks-Lee P. and Peng H. 1989. "Length Error Analysis for Impedance Tube Measurements." **The Journal of the Acoustical Society of America**. vol. 85, no. 4, pp. 1769-1772.
80. Åbom M. and Bodén H. 1988. "Error Analysis of Two-Microphone Measurements in Ducts with Flow." **The Journal of the Acoustical Society of America**. vol. 83, no.6, pp. 2429-2438.
81. Bodén H. and Åbom M. 1986. "Influence of Errors on the Two-Microphone Method for Measuring Acoustic Properties in Ducts." **The Journal of the Acoustical Society of America**. vol. 79, no. 2, pp. 541-549.
82. Dullien F.A. **Porous Media: Fluid Transport and Pore Structure**. : Academic Press. 1991.
83. NHK SPRING, **Test sound of felt trimback**, 2014, Thailand CO.,LTD.
84. Michaud V. and Mortensen A. 2001. "Infiltration Processing of Fibre Reinforced Composites: Governing Phenomena." **Composites Part A: Applied Science and Manufacturing**. vol. 32. no. 8, pp. 981-996.
85. Scott G. D. and Kilgour D. M. 1969. "The Density of Random Close Packing of Spheres." **Journal of Physics D: Applied Physics**. vol. 2, no. 6, pp. 863.
86. Ashby M. F. and Lu T. 2003. "Metal Foams: A survey." **Science in China Series B: Chemistry**. vol. 46. no. 6, pp. 521-532.
87. Hakamada M., Kuromura T., Chen Y., Kusuda H. and Mabuchi M. 2006. "High Sound Absorption of Porous Aluminum Fabricated by Spacer Method." **Applied Physics Letters**. vol. 88, no. 25, pp. 254106.
88. Alt N. W., Wiehagen N., and Schlitzer M. W. 2001. "Interior Noise Simulation for Improved Vehicle Sound" **SAE Technical Paper**. no. 2001-01-1539.

APPENDIX

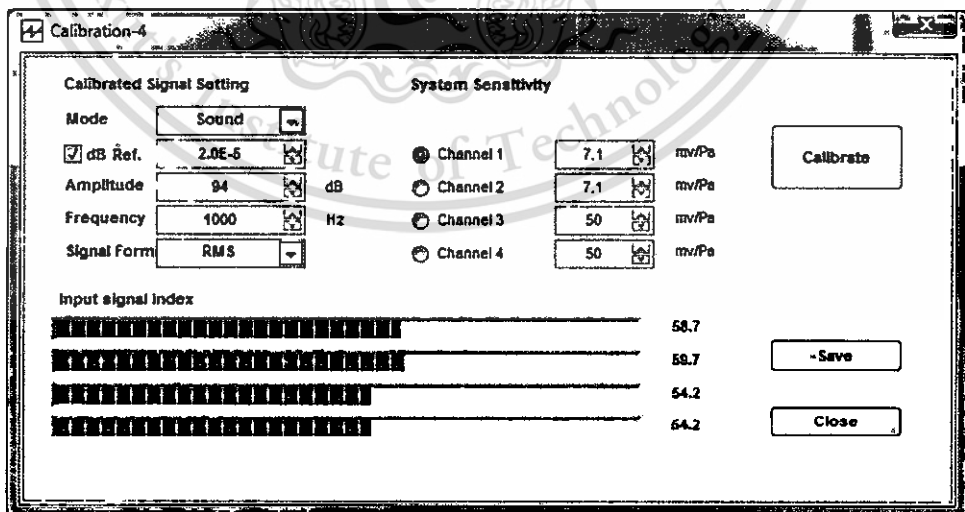
I. Image analysis method for porosity measurement of Al foams



The process of image adjustments were prepared to investigate porosity of aluminium foam samples by image analysis method: (a) image acquisition, (b) grey scale, (c) auto-contrast, (d) noise reduction, (e) sharpen edges, (f) auto fill black, (g) auto fill white, (h) filter gallery cutout and (i) threshold.

II. Sound absorption coefficient test using VA-LAB 4 IMP software

1. Microphone calibration



2. Setting parameters in software.

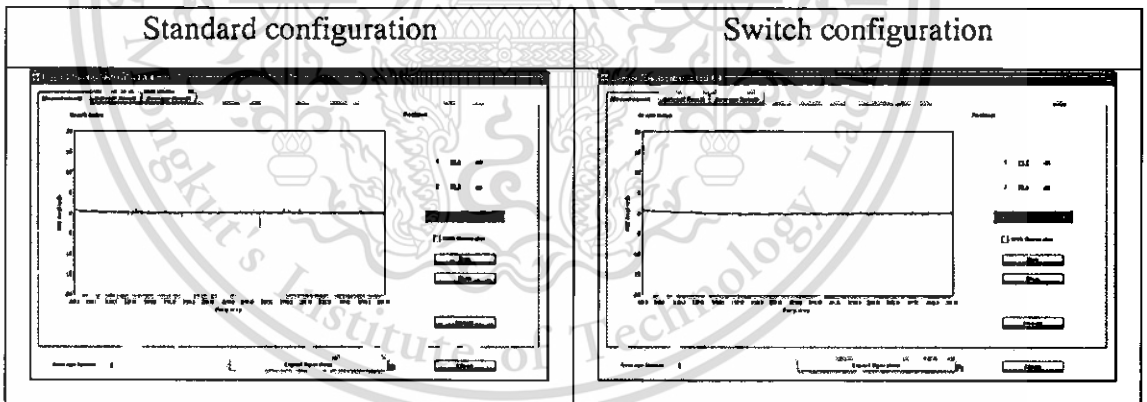
Frequency range 125 – 500 Hz	Frequency range 630 – 3150 Hz
------------------------------	-------------------------------

This material is reserved for educational use only, not allowed for commercial use.

Forbidden to modify the content, and cite the document when use.

<p>Mode Choose: Absorption Measurement</p> <p>TUBE</p> <p>Tube Choose: User-defined</p> <p>Distance to Sample from the nearest Mic(m): 0.025</p> <p>Distance between two Mic.s(m): 0.14</p> <p>Diameter(m): 0.053</p> <p>Frequency Range(Hz): 125 ~ 500</p> <p>Theoretic Range(Hz): 120 ~ 1110</p> <p>ENVIRONMENT</p> <p>Atmospheric Pressure(Pa): 101325</p> <p>Temperature(Degree): 23.2</p> <p>Relative Humidity(%): 60</p> <p>Velocity of Sound(m/s): 345.069</p> <p>Density of Air(kg/m³): 1.17319</p> <p>Characteristic Impedance of Air(Pa*s/m): 404.831</p>	<p>Mode Choose: Absorption Measurement</p> <p>TUBE</p> <p>Tube Choose: User-defined</p> <p>Distance to Sample from the nearest Mic(m): 0.025</p> <p>Distance between two Mic.s(m): 0.03</p> <p>Diameter(m): 0.053</p> <p>Frequency Range(Hz): 630 ~ 3700</p> <p>Theoretic Range(Hz): 580 ~ 3780</p> <p>ENVIRONMENT</p> <p>Atmospheric Pressure(Pa): 101325</p> <p>Temperature(Degree): 23.2</p> <p>Relative Humidity(%): 60</p> <p>Velocity of Sound(m/s): 345.069</p> <p>Density of Air(kg/m³): 1.17319</p> <p>Characteristic Impedance of Air(Pa*s/m): 404.831</p>
---	--

3. Sound absorption coefficient measurement



4. Current result of sound absorption coefficient

CURRICULUM VITAE

NAME: Mr. Phadungkiat Phewoon

DATE OF BIRTH: 28 July 1988

EDUCATION RECORD:

HIGH SCHOOL High School Graduation
La Salle Chotiravi Nakhonsawan, 2006

BACHELOR'S DEGREE B. Eng. in Automotive Engineering
Thai-Nichi Institute of Technology, 2011

MASTER'S DEGREE M. Eng. in Automotive Engineering (International program),
King Mongkut's Institute of Technology Ladkrabang, 2015

HONOUR AND SCHOLARSHIP:

2010 1st prize Rookie awards in 8th JSAE- Japan formula student
competition at Ecopa stadium, shizuoka JAPAN

2011 - 2013 Scholarship for Study Master Degree in Automotive
Engineering at KMITL by TAIST-Tokyo Tech, 2011
Scholarship for study Master degree and research with
MTEC, NSTDA

PUBLICATION: Phewoon, P., Kansuwan, P., Ohtake, N., and Srimanosaowapak, S.,
2013, "Rapid Characterisation Technique for Open-Cell Aluminium
Foam", **The 30th Annual Conference of the Microscopy Society
of Thailand**, January 23 – January 25, 2013, Chanthaburi, Thailand.

Phewoon, P., Kansuwan, P., Ohtake, N., and Srimanosaowapak, S.,
2013, "Rapid Characterisation Technique for Open-Cell Aluminium
Foam", **Journal of the Microscopy Society of Thailand**, 2013, 27:
0857-5285.